



BUSKERUD AND VESTFOLD UNIVERSITY COLLEGE

Optimal Design and Fabrication of the Polymer-based Microneedle for Improved Collection of Whole Blood

Author:

[Hoa Le Thanh](#)

Supervisor:

[Prof. Frank Karlsen](#)

Co-advisor:

[PhD-Student Nhut Tran-Minh](#)

A thesis submitted in partial fulfillment for the
degree of Master of Engineering

in the

[Department of Micro and Nano Systems Technology](#)

May 2014

“Many of life’s failures are people who did not realize how close they were to success when they gave up.”

Thomas Edison

Abstract

The main purpose of this thesis is to develop a blood-sampling device for extracting whole blood from patient's fingers. Polymer-based microneedles array has been chosen and developed. Despite that the concept of microneedle has been intensively studied since several decades ago, the fabrication still remains very challenging. Major challenges concerns the high aspect ratio of microneedle structure (length $> 1500\mu\text{m}$, wall thickness $\sim 100\mu\text{m}$), diminutive and sharp tip. In addition, the microneedles have to be sufficiently strong to avoid fracture and cracks during practical implementation. This thesis covers a total process chain from design, fabrication to performance evaluation of two microneedle designs: traditional-shaped microneedle and pyramid-shaped microneedle.

The first key contribution of this thesis is a highly applicable theoretical model for the optimization of microneedle geometry. The proposed model has been developed to predict the fracture forces. The geometry of microneedle can be optimized to have the highest fracture strength, thus minimizing the failure possibility and increasing safety. A good agreement was observed between the results obtained from analytical solution and from finite element analysis. The improved strength of pyramid-shaped microneedle was also confirmed by practical measurements of fracture force. The results showed that pyramidal tip is stronger than bevel tip with the fracture force of 2.82N compared to 0.51N of bevel tip.

The second contribution of this thesis is a simple, direct and robust method (method 2) proposed for fabrication of SU-8 microneedles. Double exposure is the core technique in method 2, consisting of two exposure steps with high and low exposure dosage, respectively. This fabrication method was initially introduced to improve the remaining challenges of a previously proposed mold-based method - method 1: replication of microneedles. To optimize the process, most of the important fabrication factors were investigated through three main scenarios conducted on three different sloped walls materials: PDMS, SU-8 and aluminum. A CNC-machined aluminum substrate with sloped walls, coated with Cr/Au, showed a big advantage for releasing the microneedles with sharp bevel tips. Microneedles with average tip-size of $23\mu\text{m}$ were feasible with a single-step of SU-8 lithography. Microneedles can be fabricated with a length up to $1500\mu\text{m}$ with an aspect ratio of 15.

For practical verification of the fabricated microneedles, skin penetrability was investigated on human fingers. Fabricated microneedles with the proposed designs were sharp and strong enough to puncture the human skin safely. There was blood coming out at several insertion spots, indicating that the microneedle may be long enough to reach the blood vessels.

Preface

This thesis is submitted in a partial fulfillment of the degree of Master in engineering from the Department of Micro and Nano Systems Technology (IMST), at Buskerud and Vestfold University College (HBV).

This project work has been conducted in three semesters from December 2012 to June 2014 under the supervision of Professor Frank Karlsen.

The ideal of this project has been brought up as a solution to overcome the biological challenges of traditional hypodermic needles to collect blood. This is an initial stage (i.e. self-sampling microneedle based device) of a self-diagnostic device. This approach may open a future path for disease diagnostic.

Horten, 2014-5-24



Hoa Le-Thanh

Acknowledgements

As I reach towards the culmination of my master program, I would like to extend my heartiest gratitude to everyone, who have been helping me during this wonderful journey, who provided me such a great opportunity to be here in Norway, the country of peace and kindness.

I would like to express my special appreciation and gratitude to my supervisors, Professor Frank Karlsen for his kindness, endless help and valuable guidance. I want to express my gratefulness to him for showing his attentions to me, helping me to improve myself not only limited to my knowledge but also in my personal developments.

I am grateful to Vy Nguyen who has been helping me a lot in my study and lifting me up whenever I felt stressful and pessimistic. I also want to give my special thank to Hai, my best friend, for being with me all the time and for his friendship.

I extend my sincere thanks to Professor Kaiying Wang, Professor Lars Hoff and Professor Einar Halvorsen for their valuable advices. Without them, I would not be able to overcome numbers of scientific challenges during my work. I am especially grateful to Zekija Ramic , Ragnar D. Johansen, Thomas Martinsen for their supports for my experimental work.

I would also like to thank PhD candidate Nhut Tran Minh, who brought me to this project and I am very grateful for what he has done to help me in my very first stage. My friends, my seniors, Bao Quoc Ta and Van Khanh Nguyen who gave me lots of valuable helps and advice, and Vinh Cao Duy who is my close friend, I would like to thank him for his brotherhood, for being with me every time I need help. And once again, I want to say thank you to every one for helping me.

Last but not least, I would like to dedicate my work to my parents and my sister, because of whose unconditional love, care and belief in me. Their loves are my biggest motivation which has been supporting me to go that far in my academic journey.

Contents

Abstract	v
Preface	v
Acknowledgements	ix
Contents	x
List of Figures	xiii
List of Tables	xv
Abbreviations	xvi
1 Introduction	1
1.1 Research context and motivations	1
1.2 Research studies, Contributions and Publications	3
1.2.1 Research studies	3
1.2.2 Contributions	3
1.2.3 Publications	4
1.3 Thesis Structure	4
2 Background	7
2.1 Microneedle	7
2.2 Background	13
2.2.1 A rigid polymer: SU-8 2150	13
2.2.2 Structural analysis	14
3 Geometry Optimization	17
3.1 Design of pyramid-shaped microneedles	18
3.2 Analytical solution	18
3.2.1 Skin deformation and insertion force	18
3.2.2 Mathematical frameworks	19
3.2.2.1 Analysis of critical buckling load	20
3.2.2.2 The proposed theoretical model for analysis of bending strength	21
3.3 Numerical solution	24
3.4 Results and Discussion	25

3.4.1	Failure Mechanism 1: Critical Buckling Load	25
3.4.2	Failure Mechanism 2: Maximum bending force	26
3.4.3	Insertion Force	31
3.5	Chapter conclusions	32
4	Fabrication of Microneedles	35
4.1	Fabrication concepts	36
4.1.1	Method 1: Replication of microneedles	36
4.1.2	Method 2: Direct formation of microneedles	37
4.1.3	Design of aluminum holder for inclined exposure	38
4.2	Fabrication issues and solutions	40
4.2.1	Bending problem and the proposed solution "separated lines"	41
4.2.2	Air gap problem and glycerol compensation	42
4.2.3	Aluminum substrate - an alternative for silicon wafer	43
4.3	Optimization of lithography process for ultrathick SU-8 layer	45
4.4	Fabrication of pyramid-shaped microneedles (PMNs)	49
4.5	Fabrication of traditional-shaped microneedles (TMNs)	52
4.5.1	Fabrication of TMNs on PDMS sloped walls	52
4.5.2	Fabrication of TMNs on SU-8 sloped walls	55
4.5.3	Fabrication of TMNs on CNC-machined aluminum sloped walls	57
4.6	Chapter conclusions	60
5	Performance Evaluation	63
5.1	Measurements of fracture forces	64
5.2	Testing of skin penetrability on human fingers	66
5.2.1	Testing of microfabricated SU-8 microneedles	66
5.2.2	Testing of hypodermic stainless steel needles	68
5.3	Chapter conclusion	69
6	Conclusion	71
A	Mathematical derivations	73
B	A simple, robust fabrication method with CNC-machined aluminum sample	79
B.1	Advantages of CNC-machined aluminum sample in microneedle fabrication	79
B.2	Design of CNC-machined aluminum sloped walls	81
B.3	Problem of damaged tips and surface modification	81
B.4	Fabrication of traditional-shaped microneedles	83
	Bibliography	87
	Publications	95

List of Figures

2.1	Blood-sampling device developed by Li et al.	8
2.2	Recently proposed silicon-based microneedles.	9
2.3	Recently proposed metallic microneedles.	10
2.4	Micrographs of Ni microneedle fabricated by using drawing lithography to fabricate the polymer molds for the fabrication of metallic microneedles. . . .	11
2.5	Lithography process: development with megasonic agitation.	12
2.6	Recently proposed SU-8 microneedles for blood extraction.	13
3.1	Illustration for microneedle insertion and skin deformation.	18
3.2	Illustrations for distributed bending force.	19
3.3	Illustrations for stress distribution on pyramidal tip.	22
3.4	Illustrations for five cross sections of PMNs.	23
3.5	Cross section at region 1. (a) inertia moment, (b), (c) illustrate for Q_{1a} and Q_{1b}	23
3.6	Finite element method with COMSOL simulator.	24
3.7	Optimization of simulation mesh with five mesh sizes: (a) fine, (b) finer, (c) extra fine, (d) extremely fine, (e) 1/2 extremely fine.	25
3.8	Critical buckling load versus base width and length.	26
3.9	Scenario 1: Matching between analytical and numerical solutions - general trend.	27
3.10	Scenario 1: Matching between analytical and numerical solutions - graphical analysis.	28
3.11	Scenario 1: The effect of sharp edge on the magnitude of shear stress.	29
3.12	Scenario 2: Effects of microneedle geometry on the magnitude of shear stress.	30
3.13	Scenario 3: Prediction of maximum bending force.	30
3.14	Comparison between P_b of PMNs and TMNs with the variation in base width.	31
3.15	Illustrations for force applying area (A_{insert}) at different penetration depth. .	31
3.16	Deformation of a Timoshenko beam (blue) compared with that of an Euler-Bernoulli beam (red).	32
3.17	Integration of microneedles array.	33
4.1	Process flow of method 1 and method 2.	36
4.2	Construction of tip-formation structures.	37
4.3	Design and working principle of the aluminum holder.	39
4.4	Working principle of inclined exposure to fabricate pyramidal tips with a aluminum holder.	40
4.5	Optical photographs illustrate the advantage of the separated lines in thermal stress reduction.	41
4.6	The effect of gap between mask and substrate on the quality of fabricated pyramid-shaped trenches.	42

4.7	Illustrations for the use of Al substrate in fabrication of pyramidal tips. . . .	43
4.8	A topography 3D image of Al substrate built by Interferometer Wyko NT9100 at 20x magnification.	44
4.9	Illustration of SU-8 based barrier for coating of thick SU-8 layer	46
4.10	Optical illustrations for the optimization of exposure dosage.	47
4.11	Optimization of PEB time for the fabrication of pyramidal tips.	48
4.12	Process flow for fabrication of PMNs by using method 1.	49
4.13	Step-by step results of PMNs fabrication. (a) Pyramidal tips on Al substrate, (b) Inverse PDMS pyramidal tips.	50
4.14	Step-by step results of PMNs fabrication. (a) Microneedle-like holes, (b) PMNs.	50
4.15	Step-by step results of PMNs fabrication. (a) misaligned PMNs, (b) well-aligned PMNs.	51
4.16	Process flow for fabrication of TMNS on PDMS sloped walls.	52
4.17	Optical micrographs of fabricated TMNs.	54
4.18	Misalignment due to the distance between the alignment marks on mask and substrate.	55
4.19	Process flow for fabrication of TMNs on SU-8 sloped walls.	56
4.20	Tip-damaging problem caused by strong adhesion between microneedles and the sloped walls.	57
4.21	Three different types of sloped walls.	59
4.22	Highly flexible design of CNC-machined aluminum sloped walls.	59
4.23	Optical micrographs of SU-8 TMNs fabricated with three different lengths.	60
5.1	Measurement setup with Shear tester Delvotec 5600.	65
5.2	Measurement results of fracture force of PMNs and TMNs.	65
5.3	Scenario 1: Testing of skin penetrability with one single microneedle.	67
5.4	Scenario 2: Brokenness of the support plate during insertion of a 3×3 microneedles array.	67
5.5	Scenario 2: Successful insertion of a 3×3 microneedles array.	68
5.6	Testing of skin penetrability with a hypodermic stainless-steel needle.	69
A.1	Five cross sections of PMNs	73
A.2	Cross section at region 1. (a) inertia moment, (b), (c) illustrate for Q_{1a} and Q_{1b}	74
A.3	Cross section at region 2. (a) inertia moment, (b), (c) illustrate for Q_{2a} and Q_{2b}	75
A.4	Cross section at region 3. (a) inertia moment, (b), (c) illustrate for Q_{3a} and Q_{3b}	75
A.5	Cross section at region 4. (a) inertia moment, (b), (c) illustrate for Q_{4a} and Q_{4b}	76
B.1	Illustration for the improved accuracy in mask alignment.	80
B.2	Illustration for coating barrier.	81
B.3	Illustration for three different coating heights.	82
B.4	Optical micrographs of SU-8 sloped walls and CNC-machined aluminum sloped walls.	82
B.5	Illustration for three different methods for surface modification.	83
B.6	Process flow for fabrication of TMNs using method 2 and CAS.	84
B.7	Optical micrographs of SU-8 TMNs fabricated with CNC-machined aluminum samples.	85
B.8	Optical micrograph of a 3×3 TMNs array fabricated with CNC-machined aluminum samples.	85

List of Tables

3.1	Optimization of mesh size.	25
3.2	Scenario 1: Matching between analytical and numerical solutions - statistical analysis.	28
3.3	Estimation of required insertion force to puncture human skin.	32
4.1	Comparison between properties of Aluminum substrate and Silicon wafer. . .	43
4.2	Summary of lithography process for thick SU-8 layer	48
4.3	Summary of the advantages and disadvantages of TMNs fabrication on three different sloped walls.	58
5.1	Measurement of fracture force on fabricated microneedles	64
B.1	Comparison between different methods to lower the adhesion of the surface of CAS.	83

Abbreviations

MNs	Microneedles
PMNs	Pyramid-shaped Microneedles
TMNs	Traditional-shaped Microneedles
CAS	CNC-machined Aluminum Sample
CASW	CNC-machined Aluminum Sloped Wall

*Dedicated to my beloved parents and my sister, for giving me their
endless love and encouragement. . .*

Chapter 1

Introduction

1.1 Research context and motivations

Early diagnosis or pre-disease detection plays a vital role in the adequate selection of suitable therapeutics to increase the patient survival rates. Early detection is urgently required to be highly sensitive and extremely accurate for reliable results. Motivated by the valuable advantages of pre-cancer detection, SelfPOCNAD project has been proposed to develop an industrial prototype for a rapid detection platform. The platform is designed to operate with five main functions of automated patient samples collection, pre-treatment, preparation, analysis and target detection [1]. Although the original concept was designed for Cervical Cancer Screening, the platform may also be used for diagnostic of other blood-related disease. The project focuses on sampling and analyzing of human blood, one of the most valuable source of body fluids that can indicate various states of health and disease. As a part of SelfPOCNAD project, this thesis aims to construct the first stage of the detection platform i.e. sample collection device. By taking the advantages of microneedle, a pathway for optimal collection of whole blood is provided. The chosen type of microneedle in this thesis is polymer based microneedle.

Firstly, in order to answer the question of why hypodermic needles have been replaced by other potential alternatives such as microneedles, several issues of hypodermic needles need to be addressed. Historically, hypodermic needles are the most effective method, a traditional pathway for blood withdrawal carried out by invasive techniques. It has been a standard for effective transportation of body fluids/drug. However, there are several challenges associated with hypodermic needles, from physical problems such as insertion pain or tissue trauma to psychological problems such as patient discomfort or needle phobia reported by Halminton [2]. Needle phobia is a problem that comes from patient's fear of sharply pointed objects like the hypodermic needles. In addition, there is a lack of convenience and user-friendly ability

with hypodermic needles [3]. The requirement of expertise and specialized medical knowledge for implementation is the biggest challenge [4], especially for patient who need periodic and continuous monitoring, e.g. diabetic patients [5].

A better way to collect blood is to perform the injection at patient's fingers. However, blood vessels at human fingers are relative small than the tip of a hypodermic needle. The typical size of hypodermic needles used in blood collection is about 20 to 22 gauge (0.7176mm to 0.9081mm in outer diameter and 0.41mm to 0.6mm inner diameter [6]), whereas the blood vessels are ranging from 0.3mm to 0.5mm. In addition, hypodermic needles are manufactured with a sharp beveled tip (12° to 15°). The opening area at beveled tip is approximately 5-10 times larger compared to the inner area of microneedle hollow. Moreover, the blood circulation in fingers is poor, leading to the problems of collecting blood when hypodermic needle is utilized. With old, disable or sick patients, normally they do not have optimal blood circulation at their fingers. Therefore, the proposed design of 9-microneedle array may help in this situation to obtain larger volume of collected blood for further process.

As an alternative for hypodermic needles, microneedle has become an interest research topic since decades ago. In this thesis, microneedle is chosen with the expectation of higher capability to handle whole blood was introduced. Its advantages have been reported by numbers of studies, in this chapter a short overview is given as follows: painless injection [7, 8], portability, higher transport efficiency in blood collection and the ability to precisely control the amount of collected blood. Therefore, microneedle has become a very promising research topic for enormous potential applications. After more than two decades, its extraordinary properties and various applications have been very well exploited. However, there are still numbers of challenges with the manufacture of microneedles, especially in geometric optimization and methods for fabricating microneedles. In fact, geometrical features such as: shape of the tip (truncated tip, tapered [9], hypodermic-needle-like [10]), tip angle, base width or tip width can directly affect mechanical strength and stability of the microneedles.

For the purpose of blood collection, in addition to the typical requirements of sharp tip, hollow structure, microneedle length is required to be longer than $1500\mu\text{m}$ in order to reach the blood vessels [11]. With that gigantic length, the fabrication problems may become more challenging to obtain high aspect ratio structures. However, with LIGA like photolithography with SU-8 negative tone photoresist, it may be able to produce the microneedles with satisfied geometrical features. The well-established technique of UV lithography can also be utilized with SU-8 for lost-cost manufacture.

In this thesis, the study begins with the geometric optimization followed by fabrication and characterization of microneedles. There are four motivational question to be answered in this thesis.

Question 1: What is the optimal design of microneedle for the whole blood collection? And how to construct it?

Question 2: Is it possible to fabricate and integrate the microneedle array with the proposed geometry? If yes, what kind of technologies can be applied to fabricate it?

Question 3: Whether the microneedles as proposed in this thesis can safely penetrate the human skin and can it survive after penetration process?

Question 4: How to evaluate and test it? Does it cause pain or uncomfortable feeling during implementation

1.2 Research studies, Contributions and Publications

1.2.1 Research studies

Study 1: Structural analysis: an optimization of microneedle geometry based on the investigation of failure mechanisms: critical buckling load and bending strength. Study 1 is presented in chapter 3.

Study 2: Process optimization for fabrication of polymer-based microneedle array. Study 2 is presented in chapter 4.

Study 3: Fabrications of microneedles: pyramid-shaped microneedles (PMNs) and traditional-shaped microneedle (TMNs). Study 3 is presented in chapter 4.

Study 4: Performance evaluation: measurements of fracture force and skin penetrability test. Study 4 is presented in chapter 5.

1.2.2 Contributions

Main contributions of this thesis are:

Contribution C1: A theoretical model to study the fracture forces of microneedles for geometry optimization.

Contribution C2: A simple, robust method with high throughput and good repeatability to fabricate microneedles on CNC-machined aluminum sample.

Contribution C3: A simple solution, namely "separated lines", to solve the problem of wafer bending caused by large CTE mismatch between SU-8 and silicon wafer.

1.2.3 Publications

Publications enclosed in this thesis

P1: Hoa Le Thanh, Hai Le The, Nhut Tran-Minh, Vy Nguyen, Frank Karlsen, "Optimal design and fabrication of polymer-based microneedle for safe collection of whole blood", submitted to Special Issue for Micro and Nano Letters, May 2014.

P2: Hoa Le-Thanh, Nhut Tran-Minh, Hai Le The, Frank Karlsen, "A Novel Design of Hollow Microneedle for Blood Extraction", in Proc. of IEEE-International Conference on Nano/Micro Engineered and Molecular Systems, pp. 430-435, April 2014.

P3: Hoa Le-Thanh, Nhut Tran-Minh, Hai Le The, Frank Karlsen, "A Study on Mechanical Strength of Pyramid-Shaped Microneedle", in Proc. of IEEE-Middle East Conference on Biomedical Engineering, pp. 29-32, February 2014.

Publications not enclosed in this thesis

P4: Hai Le The, **Hoa Le Thanh**, Nhut Tran-Minh, and Frank Karlsen, "Optimal design of an effective passive micromixer with shifted trapezoidal blades using wide Reynolds number range", accepted by Journal of Micromechanics and Microengineering May 2014.

P5: Hai Le The, Nhut Tran-Minh, **Hoa Le-Thanh**, Frank Karlsen, "A Novel Micromixer with Multimixing Mechanisms for High Mixing Efficiency at Low Reynolds Number", in Proc. of IEEE-International Conference on Nano/Micro Engineered and Molecular Systems, pp. 651-654, April 2014.

P6: Hai Le The, Nhut Tran-Minh, **Hoa Le-Thanh**, Frank Karlsen, "A Novel Passive Micromixer with Trapezoidal Blades for High Mixing Efficiency at Low Reynolds Number Flow", in Proc. of IEEE-Middle East Conference on Biomedical Engineering, pp. 25-28, February 2014.

P7: Nhut Tran-Minh, **Hoa Le-Thanh**, Frank Karlsen, "Analytical and Numerical Approaches for Optimization Design of MEMS Based SU-8 Microneedles", ACBIT2013, Japan. To be published in: Computer Methods and Programs in Biomedicine.

1.3 Thesis Structure

The dissertation is structured as six chapters. Following this chapter of introduction, chapter 2 presents the project background as well as the literature review of the previously proposed works in relation to microfabricated microneedles. Chapter 3 presents the development of

analytical solution for structural fracture analysis based on different failure mechanisms. Intensive calculations and simulations are accompanied for a detailed verification. Based on the obtained results, this chapter ends with the proposal of an optimal geometry for blood collection microneedle. In the following chapter, fabrication of the proposed microneedles are presented in chapter 4, including: mask designs, fabrication processes and optimization of lithography parameters. Fabricated results will be depicted with optical and SEM pictures followed by a short discussion from the experimental results. Chapter 5 describes the procedure to evaluate the performance of microneedles in terms of mechanical strength and skin penetrability. In chapter 6, the most valuable obtained results are summarized and concluded upon. In addition, an outlook for suggested future works is given for improvements of microneedle design and fabrication. Appendix A presents the mathematical derivations in addition to the mathematical frameworks in chapter 3. Appendix B presents the details of the second key contribution (*Contribution C2*). Lastly, three relevant publications are enclosed in the end of this thesis.

Chapter 2

Background

2.1 Microneedle

Over the past two decades a tremendous amount of studies in the area of microneedle-based devices have been carried out since its first discovery by Albert Pisano [12]. Typically, the microneedles can be classified into two types: in-plane microneedle (longitudinal axis parallel to the fabricated substrate) and out-of-plane microneedle (longitudinal perpendicular parallel to the fabricated substrate). In 1998, Mark Prausnitz et al. introduced the first "out-of-plane" solid silicon microneedle. They demonstrated the improved skin permeability of their proposed microneedles. This study opened a new trend for the development of pain-free micromachined microneedles. Some years later, in 2005, Stoeber et al. [13] reported the first hollow silicon-based microneedle. An out-of-plane, $200\mu\text{m}$ tall hollow microneedle was fabricated by isotropically wet etching of silicon with the hollow diameter of $40\mu\text{m}$. They also studied the skin penetrability by performing shallow injections into the dermis layer, thus enhance possibility of painless epidermal drug delivery.

Based on the ideal of hollow microneedle that might exhibit in the same pathway as conventional hypodermic needles for interstitial fluid and blood collection. Recently, a few demonstrations of invasive transdermal collection of interstitial fluid and blood have been reported, using the microfabricated microneedle-based devices. In 2002, Griss and Stemme [14] introduced a novel design of side-opened hollow microneedle that might provide better fluid transfer. Two years later Mukerjee et al. [5] demonstrated the ability to extract interstitial fluid from human body to measure glucose concentration for monitoring of diabetic. The driving force for extraction process is the capillary force in needle hollows. On the same purpose, Tsuchiya et al. [15] developed a compact human blood sampling device integrated with an actuator, micropump and a titanium microneedle for monitoring of blood glucose. For whole blood collection, the extraction speed of $2\mu\text{L}/\text{min}$ might be achieved through a

microneedle with the inner diameter of $25\mu\text{m}$. In one of the most recently studies, Li et al. [11] introduced a functional prototype blood-sampling device with a single metallic microneedle as shown in Fig. 2.1a. Practical tests on the extraction ability were conducted on the tail artery of the mouse as shown in Fig. 2.1b. With a hollow structure with 15° beveled tip and an actuator chamber (see Fig. 2.1b), the experiments showed that their proposed microneedle was able to collect a $20\mu\text{L}$ volume of mouse blood. They also pointed out that for blood-sampling on human fingers, the most important geometrical factor is microneedle length ($\sim 1500\mu\text{m}$), along with the requirements of hollow structure and sharp tip.

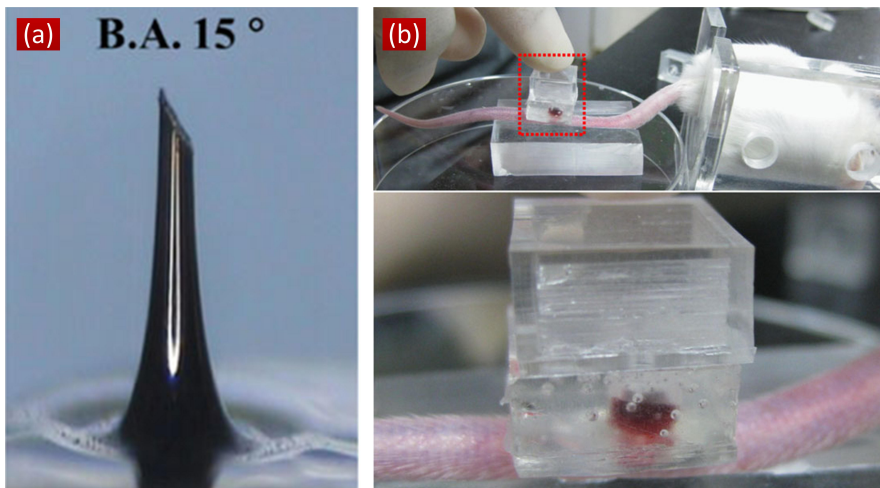


FIGURE 2.1: Blood-sampling device developed by Li et al. [11]. (a) a nickel electroplated microneedle with 15° beveled tip, (b) injection of microneedle into the tail artery and illustration for the extracted blood.

In the progressive manner, the predominant materials for constructing the fabricated microneedles are silicon and metal [16]. With conventional MEMS technologies, silicon-based microneedles have achieved an extraordinary attention as reported in many previous studies [14, 17–19]. In 1998, Henry et al. [17] introduced a micromachined solid microneedle fabricated (see Fig. 2.2a) based on the method of black silicon. The microneedle shafts and sharp tips were left behind the etching mask after underetching of silicon with reactive ion etching (RIE). For high aspect ratio structures, one frequently-used technology, which have been applied in a wide range of previously proposed studies, is deep reactive ion etching (DRIE). In standard MEMS technology, DRIE is one popular option to obtain high aspect ratio silicon microneedles. In 2002, Griss et al. reported that a side-opened silicon microneedle (see Fig. 2.2b) fabricated by deep reactive ion etching (DRIE) might be feasible for transdermal liquid transfer [14]. Two years later, Mukerjee and his group [5] reported two designs of "hypo-dermic" microneedle (see Fig. 2.2c) and volcano-like silicon microneedle (see Fig. 2.2d) for transdermal blood sampling. DRIE was performed on both sides of the substrate to obtain the high aspect ratio of about 25. The microneedles with the tip-size of $2\mu\text{m}$ was manufacturable by using isotropic wet etching of silicon. Although the field of silicon-based microneedles is attractive with well-established technologies and infrastructure, the fabrication cost still

remains relatively high for commercializing and mass-production. Moreover, in the biological domain, silicon-based microneedles problematic with risks associated during implementation, especially with its unproven biocompatibility and the brokenness of microneedle inside the skin. Since silicon is fragile, hard but very brittle [20], the possibility of brokenness of microneedles inside the skin is therefore considerably high for practical operation.

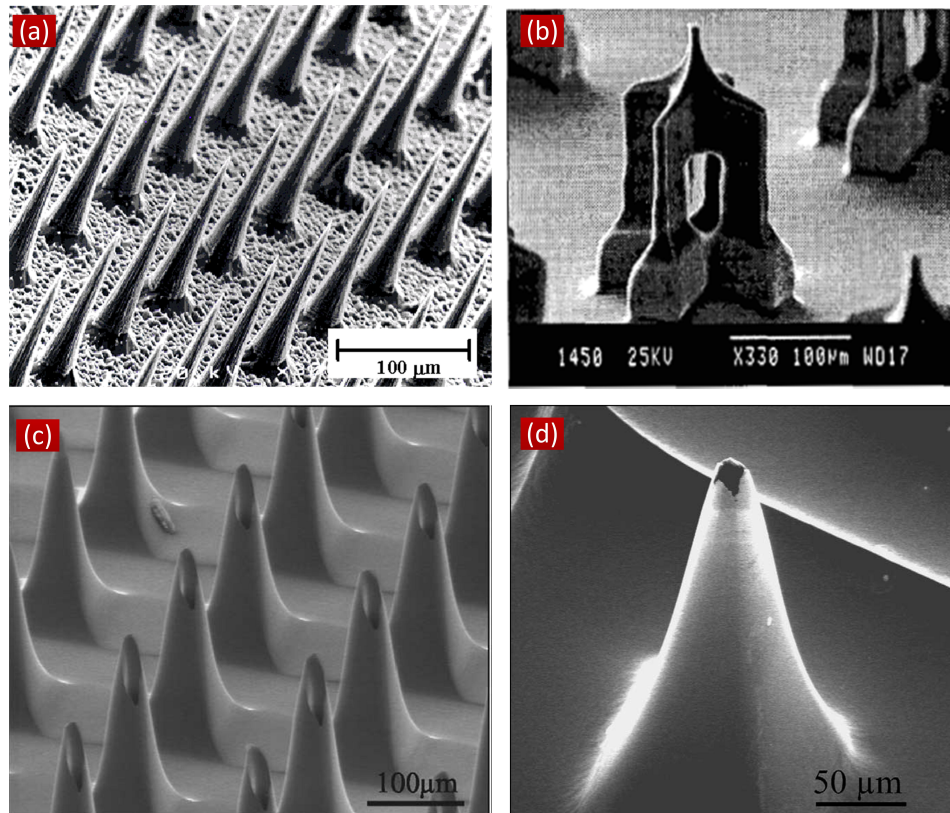


FIGURE 2.2: Recently proposed silicon-based microneedles. (a) micromachined solid microneedle fabricated by RIE of silicon, fabricated by Henry et al. [17], (b) side-opened silicon microneedle fabricated by Griss and Stemme [14], (c) "Hypodermic" microneedle and (d) volcano-like silicon microneedle fabricated by Mukerjeea et al. [5].

For microneedles that need high structural strength, metal is especially attractive with its improved mechanical properties compared to silicon. Strong, cheap metals with good biocompatibility are highly desirable, for example: titanium, platinum or nickel are the most frequently-used metals to construct the microneedles. In 2005, Tsuchiya et al. [15] produced an automatic blood extraction system integrated with a titanium microneedle using as a blood collector. The sputtered Ti microneedle was fabricated at the same size of a female mosquito's labium: 1mm tall, $60\mu\text{m}$ outer diameter and $25\mu\text{m}$ inner diameter as shown in Fig. 2.3a. Sputtering deposition was utilized. The system was proved to be able to collect fluids in a speed of $2\mu\text{L}/\text{min}$. In another studies, Davis et al. [21] proposed a robust, inexpensive fabrication method to construct a $500\mu\text{m}$ -tall nickel microneedles (see Fig. 2.3b) for *in vivo* insulin delivery. By using a pre-fabricated polymer molds, a $10\mu\text{m}$ -thick nickel layer was electroplated onto a conductive seed layer (Ti-Cu-Ti: 35nm-650nm-35nm). Similarly, Kim et al. [9] introduced a process to fabricate electroplated Ni microneedles based on a pre-fabricated

SU-8 molds (see Fig. 2.3c). To obtain the SU-8 molds, backside SU-8 exposure was conducted on a glass substrate to form $400\mu\text{m}$ tall tapered SU-8 pillar. A $20\mu\text{m}$ -thick electroplated Ni layer was performed onto the SU-8 pillar, the tips were then opened by mechanical polishing.

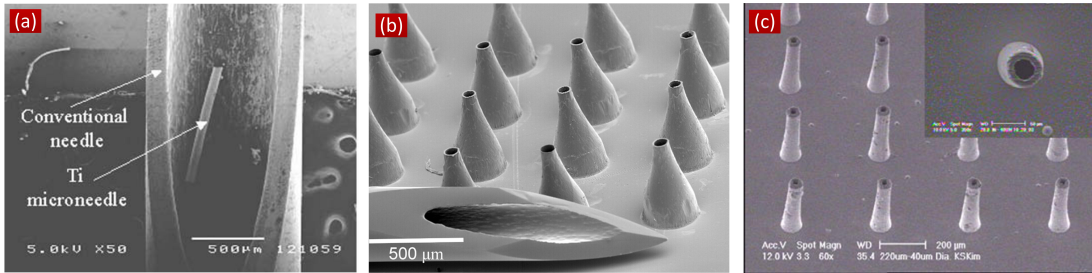


FIGURE 2.3: Recently proposed metallic microneedles. (a) 1mm tall sputtered Ti microneedle fabricated by Tsuchiya et al. [15], (b) $500\mu\text{m}$ tall tapered electroplated Ni microneedle array fabricated by Davis et al. [21], (c) $400\mu\text{m}$ tall hollow cylindrical metallic microneedles fabricated by Kim et al. [9].

To construct a polymer mold for fabrication of metallic microneedles, drawing lithography is a new approach for fabricating ultrahigh aspect ratio polymer structures [11, 22]. In 2010, Lee et al. [22] introduced a process to fabricate ultrahigh-aspect-ratio (over 100) microneedles by applying draw lithography to obtain $2000\mu\text{m}$ -tall SU-8 pillars (see Fig. 2.4a). Nickel was then electroplated on SU-8 conducted with 0.5M Tollens' reagent. The tips of SU-8 were protected during electroplating process by coating with enamel - an electroless material. The microneedles were released by 1-hour stripping in SU-8 remover. Inner diameter at tips was measured about $20\mu\text{m}$. In the same way to produce polymer molds, Li et al. [11] fabricated a $1800\mu\text{m}$ tall nickel microneedle to demonstrate the collection ability of blood (see Fig. 2.4b). The beveled angle of the tips were precisely formed by laser cutting. In general, metallic microneedles are still fragile and the risk of brokenness still remains. The metal deposition process was conducted on a pre-fabricated microneedle-shaped molds. Moreover, the fabrication process is normally serial and still expensive [20].

Many researchers started to investigate the potential of polymers in fabrication of microneedles. By using biocompatible polymers with high viscous-elasticity polymers, the risk of brokenness may be reduced. Moreover, inexpensive and mass-production techniques can be utilized, particularly with SU-8 lithography. However, the fabrication of high-aspect-ratio structures or hollow structures still remains very challenging. There is a branch concentrated on X-ray lithography with PMMA positive photoresist [23–27]. Although it has been proved that high-aspect-ratio structures are achievable with X-ray lithography but the process is much expensive compared to LIGA-like lithography. Mask fabrication for X-ray patterning is very challenging. Therefore, SU-8 is the first choice.

There have been lots of studies focused on SU-8 lithography to fabricate microneedles. Various shapes and designs of SU-8 microneedles have been reported. Among the multiplicity

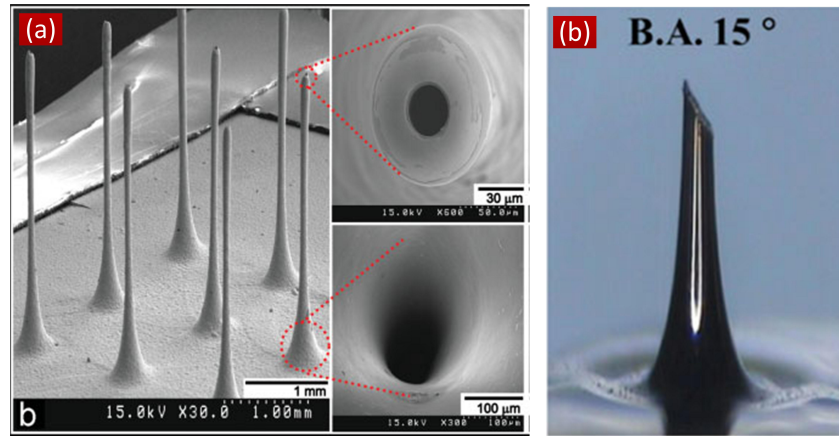


FIGURE 2.4: Micrographs of Ni microneedle fabricated by using drawing lithography to fabricate the polymer molds for the fabrication of metallic microneedles. (a) Electroplated Ni microneedles fabricated by Lee et al. with height of $2000\mu\text{m}$, $300\mu\text{m}$ base and $20\mu\text{m}$ base flat tip diameter [22], (b) Electroplated Ni microneedle fabricated by Li et al. with height of $1800\mu\text{m}$, inner diameter of $60\mu\text{m}$ and beveled tips of 15° [11].

of methods, mold-based fabrication methods has been proved to be reasonable, inexpensive and robust for mass production [16]. The most challenging step in fabrication of SU-8 microneedle is the formation of microneedle hollows. Previously, DRIE was primarily used to create hollows of silicon-based microneedles, however, DRIE requires a high-cost equipment. Another way to form the hollows is using laser drilling as presented in [28, 29]. Choi et al. reported the fabrication of SU-8 hollow microneedles with lithography, laser drilling and reactive ion etching (RIE) in [28]. The support plate was created by spinning and patterned with a chromium mask. Circular SU-8 pillars were formed by backside exposure through the glass substrate. Laser drilling was utilized to form the microneedle hollows followed by microneedle sharpening with RIE. Drilling was also used to make the molds for injection molding of polymer microneedles as introduced by Yung et al. in [30]. One downside of laser drilling is that the drilling process is serial and time-consuming.

Scientists then started a simpler, faster method with conventional UV lithography. However, conventional lithography remained challenging with ultrathick SU-8 photoresist coatings. The process parameters have to be well-controlled for high-aspect-ratio lumens. Number of studies were conducted on the process optimization of ultrathick SU-8 lithography. Among number of scientists, Wang and his group have introduced valuable studies on this issues. For example, in [31] a study of gap compensation and wavelength selection for ultrathick was firstly introduced in 2005. By filling the gap between mask and substrate with glycerol, high quality sidewalls were achieved. They also pointed out that optical filter (cut-on wavelength $\sim 365\text{nm}$) might help to obtain ultrahigh-aspect-ratio structures (more than 190:1). Moreover, they also proposed the optimal exposure dosage for 1 - 1.5mm-thick SU-8 with different structures, including: cylinders/square cylinders ($1100\mu\text{m}$ thick - $2000\text{mJ}/\text{cm}^2$), cross ($1500\mu\text{m}$ thick - $7000\text{mJ}/\text{cm}^2$). Similarly, Chaung et al. made the same conclude on the advantage of gap compensation (with glycerol) on the quality of sidewalls, particularly is vertical walls [32].

The optimization of baking time and development were also reported. Jin et al. [33] investigated the relationship between soft-baking time and UV transmittance of unexposed ultrathick SU-8 layer. They suggested that 1000 μm -thick SU-8 layer requires 30 hours soft-baking at 95°C. However, in his research [34], Wang pointed out that soft-baking time can be reduce by baking at 110°C. Particularly for a 1100 μm -thick SU-8 film, it only needs 10 hours baking on hot plate at 110°C. He also recommended to use a baking profile (consists of ramping up, dwell, and ramping down) for soft-baking of ultrathick SU-8 film.

To accelerate the development process, ultrasonic agitation was recommended. Frequency of waver propagation is one of the most important factors. Williams et al. [35] demonstrated that with low frequency agitation (KHz range) , e.g. ultrasonic agitation, may cause vibrations, which subsequently leads to cracks, deformation and debonding. Therefore, megasonic agitation with frequency from 1 to 10MHz may be beneficial to obtain high-aspect-ratio structures. The structure with the aspect ratio about 30:1 for 630 μm tall crosses (see Fig. 2.5a) up to 60:1 for 600 μm tall cylinders (see Fig. 2.5b). The direction of wave propagation was also discussed. It is suggested that the wafer should be placed perpendicularly to the direction of waves in order to avoid destruction and de-bonding problem.

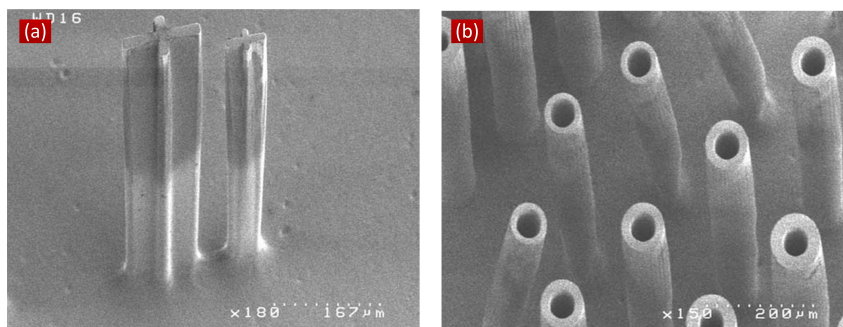


FIGURE 2.5: Lithography process: development with megasonic agitation. (a) crosses fabricated with 630 μm tall and 6 - 12 μm wide, aspect ratio is about 30, (b) cylinders fabricated with 600 μm tall and 10 - 15 μm wall thickness, aspect ratio is about 60. These figure has taken from [35].

With well-developed optimal lithography process for thick SU-8 film, number of fabricated microneedles have been reported. In 2010, Chaudhri et al. [20] introduced the studies on fabrication of high-aspect-ratio SU-8 microneedles. The 1600 μm tall microneedles were particularly constructed for blood sampling applications (see Fig. 2.6a). In their studies, a new process with dried chips SU-8 was introduced. SU-8 was firstly poured and baked for 12 hours on hot plate before being scraped off to obtain dried SU-8 chips. For further process, dried chips were placed on wafer and soft-baked with a vacuum oven at 110°C for reflowing. The process of dried SU-8 chips were applied by Ceyskens et al. [36] to construct a 1000 μm tall SU-8 microneedles with 15 μm wall thickness as shown in Fig. 2.6b. The beveled tips was created on one face of an wet-etched-silicon V-groove. After wet etching, the sample was covered with a Ti/Cu seed layer and Cr black deposition. With deposited metal layers, excellent sharp tips of 3 μm radius were able to create.

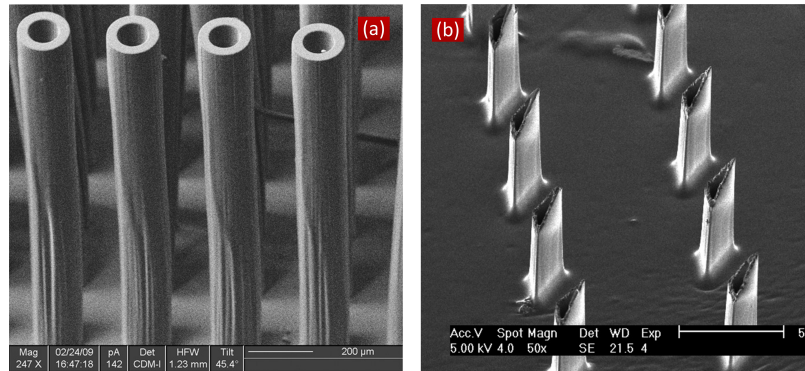


FIGURE 2.6: Recently proposed SU-8 microneedles for blood extraction. (a) microneedles fabricated by Chaudhri et al. [20] with $1540\mu\text{m}$ tall, $15\mu\text{m}$ wall thickness, aspect ratio is over 100, (b) ultrasharp SU-8 microneedles fabricated by Ceyssens et al. [36] with $1000\mu\text{m}$ tall, $15\mu\text{m}$ wall thickness, aspect ratio is over 65.

In conclude, the fabrication method with conventional lithography has been shown to be potentially feasible for the fabrication of ultrahigh hollow microneedles. With the optimal process parameters, high-aspect-ratio microneedles with excellent sharp tips are achievable. Additionally, a combination of conventional lithography and mold-based fabrication techniques (e.g. PDMS micromolds) is highly desirable for a simple, robust fabrication method suitable for inexpensive mass production.

2.2 Background

2.2.1 A rigid polymer: SU-8 2150

SU-8 is a epoxy-based photoresist originally developed and patented by IBM in 1989 [37, 38]. It has been commercialized by MicroChem Corporation in 1996 [39]. 3-dimensional high-aspect-ratio structures are achievable with SU-8 and conventional UV lithography. Microfabricated SU-8 structures have excellent mechanical properties and thermal stability which are highly desirable in permanent devices.

SU-8 consists of three main components: EPON SU-8 resin, solvent, and a photo-acid generator (PAG) that make SU-8 very viscous and sticky. Upon heating, solvents start to be evaporated, frequently leads to an increase in viscosity and hence thicker. SU-8 is a photosensitive polymer, it will cured under exposure with UV source. The UV exposure is typically performed using a mercury lamp for wavelengths from 320nm to 405nm. The UV absorption rate increases significantly with wavelengths below 350nm [31]. The desirable wavelengths for thick SU-8 lithography thus ranges from 365nm to 405nm.

SU-8 is a biocompatible polymer that has been used widely in biomedical applications. The biocompatibility of SU-8 was previously proved in may studies [40–42]. Cho et al. evaluated the biocompatibility in [40]. SU-8 based neural microprobes were implanted into transected

rat and stay there for four weeks. There is no sight of infection of tissues inflammation was recorded.

There are some alternatives for SU-8 for the fabrication of MEMS-based devices, including: PMMA (x-ray lithography) or photosensitive glass (UV lithography with wavelengths from 280nm to 320nm [43, 44]).

2.2.2 Structural analysis

With the practical implementation of microneedle arrays for collecting of blood, microneedle array will be ideally injected along its axis into human skin. In reality, during implementation of injection, skin resists with an external pressure, acting normally on force-applying area on microneedle tip. This external pressure can be expressed as a combination of two components i.e. vertical and horizontal forces. Therefore, two noteworthy failure mechanisms thus are critical buckling and brokenness due to bending force. Respectively, two noteworthy failure mechanisms thus are buckling and brokenness due to bending force.

Buckling is a phenomenon of sudden failure when an object is subjected to a compressive stress. To investigate the underlying mechanism of buckling, a secondary bending moment is introduced by an axial load eccentricity causing an instability at bottom of the structural member. i.e. brokenness and buckling. The definition of critical buckling load (P_{cr}) was firstly introduced by Euler way back to 1757 to describe the maximum axial load that structural member can withstand [45]. His proposed expression (2.1) for P_{cr} is simply for an approximate solution which can only apply for considered long objects with a constant cross section.

$$P_{cr} = \frac{\pi^2 EI}{L_e^2}. \quad (2.1)$$

However, in most of the cases, microfabricated microneedles are typically designed in more complicated shapes with extremely sharp tip and hollow structure, therefore, (2.1) cannot be applied in our case. In 1988, based on the theory of energy method, Smith [46] derived an exact solution for P_{cr} (2.2) which is applicable for varied cross-section area objects. Energy method indicates the failure point at which strain bending energy equals to work done by compressive load. This approach has been applied widely in structural analysis of microneedles [9, 47]. In this dissertation, Smith's formula is employed to verify the improved properties of the proposed pyramid-shaped microneedle.

$$P_{cr} = \frac{\pi^2 E}{2L^3} \int_0^L I(z) \cos^2 \left(\frac{\pi z}{2L} \right) dz. \quad (2.2)$$

As per two other failure mechanisms, bending force plays extremely crucial role toward successful skin penetration. Generally speaking, with structural members in the shaped of long, slender tube, maximum bending force (P_b) is much less than axial force at buckling (P_{cr}). To estimate P_b , Euler also introduced a simple formula (2.3) for an approximation of bending force. This approach has been applied as a good prediction for many previously proposed microneedles as presented in [48, 49].

$$P_b = \frac{\sigma_y I}{cL} \quad (2.3)$$

However, for an exact solution, the expression of F_b must be derived from the distributions of shear and normal stress [50]. This approach requires much more work and will be presented in chapter 3.

Chapter 3

Geometry Optimization

This chapter elucidates the failure mechanisms of microneedle during implementation. By studying the critical buckling load and bending strength of two proposed microneedle designs, including: pyramid-shaped microneedle (PMNs) and traditional-shaped microneedle (TMNs), an optimal geometry for designing the microneedles was proposed. The key contribution of this chapter is the proposed theoretical model for geometry optimization based on the study of fracture forces.

This chapter consists of four sections. Firstly, section 3.1 describes the proposed design of PMNs with pyramidal tip, off-center hollow and square base. These geometrical features are expected to improve the mechanical properties of PMNs. Secondly, section 3.2 presents the mathematical frameworks for structural analysis. The development of the proposed theoretical model is presented in this section. Thirdly, section 3.3 describes how the simulations were done with COMSOL simulator. Fourthly, section 3.4 presents the results from analytical and numerical solutions. The obtained results are discussed in this section. Finally, section ?? presents chapter conclusion and proposes the optimal design for microneedles.

3.1 Design of pyramid-shaped microneedles

In this section, a stiffer and more efficient microneedle was proposed with the following hypothesis of structural advantages. First, with square base, PMNs can tolerate higher axial and transverse forces because the inertia moment of square is approximately 1.69 times bigger than that of circle with the same dimension. Second, sharp pyramidal tip may reduce the insertion force thanks to small contact area. Moreover, pyramidal tip is expected to exhibit higher strength compared to the tip of TMNs and tapered hollow microneedle [9]. Third, the cylindrical lumen is not placed in the middle of the microneedle but in the side face of pyramidal tip, making the tip stronger. All above advantages of PMNs will be studied by the proposed theoretical model and subsequently by verified by finite element method and practical measurement of fracture force.

3.2 Analytical solution

3.2.1 Skin deformation and insertion force

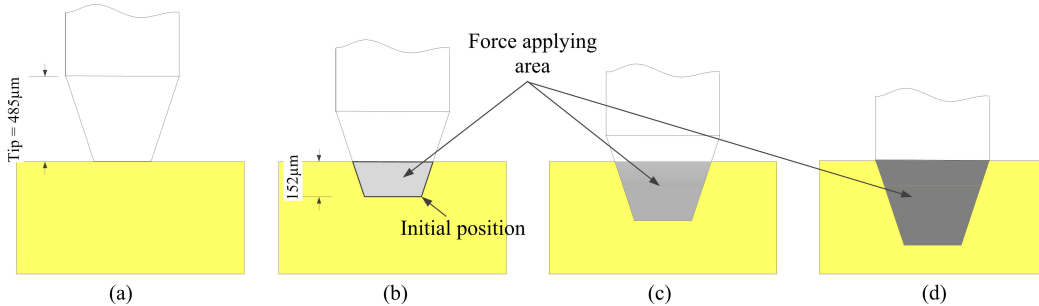


FIGURE 3.1: Illustration for microneedle insertion and skin deformation. The skin penetration is modelled at different penetration depth: (a) $X_0 = 0$, (b) $X_0 = 152\text{m}$, (c) $152\text{m} < X_0 < 485\text{m}$, (d) $X_0 = 485\text{m}$

In practical use, for bio-fluids extraction, microneedle is required to puncture the skin and inserted deeply into dermis layer where blood vessels are located. However, in reality, human skin is a heterogeneous, anisotropic and nonlinear viscoelastic material, in other words, it will be deformed before being punctured. Additionally, as we know, skin is a complex multi-layered structure which is quite complicated with different mechanical properties of each layer, e.g. first outermost layer: stratum corneum ($10\text{-}20\mu\text{m}$), second layer: epidermis ($50\text{-}150\mu\text{m}$), dermis ($1\text{-}4\text{mm}$) and hypodermis ($> 4\text{mm}$). For simplification, in this case skin is considered as a single layer structure with approximately the same mechanical strength. According to Kong [51], $152\mu\text{m}$ is the maximum skin deformation before being punctured. This value will be used in this research to calculate the initial area of applying forces. The entire process of skin penetration is presented below in Fig. 3.1.

Distributed bending force

When the needle is inserted into human skin, skin will be deformed before puncture actually happens. The actual force applied on the microneedle is a distributed force but concentrated force. Taking into account the effects of distributed will subsequently create more difficulty and complexity on further analysis of fracture force. The expressions of bending moments at two regions as shown in Fig. 3.2: $0 < x < X_0$ (point X_N) and $X_0 < x < \text{Tip}$ (point X_M) are derived as follows:

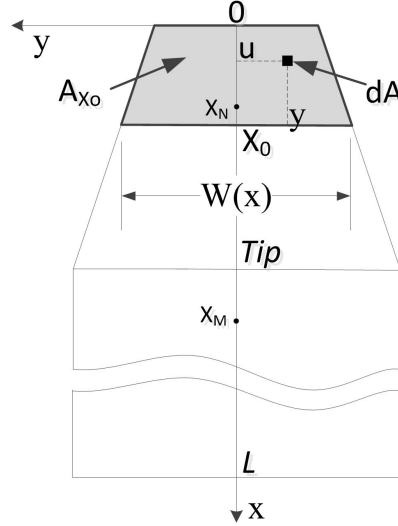


FIGURE 3.2: Illustrations for distributed bending force.

$$M_1(x) = P_{unit} \int_0^x \int_{-W(u)/2}^{W(u)/2} (x-u) dy du, \quad (3.1)$$

$$M_2(x) = P_{unit} \int_0^{X_0} \int_{-W(u)/2}^{W(u)/2} (x-u) dy du, \quad (3.2)$$

where P_{unit} is the force per unit area and $W(x)$ is the width corresponding to x . P_{unit} and $W(x)$ can be derived as follows:

$$W(x) = W_2 + \frac{W_1 - W_2}{Tip} x \quad (3.3)$$

$$P_{unit} = \frac{P_b}{A_{X_0}} = \frac{P_b}{\frac{W_{X_0} + W_2}{2} X_0}. \quad (3.4)$$

3.2.2 Mathematical frameworks

The objective of this section is to propose an optimal design of PMNs. One frequently-used approach is to minimize the failure possibility to ensure as high safety as possible. In our experiments, a negative tone photoresist SU-8 2150 was used to fabricate microneedle arrays. One mechanical issue associated with SU-8 microneedles is brokenness. After PEB

and especially hard baking, microneedles become harder but more brittle [52, 53], leading to subsequently high failure possibility. Being made from brittle materials, microneedles are most likely to be fractured than yield [54]. Therefore, two following mechanisms will be respectively considered: critical buckling load and maximum bending force resulted from shear stress. The theoretical predictions are subsequently verified by simulational results, followed by a sectional discussion that proposes an ultimate design of PMNs. The strategy for evaluating mechanical strength of our proposed microneedle is to estimate failure forces by using Euler's elastic theory. As may be noticed before, in elastic buckling model, Euler's beam theory can only apply for "long" column which has slenderness ratio (S) larger than critical slenderness ratio (S_{cr}). The formulas for S and S_{cr} are expressed as follows:

$$S = \frac{L_{eff}}{r_g} = \frac{2.1L}{\sqrt{\frac{I_{min}}{A}}}, \quad (3.5)$$

$$S_{cr} = \sqrt{\frac{2\pi^2 E}{\sigma_y}}, \quad (3.6)$$

where L_{eff} is the effective length for fixed-free column, r_g is radius of gyration, I_{min} is the minimum inertia moment, A is cross section area, E and σ_y are Young's modulus and yield strength of the material, respectively. For short and intermediate regions (i.e. $S \leq S_{cr}$), there is no exact solution for calculating critical buckling load except approximate models. Three frequently-used models are Johnson's linear (tough materials), parabolic formulas (brittle materials), and Secant's formula (eccentrically loaded). Previously, Zahn et al [48] also used Johnson's parabolic formula to estimate critical buckling load of his in-plane microneedles. In this paper, SU-8 2150 is used to fabricate our proposed microneedles with the mechanical properties of $E = 4.02\text{GPa}$ and $\sigma_y = 34\text{MPa}$. With $L = 1800\mu\text{m}$, $S_{cr} = 48.3$ is obtained by using (3.6) and S can be calculated using (3.5). S is varied due to an increase in base width (W_1). This relationship is demonstrated in Table I and in Scenario 1. The values of critical buckling load obtained from Euler and Johnson models are illustrated in Fig. 4. P_{cr} calculated with Johnson's formula critical buckling load of the proposed design is 3.4%, which is smaller than P_{cr} obtained from (3) when $W_1 = 300\mu\text{m}$. Therefore, Euler's theory is still applicable for further calculations of critical buckling load with the error span of 3.4%.

3.2.2.1 Analysis of critical buckling load

In practice, microneedle is desirably designed to pierce deeply into the dermis layer to reach the blood vessels. During penetration process, the skin acts as a mechanical barrier, resisting the insertion of microneedle. Skin resistance is modeled as axial and horizontal forces which may make micro-needle bend or break. At failure point, these forces are called critical buckling load (P_{cr}) and maximum bending force (P_b). The expression of P_{cr} can be derived by applying

energy method as shown in (3.7).

$$P_{cr} = \frac{\pi^2 E}{2L^3} \int_0^L I(x) \cos^2 \left(\frac{\pi x}{2L} \right) dx. \quad (3.7)$$

To apply (3.7) particularly for the PMN structure, the expressions of $(I_z(x))$ must be derived. The procedure for calculating $(I_z(x))$ is based on adding/subtracting the inertia moment of basic shapes (e.g. circle, circular sector, triangle...etc.). The detailed derivations of $I_z(x)$ will be presented in next section and in Appendix A. The x-dependent functions of inertia moments are highly complex, therefore, the final expression to calculate P_{cr} becomes very complicated and hard to compute manually. All the computations were conducted by programming in Maple.

3.2.2.2 The proposed theoretical model for analysis of bending strength

The second failure mechanism is due to transverse force, i.e. bending force. Typically, bending force is most likely to induce fracture at the microneedle shaft at which is subjected to the largest bending moment. However, microneedle tips are considerably breakable due to diminutive tip-size (40μm). The possibility of tip failure may be subsequently higher than that of shaft failure. In this paper, we developed a theoretical model to compute the magnitude of shear stress when the microneedle is subjected to a distributed bending force. With higher applicability to various structural designs, this model may predict more accurately the fracture bending force. With the illustration shown in Fig. 3.3, the equation of stress balance in x-direction was derived and presented in (3.8).

$$\int_A \sigma dA + \tau_{xy} A_{xy} = \int_{A+dA} (\sigma + d\sigma) dA, \quad (3.8)$$

$$\Rightarrow \int_A \sigma dA + \tau_{xy} D(x, y) dx = \int_{A+dA} (\sigma + d\sigma) dA, \quad (3.9)$$

$$\Rightarrow \int_{A+dA} \left(\frac{M(x)}{I_z(x)} + d \left(\frac{M(x)}{I_z(x)} \right) \right) - \int_A \frac{M(x)}{I_z(x)} y dA = \tau_{xy} D(x, y) dx, \quad (3.10)$$

In (3.9) and (3.10), $D(x,y)$ is defined as the width corresponding to differential dx (see Fig. 3.3). $M(x)$ is the moment in the cross section current. $I_z(x)$ and $Q_z(x,y)$ are the second moment of area (inertia moment) and the first moment of shaded area (Fig. 3.3a) with respect to neutral axis z , respectively.

$$\Rightarrow \left(\frac{M(x)}{I_z(x)} + d \left(\frac{M(x)}{I_z(x)} \right) \right) \int_{A+dA} y dA - \int_A \frac{M(x)}{I_z(x)} y dA = \tau_{xy} D(x, y) dx, \quad (3.11)$$

$$\left(\Rightarrow \frac{M(x)}{I_z(x)} + d \left(\frac{M(x)}{I_z(x)} \right) \right) (Q_z(x, y) + dQ_z(x, y)) - \frac{M(x)}{I_z(x)} Q_z(x, y) = \tau_{xy} D(x, y) dx, \quad (3.12)$$

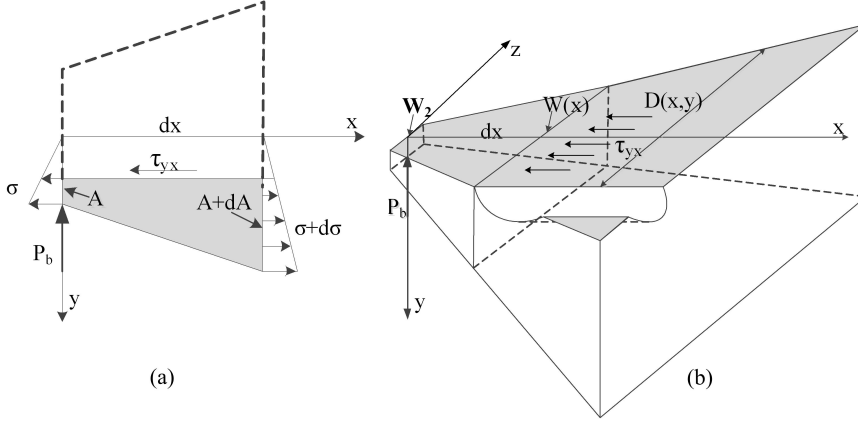


FIGURE 3.3: Illustrations for stress distribution on pyramidal tip. (a) normal stress and shear stress in xOy plane. (b) 3D distribution of shear stress (τ_{yx}) in xOz plane. σ and $\sigma+d\sigma$ are normal stress acting on area A and $A+dA$, respectively. P_b represents for distributed bending force.

$$\Rightarrow \frac{M(x)}{I_z(x)}Q_z + \frac{M(x)}{I_z(x)}dQ_z + d\left(\frac{M(x)}{I_z(x)}\right)Q_z + d\left(\frac{M(x)}{I_z(x)}\right)dQ_z - \frac{M(x)}{I_z(x)}Q_z = \tau_{xy}D(x,y)dx. \quad (3.13)$$

By neglecting high-order differential terms, (3.13) can be simplified as

$$\Rightarrow \frac{M(x)}{I_z(x)}dQ_z + d\left(\frac{M(x)}{I_z(x)}\right)Q_z = \tau_{xy}D(x,y)dx. \quad (3.14)$$

The expression of shear stress can be obtained from (3.14) as follow:

$$\tau_{xy} = \frac{1}{D(x,y)} \left(\frac{M(x)}{I_z(x)} \frac{dQ_z}{dx} + Q_z \frac{d}{dx} \left(\frac{M(x)}{I_z(x)} \right) \right). \quad (3.15)$$

The unknown components in (3.15) are $I_z(x)$, $Q_z(x,y)$ and $D(x,y)$. In this section, to understand the procedure to calculate those components, detailed derivations for region 1, the simplest region in Fig. 3.4), were conducted. Calculation for the rest (i.e. region 2-5 in 3.4) will be presented in Appendix A. The magnitude of τ_{yx} can be obtained by solving (3.15) with the insertion of all necessary components. However, mathematical calculations become more complicated and τ_{yx} difficult to compute manually due to the dependence of $I_z(x)$, $Q_z(x,y)$, $M(x)$ and $D(x,y)$ on x and y . Therefore, all detail calculations were performed by programming in Maple.

Region 1: x from Tip to L

1. Second moment of area $I_z(x)$:

$$I_1 = \frac{W_1^4}{12} - \frac{\pi}{4} \frac{D_1^4}{2} \quad (3.16)$$

2. First moment of area $Q_z(x,y)$:

- y from 0 to R_1

$$Q_{1a}(x,y) = Q_{A_3} + Q_{A_2} - Q_{A_1}$$

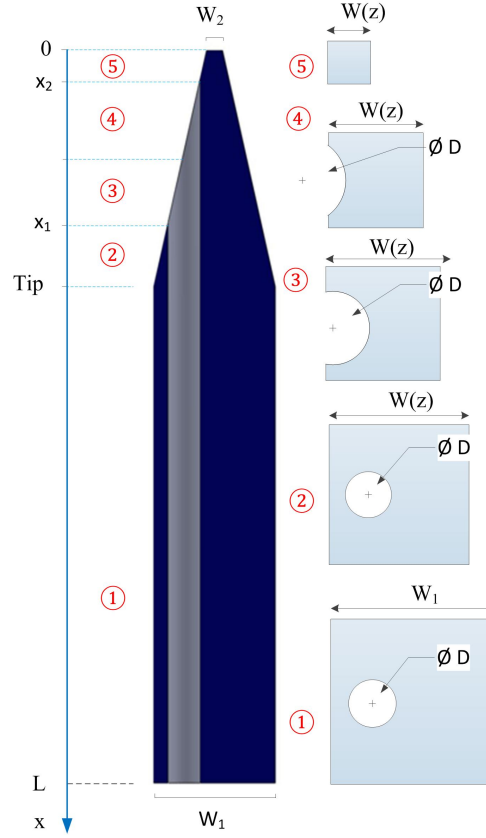
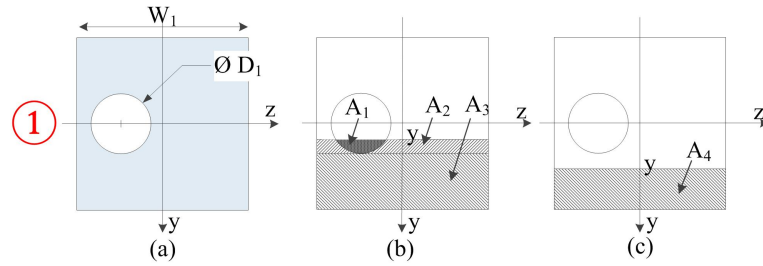


FIGURE 3.4: Illustrations for five cross sections of PMNs.

FIGURE 3.5: Cross section at region 1. (a) inertia moment, (b), (c) illustrate for Q_{1a} and Q_{1b}

$$Q_{1a}(x, y) = W_1 \frac{\frac{W_1^2}{4} - y^2}{2} + W_1 \frac{\frac{W_1^2}{4} - R_1^2}{2} - \int_{\sqrt{-R_1^2 - y^2}}^{\sqrt{R_1^2 - y^2}} \int_y^{\sqrt{R_1^2 - z^2}} y dy dz \quad (3.17)$$

- y from R_1 to $W_1/2$

$$Q_{1b}(x, y) = Q_{A_4}(x, y) = W_1 \frac{\frac{W_1^2}{4} - y^2}{2} \quad (3.18)$$

3. Width $D(x, y)$ corresponding to differential dx :

- y from 0 to R_2

$$D_{1a}(x, y) = W_1 - 2\sqrt{R_1^2 - y^2} \quad (3.19)$$

- y from R_1 to $W_1/2$

$$D_{1b}(x, y) = W_1 \quad (3.20)$$

3.3 Numerical solution

The finite element method was applied to study the mechanical behavior of the proposed microneedles. The theoretical results were verified by COMSOL simulator under the same following boundary conditions: the whole structure is free while the bottom is set to be fixed constraint. The magnitude of shear stress was extracted from the stress tensor as illustrated in Fig. 3.6b. The maximum value of shear stress was obtained by considering the volume maximum.

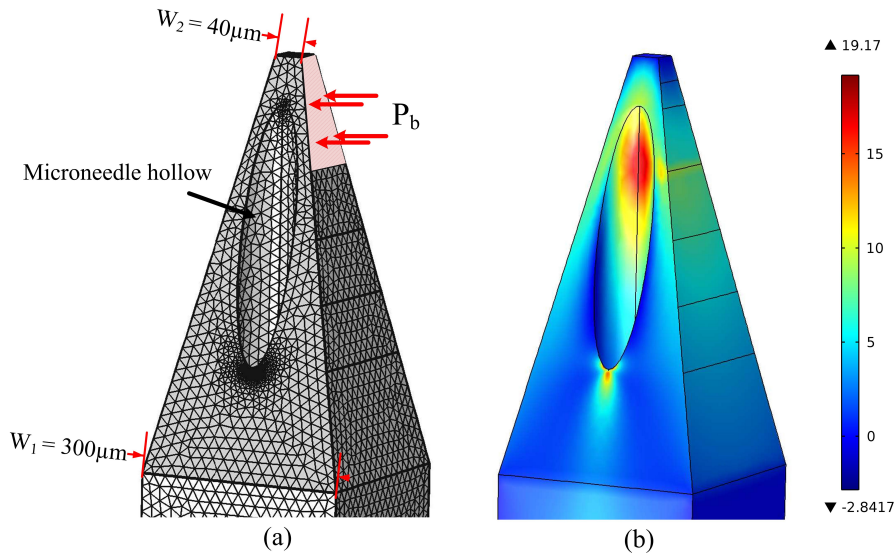


FIGURE 3.6: Finite element method with COMSOL simulator on PMNs ($L = 1800\mu\text{m}$, $D = 80\mu\text{m}$). Distributed bending force $P_b = 0.105\text{N}$ is applied on the shaded area. (a) Extra fine mesh for simulation with the minimum element size of $2.7 \times 10^{-6}\text{m}$, (b) Simulation results: distribution of shear stress. $(\tau_{xy})_{\text{max}} = 19.17\text{MPa}$.

Optimization of mesh size: the element size was calibrated for general physics. The mesh size was optimized by conducting five studies on five mesh sizes, including: fine, finer, extra fine, extremely fine and 1/2 size of extremely fine. The illustrations corresponding to five mesh sizes are shown in Fig. 3.7. In each study, the magnitude of maximum shear stress was recorded and presented in Table 3.1. The maximum value of shear stress (τ_{xy}) was recorded. As can be seen in Table 3.1, the magnitude of shear stress begins to converge in the last three test cases (Simulation No. 3-5). In addition, the simulation running on Simulation No. 4 and 5 required much longer processing time in compared to the first three scenarios. In fact, the simulation is not required to be highly accurate. By considering the accuracy and processing time, in conclude, the mesh size named extra fine (Simulation No. 3) was chosen for conducting all simulations in this thesis.

TABLE 3.1: Optimization of mesh size. The mesh size was utilized with the calibration of General Physics. Distributed bending force ($P_b = 0.105\text{N}$) was applied in the shaded area as shown in Fig. 3.6a.

Simulation No.	Mesh Size		$(\tau_{xy})_{\max}$ (MPa)	Illustrated in Fig. 3.7
	Name of mesh	Minimum element size		
1	Fine	1.8×10^{-5}	18.73	<i>a</i>
2	Finer	7.2×10^{-5}	18.95	<i>b</i>
3	Extra fine	2.7×10^{-6}	19.17	<i>c</i>
4	Extremely fine	3.6×10^{-7}	19.20	<i>d</i>
5	1/2 extremely fine	1.8×10^{-7}	19.21	<i>e</i>

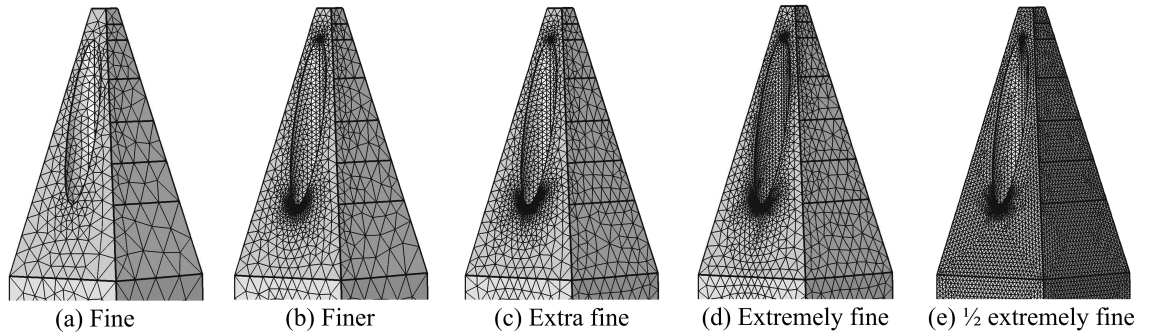


FIGURE 3.7: Optimization of simulation mesh with five mesh sizes: (a) fine, (b) finer, (c) extra fine, (d) extremely fine, (e) 1/2 extremely fine.

3.4 Results and Discussion

In this section, the improved mechanical properties of PMNs will be demonstrated with the results from mathematical calculations and numerical simulations. The following geometrical values as being relevant for geometry optimization: base width (W_1), length (L) and hollow diameter (D). Performance evaluation of PMNs will be conducted with three main scenarios of critical buckling load, shear stress and normal stress due to bending force.

3.4.1 Failure Mechanism 1: Critical Buckling Load

To predict the failure force due to buckling, energy method was utilized. The proposed PMNs has five regions of cross section area as depicted in Fig. 3.4. By studying P_{cr} as a function of base width (W_1) and length (L), then P_{cr} will be compared to the minimum insertion force of 31.8MPa [55], the first design criterion for axial force can be obtained. In this scenario, the values of P_{cr} were recorded with the variations in W_1 for two cases: $L = 1800\mu\text{m}$ and $L = 1500\mu\text{m}$. The results are shown in Fig. 3.8. It can be observed that PMNs can endure higher axial force at all W_1 compared to TMNs, with 2.32N and 2.94N and 1.08N and 1.5N when

$W_1 = 300\mu\text{m}$, $L = 1800\mu\text{m}$ and $L = 1500\mu\text{m}$, respectively. This implies that the proposed PMNs may have better mechanical properties in term of fracture strength against axial force.

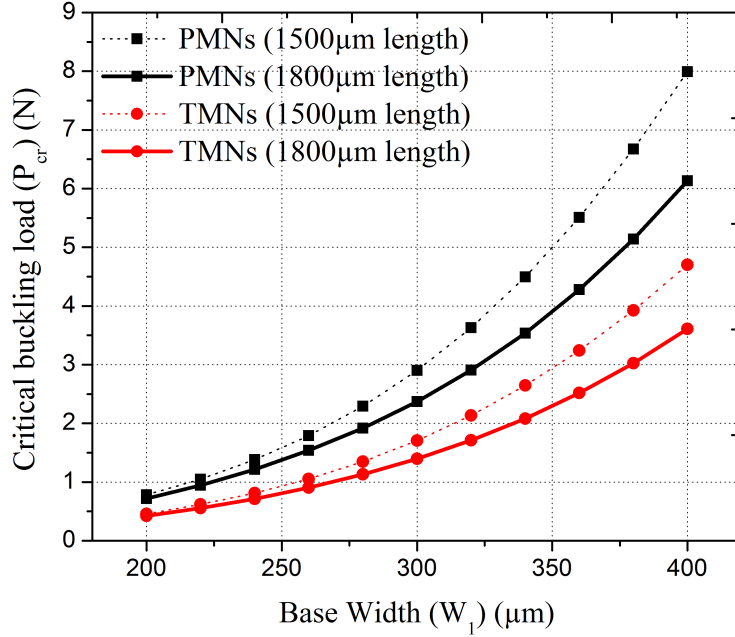


FIGURE 3.8: Critical buckling load versus base width and length.

3.4.2 Failure Mechanism 2: Maximum bending force

Base on derived formula 3.15, 3D distribution of shear stress was built in Maple as shown in Fig. 3.3b. The 3D image was built for the shear stress distribution at the pyramidal tip. The coordinates are depicted in Fig. 3.3c with x varies from 0 to $485\mu\text{m}$, y from 0 to $150\mu\text{m}$ and z presents for shear stress magnitude. Shear stress is assumed to have a constant value in z -axis, and is symmetric about y -axis.

To study the effects of bending force, three scenarios were performed. First, scenario 1 presents the matching of analytical and numerical solutions. Second, scenario 2 studies the relationship between $(\tau_{xy})_{\max}$ and hollow diameter (D) or base width (W_1). Third, scenario 3 predicts the maximum bending force (P_b) that the microneedle can endure. All scenarios were conducted with an increased penetration depth (X_0). It means that the force applying areas is enlarged as X_0 increases i.e. microneedle is incrementally inserted into the human skin. At each of five considerable points correspond to five values of X_0 from $56\mu\text{m}$ to $485\mu\text{m}$. The values of $(\tau_{xy})_{\max}$ will be recorded and presented as a function of X_0 .

Scenario 1: *Matching of analytical and numerical solutions*

To evaluate the proposed theoretical model, verification with a finite element method is highly desirable. In this case, COMSOL simulator was utilized. The accuracy of the proposed model was evaluated through the matching between the magnitude of shear stress obtained from analytical solution and numerical solution. According to the results, as shown in Fig. 3.9 and Fig. 3.10, a good agreement was achieved.

Firstly, the general matching trend is considered. In Fig. 3.9b, two critical points were detected, including: 1st MAX (global maximum at X_0) and 2nd MAX (local maximum at diminutive edge). These points can also be observed from simulation results as depicted in Fig. 3.9a. Therefore, one thing can be concluded is that the proposed theoretical model can predict the general trend of shear stress distribution.

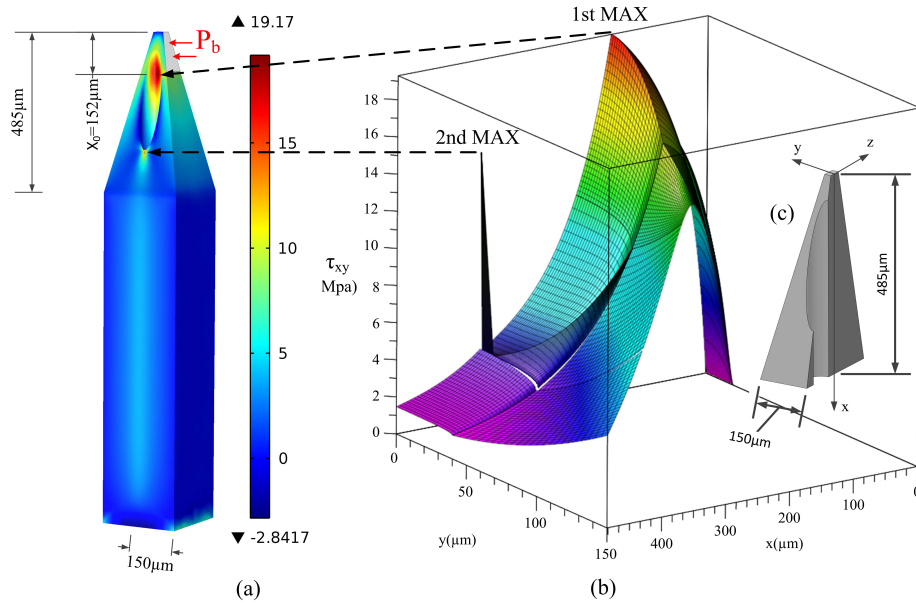


FIGURE 3.9: Scenario 1: Matching of analytical and numerical solutions. A distributed bending force $P_b = 0.105\text{N}$ is applied in the shaded area ($X_0=152\text{m}$). (a) 3D distribution from simulation results, (b) 3D distribution built by theoretical model for the tip of PMNs, (c) illustration for system coordinates. Distribution of xy is presented in x - y coordinates and it is assumed to be uniform in z -direction and symmetric about the y -axis. There are two critical points with highest values of τ_{xy} , e.g. 1st MAX (global maximum at X_0) and 2nd MAX (local maximum at diminutive edge).

Secondly, for statistical evaluation, a scenario studying the relationship between $(\tau_{xy})_{\max}$ and X_0 was conducted. The results are shown in Fig. 3.10 and Table 3.2. From the red lines in Fig. 3.10, a very good matching between two solutions is observed at 1st MAX point with $\bar{\Delta} = 6.9\%$. On the other hand, this number is $\bar{\Delta} = 20.5\%$ for 2nd MAX point. This number implies that shear stress prediction for 2nd MAX point is not as accurate as for 1st MAX point. One possible explanation is the effect of concentrated stress at 2nd MAX point. In fact, in the ideal sketch, at 2nd MAX point, stress is distributed in diminutive area (see 2nd MAX point in Fig. 3.9a). Because of the fact that at diminutive features (e.g. sharp edge), it is very difficult to calculate the exact value of stress. Moreover, magnitude of concentrated stress is normally very high.

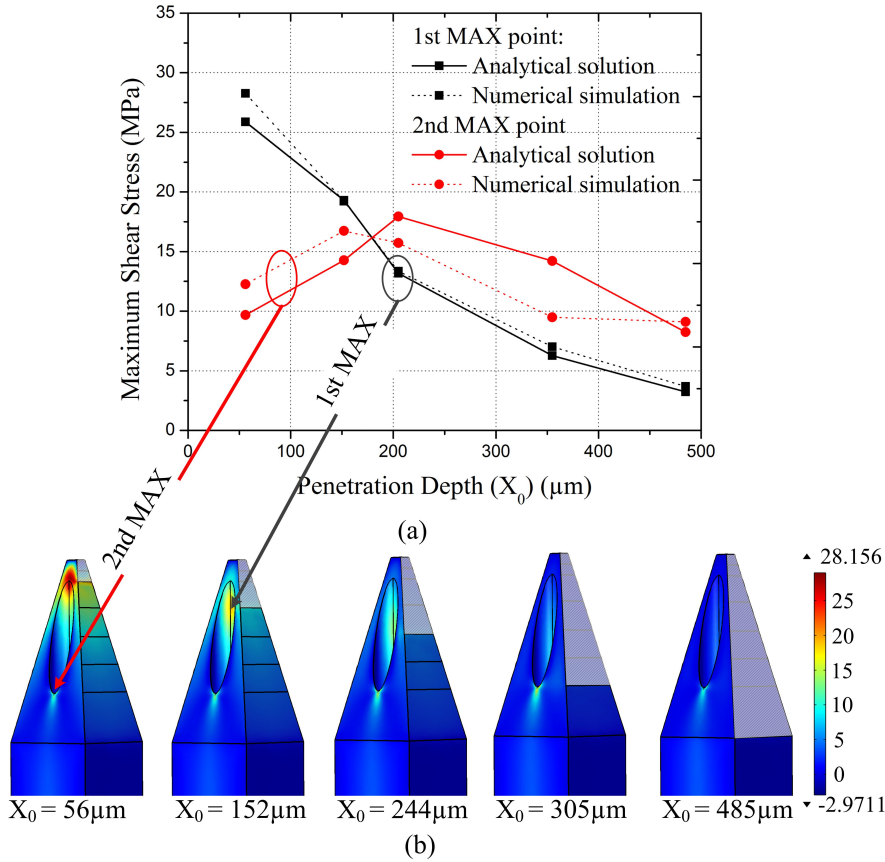


FIGURE 3.10: Scenario 1: Matching between analytical and numerical solutions - graphical analysis. (a) 2D plot of the matching of τ_{xy} magnitude at 1st and 2nd MAX point, (b) 3D distribution of τ_{xy} from simulation with X_0 : $56\mu\text{m}$ - $485\mu\text{m}$. The shaded areas illustrate the force-applying area of a 0.105N distributed bending force.

TABLE 3.2: Scenario 1: Statistical analysis of the matching between analytical and numerical solutions. Matching of $(\tau_{xy})_{\text{max}}$ obtained from analytical and numerical solutions at two critical points: 1st MAX and 2nd MAX.

	1st MAX			2nd MAX		
	Analytical	Numerical	$\bar{\Delta}$ (%)	Analytical	Numerical	$\bar{\Delta}$ (%)
	25.88	28.26	8.78	9.68	12.26	23.50
	19.23	19.17	0.31	14.27	16.74	15.90
	13.18	13.35	1.30	17.95	15.72	13.27
	6.27	7.01	11.18	14.21	9.49	39.83
	3.24	3.70	13.09	8.25	9.11	9.95
Average			6.93			20.50

In practice, however, the microneedles cannot be fabricated with a perfect sharp features, for example the edge at 2nd MAX point. So, to study the effect of sharp edge on shear stress value, a follow-up scenario was conducted and the results are shown in Fig. 3.11. In Fig. 3.11, a 0.105N distributed bending force is applied at $X_0 = 152\mu\text{m}$. The sharp edge at 2nd MAX point is rounded with the radius of $5\mu\text{m}$. The magnitude of shear stress at 2nd MAX point reduced significantly from 16.7MPa to 6.8MPa with rounded edge ($r = 5\mu\text{m}$). On

the other hand, at 1st MAX point, the shear stress remained stable with the magnitude of approximately 19.1MPa. So, it can be concluded that the fracture at 2nd MAX point would not occur in practical implementation. The only critical point to be considered is at 1st MAX point.

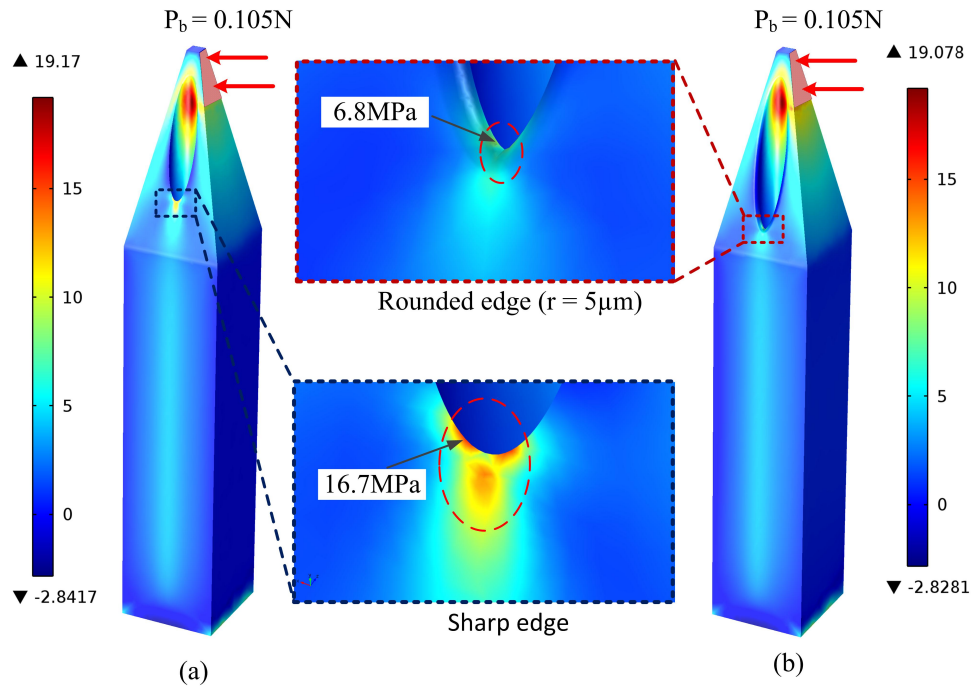


FIGURE 3.11: Scenario 1: The effect of sharp edge on the magnitude of shear stress. The values of maximum shear stress between (a) sharp edge, (b) rounded edge (rounded radius = $5\mu\text{m}$) at 2nd MAX point was recorded.

Scenario 2: Effects of microneedle geometry

To study the effects of microneedle dimensions on the magnitude of shear stress, two studies were conducted with the variations of X_0 at different values of hollow diameter (D) and base width (W_1). The results are shown in Fig. 3.12. The presented values of $(\tau_{yx})_{\text{max}}$ was deduced by taking the average numbers of calculated results and simulated results. One general trend can be observed in Fig. 3.12 that $(\tau_{yx})_{\text{max}}$ decreased slightly when D increased and W_1 increased. However, at low penetration depth ($X_0 < 250\mu\text{m}$), value of D and W_1 induced more impact on τ_{yx} . Therefore, the tip part is most likely to be broken when force is initially applied ($X_0 < 152\mu\text{m}$). In general, at puncturing point (i.e. $X_0 = 152\mu\text{m}$), the value of $P_b = 0.105\text{N}$ which is higher than 0.084N as presented in Paper P2. In addition, bending strength becomes higher at deeper penetration depth.

Scenario 3: Maximum bending force

After $(\tau_{yx})_{\text{max}}$ was calculated, P_b can be deduced by comparing $(\tau_{yx})_{\text{max}}$ to the shear strength of SU-8. In this scenario, P_b was studied with the variations in base width (W_1) and penetration depth (X_0). Fig. 3.13 presents the magnitude of P_b when W_1 varies from $225\mu\text{m}$ to $400\mu\text{m}$ and X_0 increases from $152\mu\text{m}$ to $485\mu\text{m}$. The general trend can be observed in Fig.

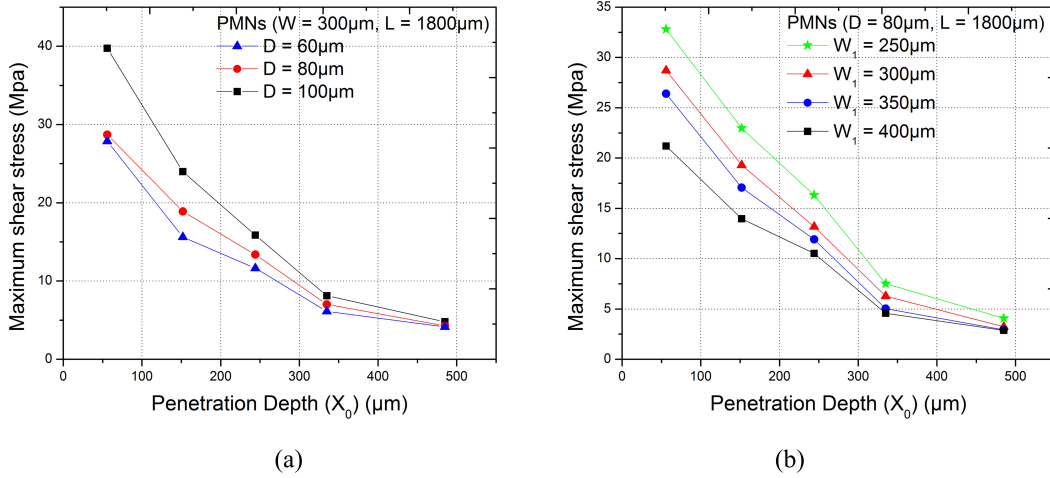


FIGURE 3.12: Scenario 2: Effects of microneedle geometry on the magnitude of shear stress. Maximum shear stress as a function of X_0 at (a) three different values of hollow diameter (D), (b) four different values of base width (W_1).

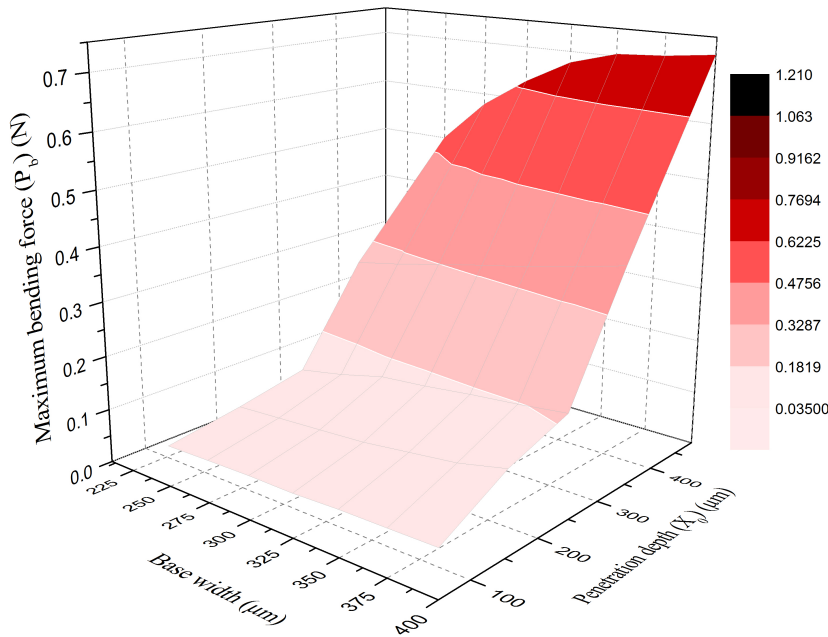


FIGURE 3.13: Scenario 3: Prediction of maximum bending force. 3D illustrations of the relationship between P_b , W_1 and X_0 .

3.13 that bending strength increase significantly with the increasing penetration depth. The maximum and minimum of P_b is about 1.21N ($X_0 > 485\mu\text{m}$) and 0.09N ($X_0 = 152\mu\text{m}$). The values indicate that microneedles were potentially breakable at the initial stage of penetration i.e. when the microneedles were firstly inserted.

Fig. 3.14 compares the bending strength of two proposed microneedle designs. As expected, PMNs may have higher bending strength with about 0.7N compared to 0.14N of TMNs (X_0

$= 485\mu\text{m}$, $W_1 = 300\mu\text{m}$). The pyramidal tip is theoretically expected to be stronger than bevel tip of TMNs. The practical verification will be presented in chapter 5.

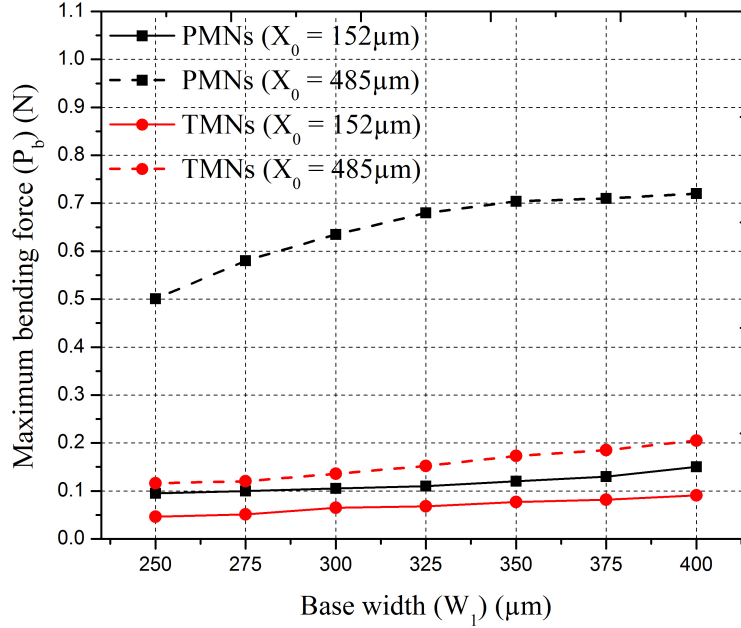


FIGURE 3.14: Comparison between P_b of PMNs and TMNs with the variation in base width.

3.4.3 Insertion Force

To ensure the fracture will not occur during operation, the statistical understanding of required insertion force (P_{insert}) to puncture human skin is highly desirable. It has been stated in [56] that the required pressure to puncture the human skin is about $3.18\text{MPa} = 3.18 \times 10^{-8}\text{N}/\mu\text{m}^2$. The insertion force, therefore, can be calculated by multiplying the required pressure to insertion area (A_{insert}) to $3.18 \times 10^{-8}\text{N}/\mu\text{m}^2$. The results are shown in Table 3.3. The insertion force was estimated corresponding to different penetration depth as depicted in Fig. 3.15. The results illustrated that the magnitude of P_b is much bigger than P_{insert} at all values of X_0 . Therefore, the proposed microneedles are expected not to be broken during skin penetration.

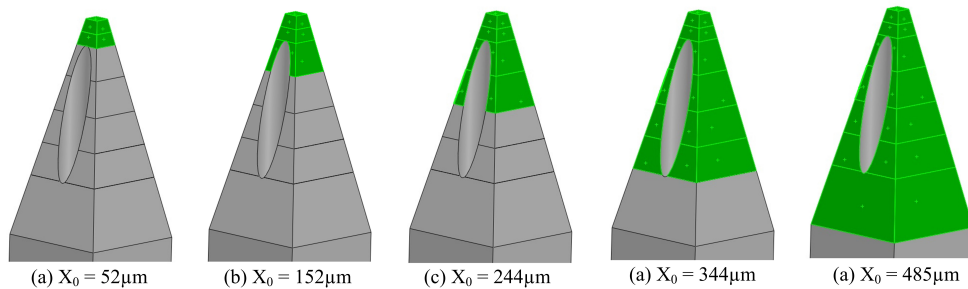


FIGURE 3.15: Illustrations for force applying area (A_{insert}) at different penetration depth.

TABLE 3.3: Estimation of required insertion force to puncture human skin. The values of P_b were taken from Fig. 3.13.

X_0 (μm)	A_{insert} (μm^2)	Insertion pressure ($\text{N}/\mu\text{m}^2$)	P_{insert} (N)	P_b (N)
52	17164	3.18×10^{-8}	0.00055	0.079
152	43540	3.18×10^{-8}	0.00138	0.105
244	85103	3.18×10^{-8}	0.00271	0.155
335	209777	3.18×10^{-8}	0.00667	0.328
485	382833	3.18×10^{-8}	0.01217	0.635

3.5 Chapter conclusions

According to the results from theoretical calculations and simulations, PMNs may be stronger than TMNs in term of force endurance. The results showed a good agreement between analytical and numerical solutions. The improved properties were verified through the studies in fracture forces. By comparing to the estimated insertion force (see Table 3.3), the fracture forces are much bigger than the required insertion force. Therefore, the proposed design of microneedle may successfully puncture the skin without failure. Further verification with practical measurements of fracture force will be presented in Chapter 5.

In relation to the limitations of the proposed theoretical models, Euler's beam theory is with several assumptions on the aspect ratio, slenderness ratio with the elimination of shear deformation. With short or immediate structural members, the effects of shear force on deformation have to be addressed. For further study, the beam theory developed by Timoshenko can be utilized for more accurate results. Fig. 3.16 illustrates the difference between Euler's Beam theory and Timoshenko's beam theory [57]. It can be seen that at the beam deformation is not normal to the beam axis, it is called shear deformation. Based on the obtained data

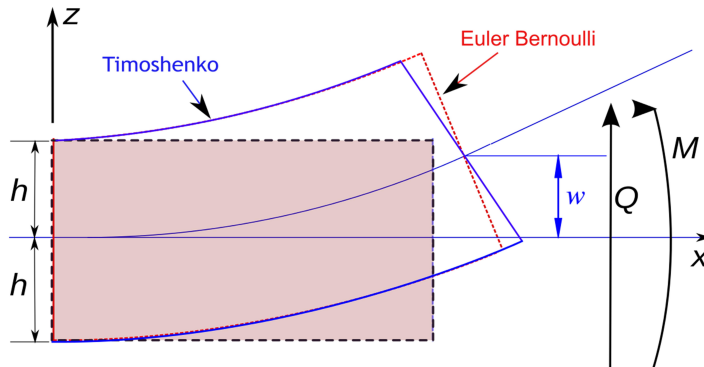


FIGURE 3.16: Deformation of a Timoshenko beam (blue) compared with that of an Euler-Bernoulli beam (red).

of fracture forces, an optimal geometry for a single PMNs is introduced with the following features (as depicted in Fig. 3.17a):

1. *Microneedle length* (L): $1500\mu\text{m}$ to $1800\mu\text{m}$.
2. *Base width* (W_1): $300\mu\text{m}$ square.
3. *Microneedle tip* (W_2): $40\mu\text{m}$ square.
4. *Microneedle hollow* (D): $80\mu\text{m}$ to $120\mu\text{m}$. In practice, the hollow diameter has to be carefully considered with the fabrication ability, especially for high aspect ratio structures. Small hollow may be very challenging to fabricate due to the limitations of UV lithography with SU-8, such as: SU-8 UV light absorption, light scattering and diffraction.
5. *Tip angle* : 25 to 30 degree angle. To fabricate the pyramidal tips, inclined exposure is utilized. The tip angle depends on the mechanical structure of the Karl Suss. Moreover, light refraction reduces the incident angle of UV light travel in SU-8 photoresist layer.

In practical use, syringe pump connected to a 1mm-inner-diameter polymer tube is used to generate suction pressure. The integration device (see Fig. 3.17b) is design with three parts including: SU-8 based microneedle array, PDMS plate and polymer tube. In addition, an

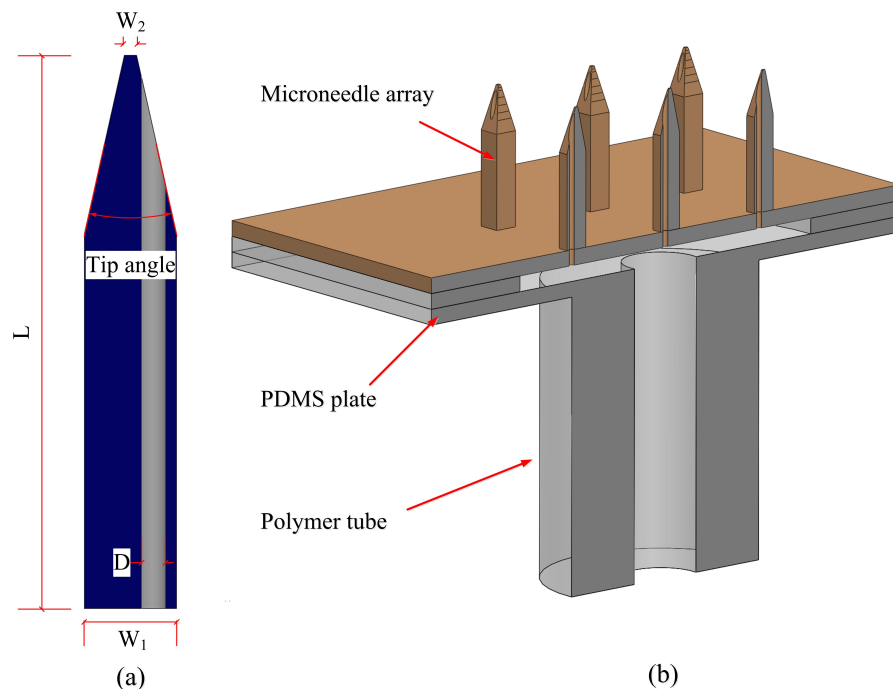


FIGURE 3.17: Integration of microneedles array. (a) One single microneedle, (b) An integration of microneedles array. The microneedle array is fixed to a PDMS plate (mounted with a polymer tube). The integration needs to be sealed appropriately to avoid leakage problem.

array of 9 microneedles may need to perform better collection of blood. In mechanical point of view, the microneedle array may withstand higher applied force than individual needles. The applied force will distributed uniformly on the array, thus reduce the pressure put on each needle [5]. To fabricate the microneedle array, the photomasks are simply designed with 9 microneedles on one array. The ultimate goal of microneedle array is to safely puncture the

skin and successfully withdraw blood. Therefore, to minimize the insertion force, microneedle array also need to be designed carefully. In fact, the numbers of microneedles on an array and the center-to-center spacing can affect directly to the success rate of skin penetration. If the microneedle arrangement is too dense, insertion force will significantly increase. On the other hand, sparse arrangement is space-consuming and it may reduce the mechanical endurance of microneedles. Center-to-center spacing (pitch) needs to be controlled based on microneedle height. In conclude, an optimal value for microneedle pitch is chosen to be $2000\mu\text{m}$ for $1500\mu\text{m}$ -high microneedles [58, 59].

Chapter 4

Fabrication of Microneedles

This chapter aims to develop a simple, inexpensive method with high throughput and repeatability for fabrication of microneedles. Two methods were proposed, including: replication of microneedles (method 1) and direct formation of microneedles (method 2). Method 2 is the contribution in the experimental part in this thesis. In addition, this chapter also addresses some practical issues associated during the manufacturing process. In summary, the main contributions of this chapter are listed as follows:

Contribution C2: A simple, robust method with high throughput and good repeatability to fabricate microneedles on CNC-machined aluminum sample.

Contribution C3: A solution, namely "separated lines", to solve the problem of wafer bending caused by CTE mismatch between SU-8 and silicon wafer.

This chapter is organized with five sections. Section 4.1 describes the concepts of two proposed fabrication methods and the idea to perform inclined exposure with a CNC-machined aluminum holder. Section 4.2 addresses three fabrication issues associated during microneedle fabrication. Section 4.3 describes the optimal lithography process for ultrathick SU-8 on aluminum substrate. Section 4.4 and section 4.5 present the experiments conducted to fabricate PMNs and TMNs, respectively. Section 4.6 gives a conclusion on the experiment part.

4.1 Fabrication concepts

This section describes the concepts of two methods which were utilized to realize the proposed microneedles, including: replication of microneedles (method 1) and direct formation of microneedles (method 2). In my experiments, method 1 was applied to fabricate pyramid-shaped microneedles (PMNs), and method 2 was applied to fabricate traditional-shaped microneedles (TMNs). This part also presents the design of aluminum holder which was used to perform inclined exposure.

Inclined exposure technique is the core ideal to construct the tip-formation structures i.e. pyramidal trenches for PMNs and bevel tips for TMNs. The expected outcomes and challenges of each method will be discussed.

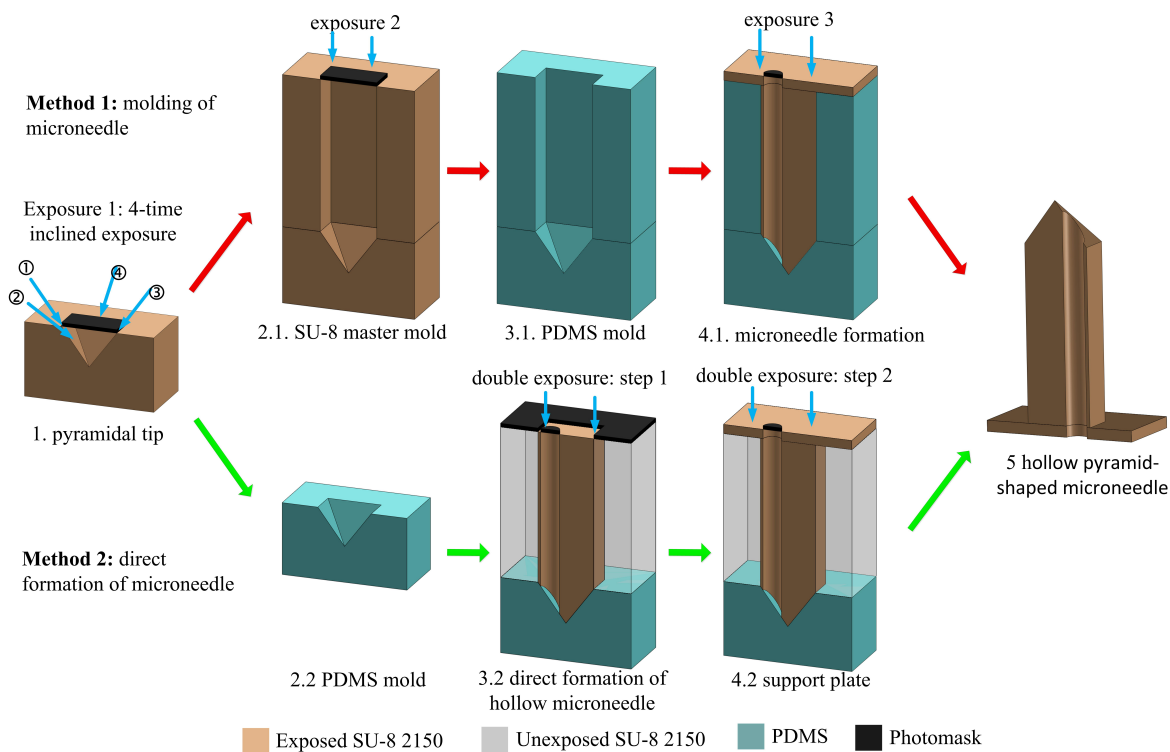


FIGURE 4.1: Process flow of two proposed fabrication methods. The figures are shown in cross-sectional view.

4.1.1 Method 1: Replication of microneedles

The ideal of method 1 is to replica the microneedles by using a negative PDMS mould with pre-defined microneedle-like structures (i.e. microneedle shaft and tip but without hollow). The proposed process consists of five main steps which are described as follows:

Step 1: Construction of tip-formation structures (i.e. pyramidal trenches for PMNs and sloped walls for TMNs) as depicted in Fig. 4.2.

Step 2.1: Construction of SU-8 master mold with the microneedle-like holes.

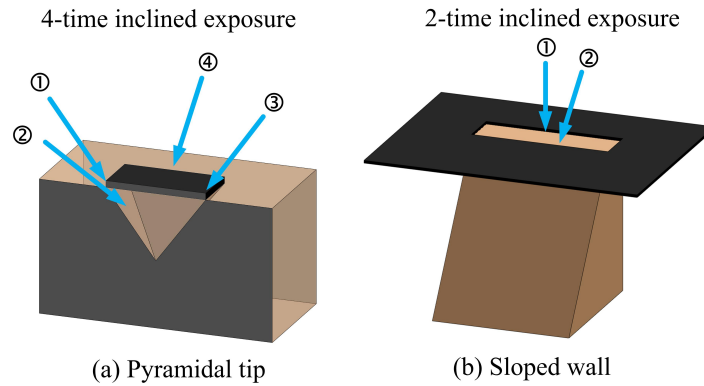


FIGURE 4.2: Construction of tip-formation structures. (a) 4-time inclined exposure and pyramidal tip, (b) 2-time inclined exposure and sloped wall.

Step 3.1: SU-8 master mold is replicated to form a negative PDMS mould by performing inverse PDMS molding two times.

Step 4.1: Molding of microneedles and formation of the microneedle hollows.

Step 5: Microneedle separation.

- *Expected outcomes:* the fabrication of microneedles using method 1 is expected to be simple, robust and cost-effective. Most importantly, method 1 may exhibit good repeatability with a reusable PDMS mold. The microneedles can be replicated robustly by using a pre-constructed mold. Since the PDMS mold is ideally designed to be reusable, only one single step of SU-8 lithography is required.

- *Expected challenges:* there are three main challenges that may associate during the fabrication of microneedle using method 1, including: (i) brokenness of structures during molding/unmolding process of the high-aspect-ratio structures. Specifically, it is not easy to perform perfect the step of structure releasing with microneedle-like structures (AS~5-6). (ii) imperfect microneedle tips due to poor PDMS encapsulation into diminutive holes. This process requires a high vacuum to be accomplished. (iii) high possibility of hollow blocking due to the effect of light scattering. In the exposure step (step 4.1 in Fig. 4.1), the effect of light scattering becomes more critical when the unexposed region is relatively smaller than the thickness of SU-8 layer. The opaque circular area is $80\mu\text{m}$ -wide and the SU-8 layer (at step 4.1) is more than $1500\mu\text{m}$ thick.

4.1.2 Method 2: Direct formation of microneedles

Method 2 was developed with the expectations to overcome the challenges remained with method 1. The key ideal of method 2 is that the microneedles are constructed and released directly from the tip-formation structures (see Fig. 4.2). The first version of method 2 was conducted on the PDMS sloped walls. The description for each step in the process flow is presented as follows:

Step 1: Construction of tip-formation structures (e.g. pyramidal trenches for PMNs and sloped walls for TMNs) as depicted in Fig. 4.2.

Step 2.2: Tip-formation structure is replicated to form negative PDMS mold by performing inverse PDMS molding two times.

Step 3.2: Formation of microneedle shaft with step 1 of double exposure technique.

Step 4.2: Formation of the support plate for microneedles array with step 2 of double exposure technique. The exposure should be conducted in a short period of time to control the thickness of support plate.

Step 5: Microneedle separation.

- *Expected outcomes:* method 2 is expected to exhibit two important improvements in comparison to method 1, including: (i) the improved quality of fabricated tips. In method 2, the same procedure of 4-time inclined exposure is applied to fabricate the pyramidal tips. But at step 2.2 in Fig. 4.1, for example, the pyramidal tips are replicated instead of the microneedle-like structures. With this difference, the tips to be replicated have relatively smaller aspect ratio ($AS \sim 1.6$) compared to $AS \sim 6$ of the microneedle-like structures. Therefore, molding/unmolding process is much easier to perform and the quality of PDMS pyramidal tips is greatly improved. (ii) formation of microneedle hollow is more feasible compared to method 1 since the effect of light scattering may be lowered.

- *Expected challenges:* there are two challenges may associate in the process of method 2, including: (i) tip-damaging in microneedle separation. The needle tips may be broken in the releasing step (after step 4 in Fig. 4.1) due to strong adhesion between cross-linked SU-8 and the substrate. In my experiments, several solutions (e.g. metal coatings, surface modification, PDMS) were attempted to lower the adhesion, thus increase the possibility to obtain sharper microneedle tips. (ii) misalignment in double exposure technique. At step 3.2 and 4.2 in Fig. 4.1, the photomasks should be aligned accurately in order to obtain well-constructed microneedles.

4.1.3 Design of aluminum holder for inclined exposure

For inclined exposure, a metallic holder is sketched in Solidworks and manufactured by using CNC precision mechanic. The design of the aluminum holder is shown in Fig. 4.3. The holder consists of two parts: top part and bottom part. The inner diameter of the top part is 76.2mm which is capable to contain a 3-inch wafer. The bottom part provides an angle of 18° for inclined exposure. The top and bottom parts are fitted together by rotation joints (one on the backside of the top part and four on the front side bottom part). Fig. 4.3a shows the cross section of a assembly of two parts which are fitted together by rotation joints. To increase the holder stability during exposure, four markers (see Fig. 4.3a) in the bottom side

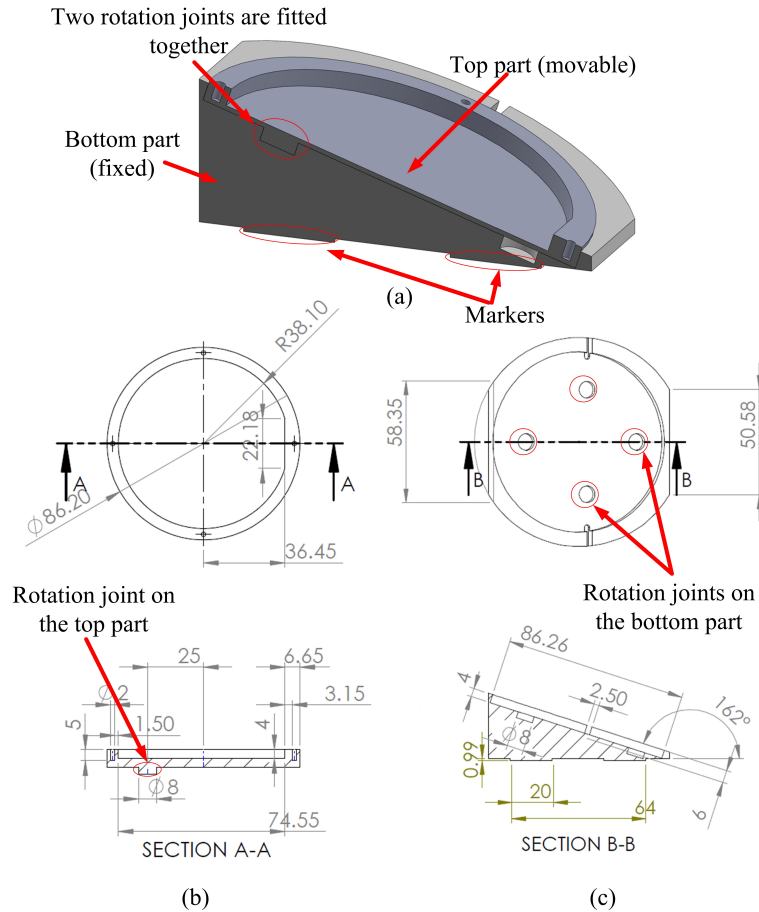


FIGURE 4.3: Design and working principle of the aluminum holder. (a) cross section of the aluminum holder, (b) schematic design of the top part, (c) schematic design of the bottom part.

of the aluminum holder are designed to fit into four trenches on the wafer holder of aligner machine. Fig. 4.3b, c show a 2D schematic drawing which present the detail dimensions of the top part and bottom part, respectively.

Pyramidal tips with 4-time inclined exposure: the principle of 4-time exposure process to form pyramidal tip is illustrated in Fig. 4.4. The top part (movable part) is rotated relatively to the bottom part (fixed part). Rotation is precisely controlled by four joints on the bottom part and one joint on the backside of the top part. The sample is exposed four times (Fig. 4.4a) in total to obtain a complete pyramidal tip. The exposure angle can be increased from 18° (Fig. 4.4b) to 35° by using an additional part with a 17° increased angle (Fig. 4.4c). The illustration for pyramidal tip is shown in Fig. 4.2a.

Sloped walls with 2-time inclined exposure: to fabricate the sloped walls for making the bevel tips of TMNs, two-time inclined exposure process is utilized with relative rotation of the top part to the bottom part. The first exposure is conducted when the top part at position 1 in Fig. 4.4a. The sample is then exposed with the second exposure in the direction

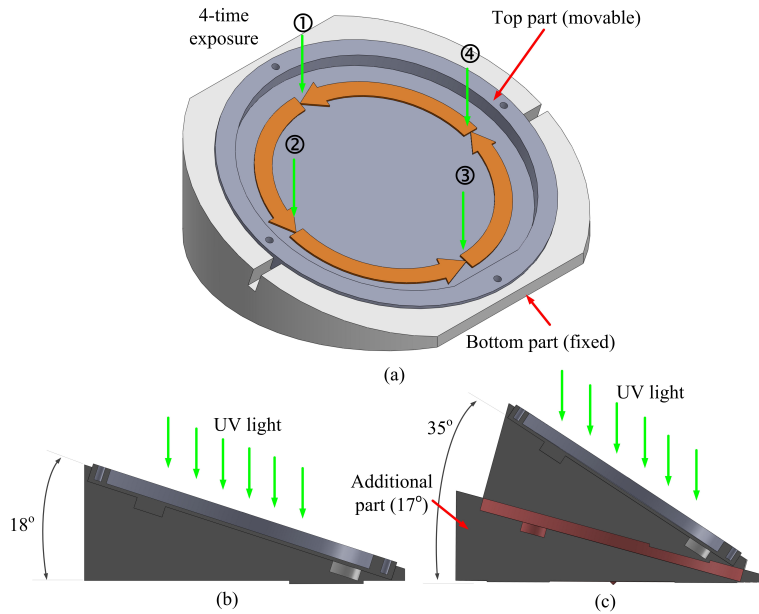


FIGURE 4.4: Working principle of inclined exposure to fabricate pyramidal tips with an aluminum holder. (a) illustration for 4-time exposure with the holder, (b) schematic design of the bottom part, (c) schematic design of the top part. The bottom part is fixed during implementation process while the top part is rotated 4 times by 90° each time. At each position, the sample is exposed once to create one side of the pyramidal tip.

perpendicular to the sample substrate. The illustration for pyramidal tip is shown in Fig. 4.2b.

4.2 Fabrication issues and solutions

According to the recommended process in datasheet, MicroChem proposes a typical lithography process for SU-8 2150 with the thickness up to $550\mu\text{m}$. With thick SU-8 layer, the photolithography becomes more complicated and not easy to be well-controlled. Typically, it is very challenging to obtain high-aspect-ratio structures without any modifications from the standard process. To achieve quality fabricated microneedles, each process parameter should be carefully controlled and optimized. Several challenges that need to be addressed, including: wafer bending due to thermal stress, UV light absorption, air gap problem in inclined exposure. In addition, aluminum substrate was utilized as an alternative for silicon wafer. With higher strength, aluminum plate showed to be beneficial in reducing bending problem and wafer brokenness. The fabrication process were optimized for aluminum plate with various settings of lithography parameters.

4.2.1 Bending problem and the proposed solution "separated lines"

During the photolithography process, fabrication of microneedle has experienced several problems of cracks, poor adhesion or wafer bending, due to the compressive thermal stress. It is experimentally observed that the explanation would be the problem of wafer bending. In fact, It is the most critical issue needs to be addresses, otherwise the structures may be lifted off or destroyed. Physically, the origin of this stress is the large mismatch in CTE between SU-8 and the substrate. After exposure and PEB, the exposed SU-8 becomes harder but more brittle which subsequently results in an increase of thermal stress subjected at the SU-8-substrate interface. The consequences of thermal stress in SU-8 film was reported in [53, 60, 61].

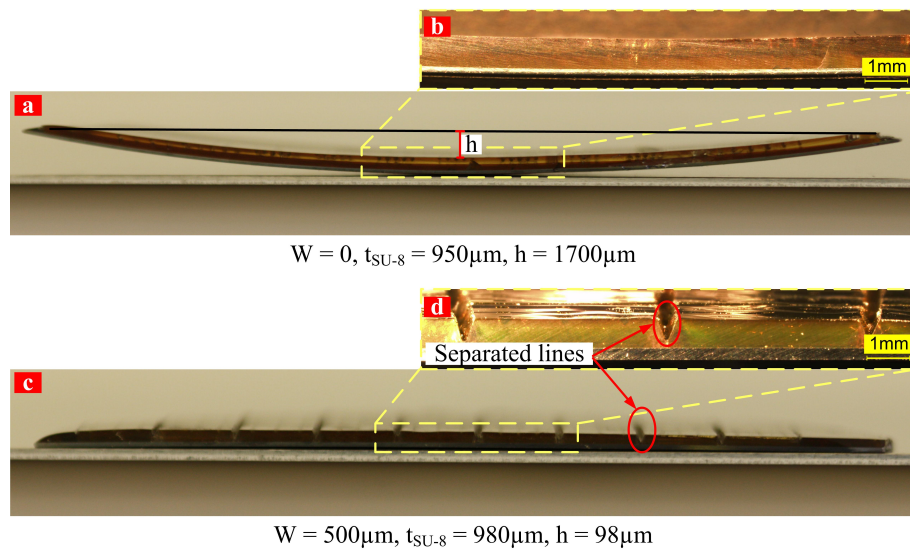


FIGURE 4.5: Optical photographs illustrate the advantage of the separated lines in thermal stress reduction. (a), (b) 950 μm -thick SU-8 layer, no separated lines, deformation height $h = 1700\mu\text{m}$. (c), (d) 980 μm -thick SU-8 layer, 500 μm -wide separated lines, deformation height $h = 98\mu\text{m}$.

In this thesis, one solution called "separated lines" was proposed to solve this problem. The ideal of this concept is to reduce the stress applying area, thus providing more space for SU-8 to expand/compress upon heating/cooling. In comparison to the solution of ultrasonic treatment proposed by Du et al. [61], separated line is potentially simpler and easier for implementation. In addition, the proposed solution is especially suitable for multilayer process to produce ultrahigh-aspect-ratio SU-8 structures. Separated lines are patterned on a photomask to separate and reduce the stress applying area (see Fig. 4.5c, d), thus providing more space for SU-8 to expand/compress upon heating/cooling. The optimal width of separated line (W) was chosen to be 500 μm based on the numerical and experimental studies. The tests on 3-inch silicon wafer were conducted to examine the advantage of separated line. The wafer bending reduced significantly from 1700 μm to 98 μm for the cases of $W = 0$ and $W = 500\mu\text{m}$ as illustrated in Fig. 4.5a and see Fig. 4.5c, respectively.

4.2.2 Air gap problem and glycerol compensation

The core ideal of microneedle fabrication in this thesis is inclined exposure [62–64]. It is applied to obtain pyramid-shaped trenches and sloped-wall. Because of a large mismatch in refractive index of SU-8 ($n = 1.668$ at 365nm wavelength [65]) air ($n = 1$), the incident angle (i.e. exposure angle) is limited at 36° [64]. The tilted angle of the substrate cannot exceed 45° due to the height limitation between wafer holder and UV lamp. Thus, the maximum incident angle is actually smaller (approximately 25°).

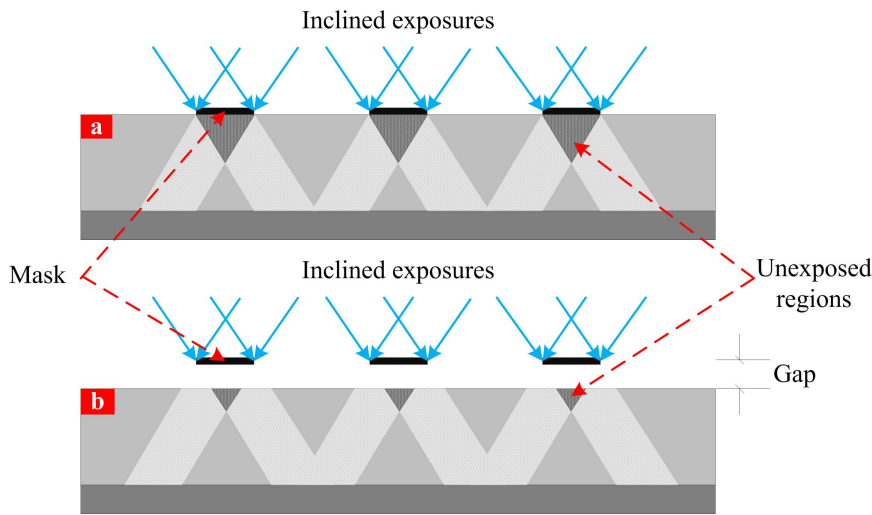


FIGURE 4.6: The effect of gap between mask and substrate on the pyramid-shaped trenches. (a) without gap, (b) with gap. In general, the gap is resulted from low uniformity of SU-8 surface or un-leveled hot plate.

Practically, the tilted Aluminum holder is design to have maximum angle of 33° . It means the incident angle is reduced to approximately 19° with air gap between mask and substrate. To have higher incident angle in SU-8 layer, compensation with high refractive index material is desirable. In my experiments, glycerol ($n = 1.47$) was filled in the gap between SU-8 and mask, thus increasing the incident angle up to 25° . Some researchers suggested to use water ($n = 1.33$) [66, 67], however, it is experimentally shown that filling the gap with water often causes wrinkles on SU-8 surface after exposure step. A higher viscous liquid may be reasonable in this case. One commonly-used option is glycerol which has been chosen in numbers of studies [34, 64, 68]. In addition, glycerol compensation also helps to reduce the effects of light diffraction [69].

In fact, between the photomask and top surface of SU-8 always has a gap due to rough SU-8 surface, un-leveled baking or bad uniformity. With standard exposure in vertical direction, this problem has no effect on the structures. However, in this case, when performing inclined exposure, this problem becomes particularly critical. Specifically, in the fabrication of pyramidal tips, since the size of opaque regions on photomask vary from $300\mu\text{m}$ to $400\mu\text{m}$. If the gap between mask and substrate is relative too high compared to the width of opening area,

the exposed regions will be changed and reduced in size of developed structures. In addition, with gap filling with glycerol, hard contact between the photomask and the sample during exposure can be provided. Illustration for this is presented below in Fig. 4.6.

4.2.3 Aluminum substrate - an alternative for silicon wafer

As an alternative for silicon wafer, aluminum substrate is utilized because of its advantages in mechanical strength, adhesion and thermal transfer. Some specific properties of aluminum plate, silicon wafer and SU-8 are presented in Table 4.1. Practically, thermal stress is created after curing of SU-8, especially after PEB and hard baking process. The problem of internal stress is presented in subsection 4.2.1. Stress is originally resulted from the mismatch in coefficient of thermal expansion (CTE) between SU-8 and silicon wafer. Large internal stress caused many problems in fabrication of thick SU-8 layers, especially for multilayer structures. For example: bending of wafer (i.e. wafer curvature), misalignment, poor adhesion and cracks.

TABLE 4.1: Comparison between properties of Aluminum substrate and Silicon wafer.

Properties	Al substrate	Silicon wafer	SU-8 2150
Thickness (μm)	1000	350	
Young's Modulus (GPa)	69 [70]	130.2 - 187.5 [71]	4.02 [71]
CTE (ppm/K)	23.1 [72]	3 [?]	52 [73]
Thermal conductivity (W/mK)	205 [74]	131 [75]	

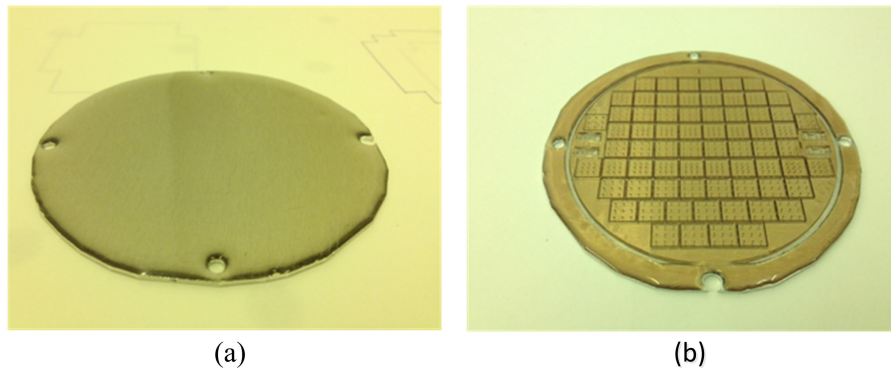


FIGURE 4.7: Illustrations for the use of aluminum substrate in fabrication of pyramidal tips. (a) Coated SU-8 2150 layer, (b) Pyramid tips on Al substrate after development of SU-8. To minimize the effect of internal stress, separated lines were also utilized.

Based on the given data in Table 4.1 and experimental results, the replacement of Al substrate for silicon wafer contributes to:

Wafer bending problem

With aluminum substrate, the sample is no longer bent even with ultrathick SU-8 coating. This improvement comes from much better mechanical strength of aluminum substrate compared to silicon wafer which is extremely brittle and easily broken.

Heat transport: longer cooling time

With high thermal conductivity (205 W/mK), aluminum theoretically allows faster heat transfer. Moreover, thanks to thicker substrate, typically it takes longer time to be heated up to 110°C, allowing more uniform baking and less wrinkles on SU-8 surface. Heating rate of aluminum substrate is 13°C/min compared to 40°C/min with silicon wafer. The measured cooling rate was assumed to be linear.

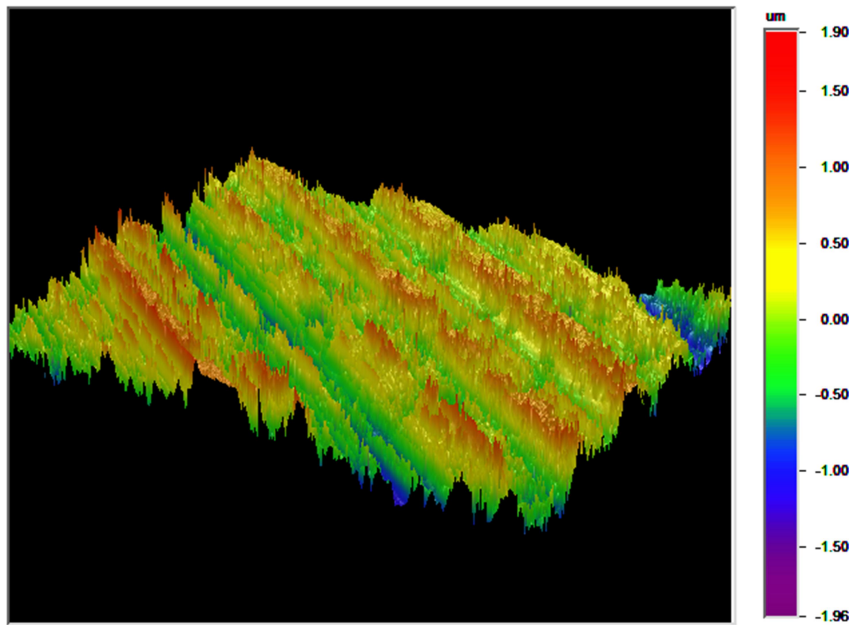


FIGURE 4.8: A topography 3D image of aluminum substrate built by Interferometer Wyko NT9100 at 20x magnification. The average roughness $R_a=384.6\text{nm}$. Roughness variation is shown on the legend to be from $-1.96\mu\text{m}$ to $1.9\mu\text{m}$. There are lots of directional scratches which may help to improve the adhesion between SU-8 and the substrate.

Strong adhesion with cured SU-8

In general, SU-8 has good adhesion with aluminum as stated by Williams et al. in [31]. Moreover, the aluminum substrate that has been used in my experiments has relative high roughness with scratches during the manufacturing process. The average surface roughness (R_a) of aluminum substrate is measured to be 384.6nm by Interferometer Wyko NT9100. Surface roughness of aluminum substrate is studied by scanning on a 3cm-square area. A 3D topography image, which is built based on the obtained data, is shown in Fig. 4.8.

Using Al substrate allows bubble destruction

Aluminum substrate also has slower cooling rate is approximately 13°C/min. It also helped to solve the problem of bubbles in pyramid-shaped trenches in the first step of SU-8 coating. Specifically, with the diminutive pyramidal tips on silicon wafer, it is very challenging to get rid off all the bubbles in the pyramidal trenches. Specifically, the silicon wafer cools rapidly, the coated SU-8 thus becomes more viscous, the bubbles are then very difficult to be sucked up in the vacuum chamber. On the other hand, with aluminum substrate, the necessary

time for cooling the sample to room temperature is relative longer, therefore, bubbles can be easily sucked up to the top surface. Most of these bubbles will be disappeared during baking step, the remaining bubbles can be destroyed manually by using a metallic needle. Aluminum plate was also used as a substrate for mounting the negative PDMS mould. To fix the PDMS mould, avoid bending problem during baking step and allowing longer cooling time for better efficiency in bubble destruction.

4.3 Optimization of lithography process for ultrathick SU-8 layer

This part presents the development of lithography process particularly for thick SU-8 layer. One lithography process consists of seven main steps. The process parameters in each step were experimentally studied and optimized. The optimal parameters optimized for specific structures, for example: pyramidal tips, sloped walls, microneedle shafts and microneedle hollows, are summarized in the end of this subsection.

Step 1. Substrate preparation

For better adhesion with SU-8, substrates are treated with acetone, IPA and DI water before being dry with Nitrogen gun. Dehydration was then performed on the hot plate at 120°C for 5 minutes. Before coating of photoresist, the substrates were primed by Oxygen plasma cleaner in 3 minutes. After this step, substrate was sufficiently cleaned for further steps.

Step 2. Coating of SU-8: Weight-controlled method

As discussed before in chapter 2, there are several techniques for coating of SU-8, including: multiple coatings, volume-control coating or constant-volume-injection [76]. In this thesis, coating of SU-8 is performed by pouring heated SU-8 onto the substrate by a weight-control approach. More specific, SU-8 was firstly weighted and subsequently poured on the petridish. Then it was warmed to 60°C for 5 minutes to reduce viscosity and avoid bubbles. This temperature is above glass transition temperature of SU-8 ($T_g = 50-55^\circ\text{C}$ [77, 78]) at which SU-8 become softer and less viscous. Pre-heating allows SU-8 to flow easily without creating bubbles. With the density $\rho = 1.19\text{kg/m}^3$, 5.25g of SU-8 2150 is required to get 1mm thick on 3-inch wafer, but practically it was rounded to be 6g. Wafer can be swiveled letting SU-8 flows across the wafer, reducing the possibility of bubbles formation at the interface between SU-8 and the substrate.

In addition, with the second SU-8 layer, during baking period, SU-8 can easily flow out of wafer due to not perfect leveling of hot plate. This situation frequently leads to uniformity and thinner SU-8 layer. To avoid this problem, a ring of cured SU-8, namely coating barrier (see Fig. 4.9b), is formed over the edge of substrate, making the barrier to avoid flowing out

of the heated SU-8. Moreover, SU-8 is very sensitive to the planarization of the hot plate, therefore, hot plate should be carefully leveled prior to the next step.

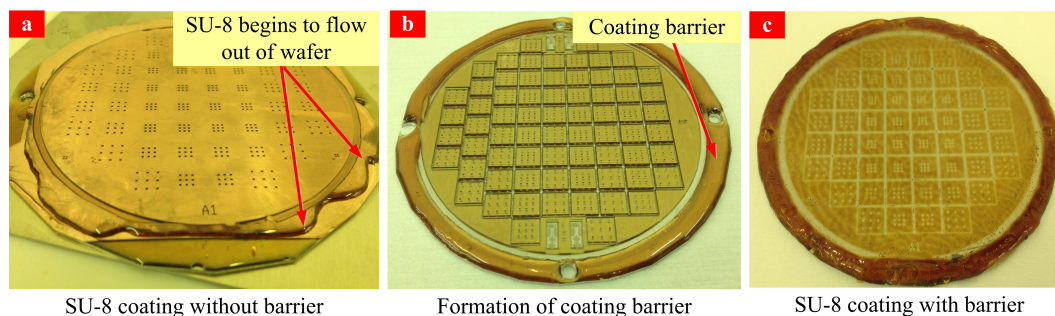


FIGURE 4.9: Illustration of SU-8 based barrier for coating of thick SU-8 layer: (a) coating of second SU-8 layer without coating barrier, (b) coating of second SU-8 layer with coating barrier (c) 1400 μm -thick second SU-8 layer after soft bake. The coating barrier is created by forming a 1000 μm -thick SU-8 ring around the substrate, the barrier is baked at 110 $^{\circ}\text{C}$ for 15 minutes before being exposed for 80 seconds and developed in 5 minutes with ultrasonic agitation. The inner part of substrate was covered by a 3-inch wafer to avoid over-exposed effect on the inner desired structures.

Step 3. Soft bake

According to the manufacturing datasheet of SU-8 2150, soft baking process contains of two steps at two different temperatures: 65 $^{\circ}\text{C}$ and 95 $^{\circ}\text{C}$. Baking time depends on the thickness of photoresist. Moreover, as mentioned before, microneedles have to be fabricated in millimeter-range in order to reach blood vessel for blood collection approach. Therefore, time for soft baking is supposed to be longer to reduce the retained solvent level. However, it is stated that baking time can be reduced with higher baking temperature i.e. 100-120 $^{\circ}\text{C}$ [76]. The chosen temperature for baking was 110 $^{\circ}\text{C}$ on Aluminum foil and the actual temperature on the sample is approximately 100 $^{\circ}\text{C}$. In addition, for the second SU-8 layer coated on a sample with predefined pyramidal tips, the baking time should be carefully controlled and optimized for optimal solvent evaporation. Hot plate was utilized because it provides more uniform solvent evaporation, especially for SU-8 near the interface with the substrate.

Step 4. Exposure with UV light

For optimization of exposure time, a 1100 μm thick SU-8 layer was coated on a 4-inch Si wafer. The exposure dosage varied from 1000 mJ/cm^2 to 3500 mJ/cm^2 , other parameters were kept the same. The results are shown in Fig. 4.10. With thick SU-8 layer, multiple exposures are required to avoid overheating, scattering, and diffusion on the surface of the resist [34]. Typically, exposures need to be separated in 20-second (or less than 400 mJ/cm^2 per time) intervals with 60-second waiting periods in between. As can be seen from Fig. 4.10, when the exposure dosage was smaller than 3000 mJ/cm^2 , the pillar were deformed, bent and broken. Whereas, the quality of pillar were not changed so much when increased the exposure dosage from 3000 to 3500 mJ/cm^2 . In conclude, to form the microneedle shafts, the exposure dosage of 3000 mJ/cm^2 was utilized.

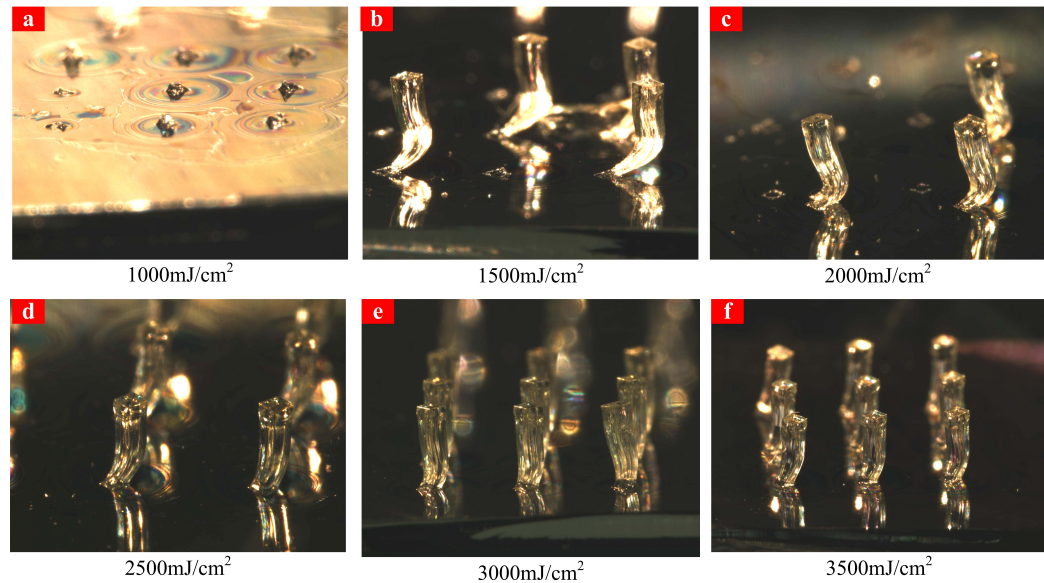


FIGURE 4.10: Optical illustrations for the optimization of exposure dosage. During development with ultrasonic agitation, the pillars were deformed due to soft, underexposed support at bottom part. The exposure dosage of $3000\text{mJ}/\text{cm}^2$ was chosen to be optimal exposure dosage.

Step 5. Post bake (PEB)

In my experiments, PEB needs to be considered and carefully controlled for the reasons of minimization of thermal stress and development ability. In fact, post-exposure baking time depends on different structures, particularly for pyramidal holes and out-of-plane pillars. More specific, in fabrication of pyramidal tips and microneedle-shaped holes, post-exposure time was approximately 30 seconds to 1 minute. The unexposed regions are expected to be completely uncrosslinked, however, the SU-8 regions in the holes are partially cured due to the effects of UV light diffraction and scattering. Therefore, long PEB step will accelerate the thermal curing, thus leading to the difficulty in development and unwanted SU-8 residual. On the other hand, in the formation of out-of-plane structures such as the sloped wall or direct-forming microneedles, the sample should be post-baked sufficiently long for better structural stability. Fig. 4.11 illustrates the effect of long post-baking time on the pyramidal tips. It can be observed that when the post-baking time increases, the unexposed SU-8 becomes more difficult to be developed. The results showed that the optimal PEB time should be from 30 seconds to 1 minute in order to obtain good pyramidal tips. The development time should also be controlled precisely to avoid damaging the tips.

Step 6. Development

In the photolithography process of thick SU-8, there are numbers of challenges associated during the development step due to agitation problem. In general, without agitation, the development may last hours but normally is still critical to achieve high aspect ratio structures. Long development also softens the bottom part, damages the fine structures and normally the structures are not completely developed. Therefore, strong agitation is required and in

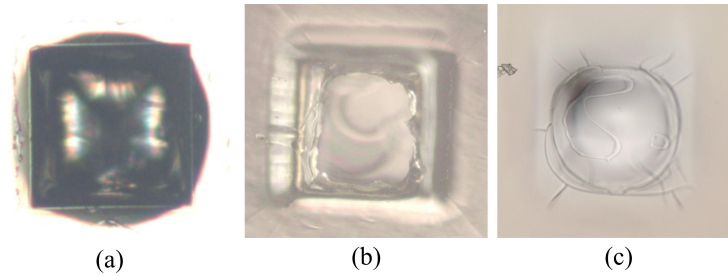


FIGURE 4.11: Optimization of PEB time for the fabrication of pyramidal tips. (a) 1 minute at 95° , (b) 5 minute at 95° , (c) 10 minute at 95° . The exposure dosage for each sample was the same, $4 \times 700 \text{ mJ/cm}^2$. The samples were continuously checked during development. For 1 minute baking, development was fully finished and sharp tips can be created. Whereas, with 5 minutes and 10 minutes baking, it is very difficult to develop even with long development time.

my experimental works, ultrasonic energy is utilized (Ultrasonic Cleaning Brandson). The advantages of ultrasonic energy is obvious that strong stirring is provided, allowing much faster development. However, it may cause microstructures destruction, sidewall quality or debonding of fine patterns if waves propagate laterally to the substrate. Therefore, it is required that the sample is placed perpendicularly to the direction of wave propagation in order to minimize the possibility of structure damage. Experimentally, during development process, the structures are continuously checked when using ultrasonic agitation to avoid over-development. At the point of pre-finishing, the samples were positioned in a face-down orientation to take the advantage of gravity force. Better transportation of dissolved SU-8 is provided, therefore, better profile at the bottom part can be achieved.

Step 7. Flood-exposure and hard bake

To harden the structures after development, flood exposure was performed with exposure dosage of 400 mW/cm^2 followed by 2-minute hard baking at 130°C . For the final microneedle structure, longer hard baking is required and the convection oven is preferable.

Summary of optimal SU-8 lithography parameters

In conclude, the parameters for lithography process with SU-8 are summarized and presented in Table 4.2.

TABLE 4.2: Summary of lithography process for thick SU-8 layer

Thickness (μm)	Coating	Softbake		Exposure (mJ/cm^2)		Postbake		Dep. time (min)	Flood exp. (mJ/cm^2)	Hardbake 130°C
		65°C (min)	95°C (hrs)	65°C (min)	95°C (min)	65°C (min)	95°C (min)			
Pyramidal tips	3.25g	15	5	700x4	5	30	10	2000	2min	
600	3.25g	15	5	1800	5	30	10	2000	2min	
1200	6.5g	30	12	3000	5	60	15	2000	2min	

Inverse PDMS molding

For a 3-inch wafer, to obtain 2mm - 3mm thick PDMS mould, about 25g - 30g of PDMS mixture is required. The amount of each chemical was precisely controlled by weighting. One process of inverse PDMS molding consists of three following steps: (i) Silicon elastomer (PDMS) was carefully weighted and mixed with curing agent in the proportion of 10:1. The mixture was then whisked vigorously with a spatula for about 10 minutes to ensure that the curing agent is uniformly distributed. The homogeneous mixture was then put inside a vacuum chamber in 1 hour for degassing. (ii) In the meanwhile, a thin anti-sticking chemical (Silane) was performed on the SU-8 substrate by evaporation process in a vacuum chamber for 1 hour. The sample must be sufficiently treated before casting of PDMS, otherwise it may induce difficulty in the unmolding step. (iii) The PDMS mixture was casted on the treated sample. After casting of PDMS, degassing was performed with a strong vacuum pump which can reach down to less than 1mbar. The sample was then stored in convection oven at 60°C overnight to activate curing process.

4.4 Fabrication of pyramid-shaped microneedles (PMNs)

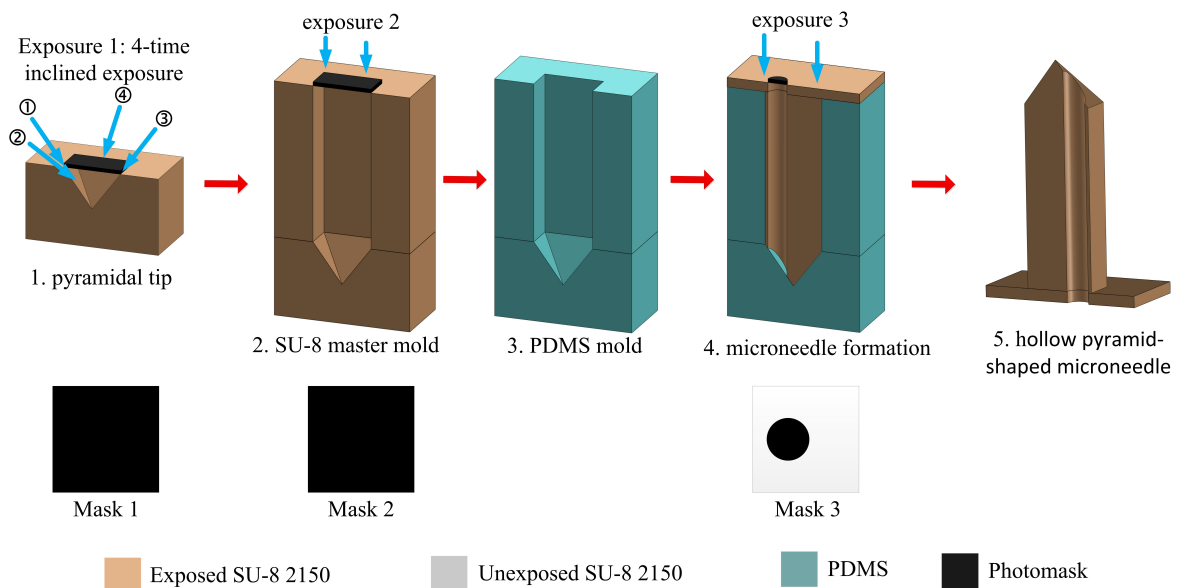


FIGURE 4.12: Process flow for fabrication of PMNs by using method 1.

The process to fabricate PMNs with method 1 consists of five steps, as shown in Fig. 4.12. The first step in Fig. 4.12 is to fabricate the pyramidal tips by using 4-time inclined exposure method. Firstly, 3.3g SU-8 2150 was coated on the substrate and softbaked for 15 minutes at 65°C and 4 hours at 110°C. The exposure dosage for each time was 700mJ/cm². Post-baking time was about 1 minute on a 110°C hot plate. The sample was then immersed

into the developer mr-Dev 60. Fully developed pyramidal tips was achieved after 10-minute developing with ultrasonic agitation. 500 μm -tall pyramidal tips can be observed in Fig. 4.13.

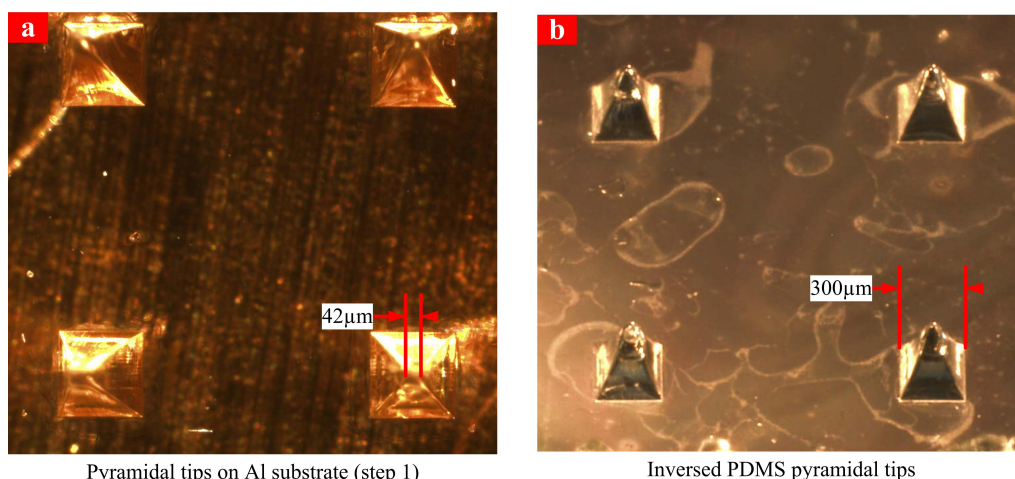


FIGURE 4.13: Step-by step results of PMNs fabrication. (a) Pyramidal tips on Al substrate, (b) Inverse PDMS pyramidal tips.

The second step is formation of microneedle shaft to obtain microneedle-like holes. A 1200 μm -thick photoresist layer was coated by pouring 6g SU-8 2150. Soft-baking was performed on hot plate at 65 $^{\circ}\text{C}$ for 30 minutes and at 110 $^{\circ}\text{C}$ for 12 hours. The sample was then exposed with the exposure dosage of 3000 mJ/cm^2 followed by post-baking at 65 $^{\circ}\text{C}$ for 5 minutes and at 110 $^{\circ}\text{C}$ for 1 hour. Development time was 15 minutes. An additional flood exposure (2000 mJ/cm^2) and hard-baking (2 minutes at 130 $^{\circ}\text{C}$) is desirable for completely curing of SU-8. After step 2 in Fig. 4.12, the microneedle-like holes were constructed and presented in Fig. 4.14a.

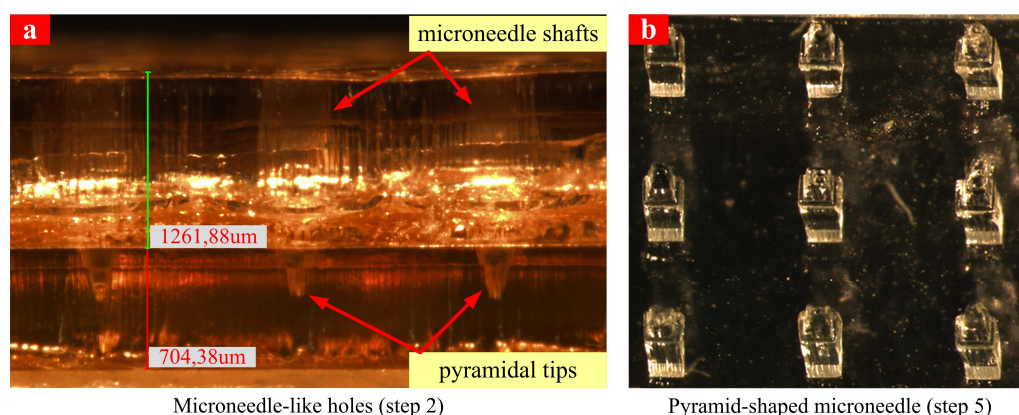


FIGURE 4.14: Step-by step results of PMNs fabrication. (a) Microneedle-like holes, (b) PMNs.

At step 3 in Fig. 4.12, the constructed microneedle-like holes were then utilized as the master mold for performing inverse PDMS molding. The fourth step focused on microneedle molding through a negative PDMS mold. The SU-8 2150 was cast by weight ($\sim 3\text{g}$) on the PDMS mold to obtain 300 μm -thick support plate. Soft-baking time was 15 minutes at 65 $^{\circ}\text{C}$ and 5 hours at 110 $^{\circ}\text{C}$. The microneedle hollows were created with 3500 mJ/cm^2 . After 20-minute

development, the microneedles arrays were separated from the substrate manually by using metallic tweezers.

The step-by-step fabrication results are illustrated in Fig. 4.14- Fig. 4.15. Fig. 4.14a shows the optical micrographs of pyramidal tips. The lateral dimension was measured to be approximately $300\mu\text{m}$ with tip-size of $42\mu\text{m}$. The process with method 1 was experimentally studied. The manufacturability of this method were also considered with the following criteria: quality of the fabricated microneedle, repeatability and throughput. There were four main limitations with method 1 are presented as follows:

(i) *Tip damaging and brokenness during molding/unmolding*: in method 1, inverse PDMS molding was performed two times to create negative PDMS mould with microneedle-like holes. Gentle separation is highly desirable when performing the high-aspect-ratio structures i.e. microneedle-like holes, however, brokenness was occurred and lowered the repeatability and throughput.

(ii) *Problem at the interface between the first and second SU-8 layer*: at step 2 in Fig. 4.14, the quality of vertical walls (i.e. microneedle shafts) did not provide good repeatability since the cavity created at the interface between the first and second layer was not perfect. Moreover, development step must be carefully controlled to achieve straight shaft.

(iii) *Difficulty in the formation of microneedle hollows*: it was experimentally shown that it is very challenging to form high-aspect-ratio microneedle hollows. The circular opaque features patterned on photomask is much smaller compared to the opening area. The effect of light scattering thus becomes more critical.

(iv) *Misalignment*: distance between alignment marks on mask and on substrate $\sim 1\text{mm}$, therefore they cannot be optically focused at the same time under microscope, thus inducing alignment error.

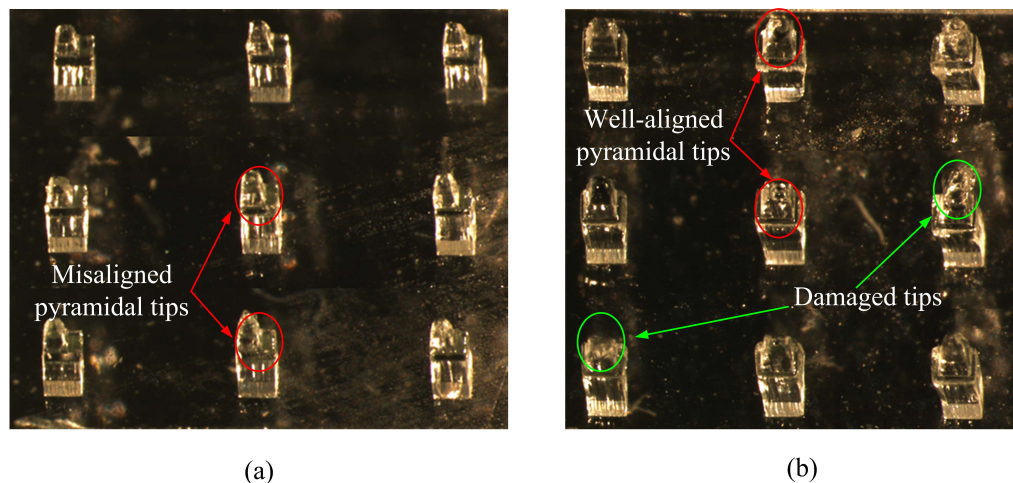


FIGURE 4.15: Step-by step results of PMNs fabrication. (a) misaligned PMNs, (b) well-aligned PMNs.

4.5 Fabrication of traditional-shaped microneedles (TMNs)

This section presents fabrication of TMNs on pre-constructed sloped walls by using method 2. Method 2 was firstly introduced to overcome the problem during molding process with lower aspect ratio structures i.e. pyramidal tips and sloped walls. The molding/unmolding process with sloped walls is hoped to be more feasible. In addition, the microneedle shafts are directly formed by a single-step lithography process. The effect of light scattering is reduced due to small opening area on the photomask as compared to opaque regions (see mask 2 in Fig. 4.16). The fabrication process was developed through two main experiments conducted on PDMS sloped walls and SU-8 sloped walls. The fabrication process was further improved with the utilization of CASW. The process development will be presented step-by-step through three experiments as follows:

4.5.1 Fabrication of TMNs on PDMS sloped walls

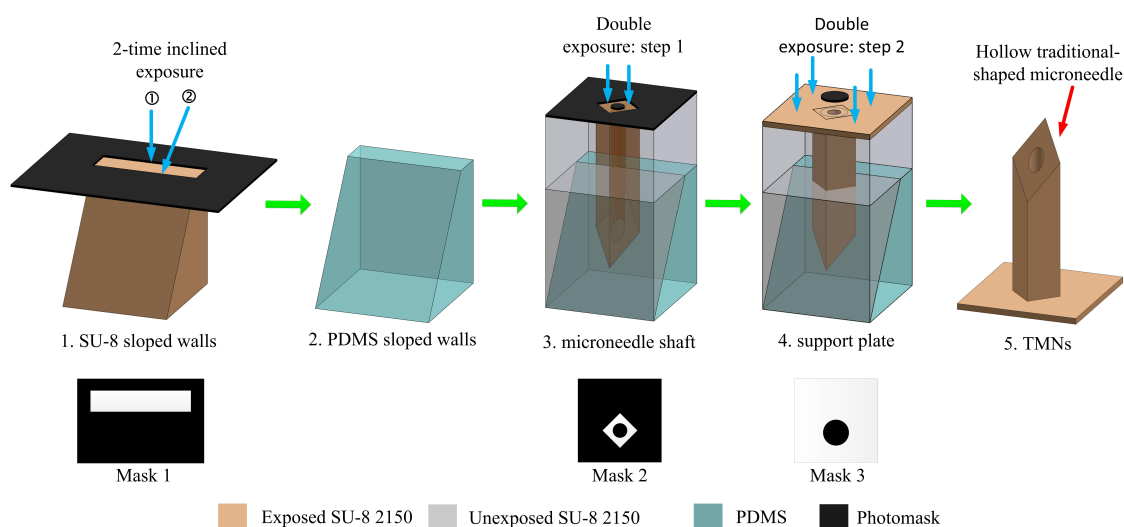


FIGURE 4.16: Process flow for fabrication of TMNS on PDMS sloped walls. Step 1: SU-8 sloped wall; Step 2: PDMS sloped wall; Double exposure: step 3: formation of microneedle shaft, step 4: formation of support plate; Step 5: desired TMNs.

Fabrication of TMNs begins with the formation sloped walls followed by the direct formation of microneedles and microneedle separation. The arrays were gently blown dry using a nitrogen gun prior to flood exposure and hard bake. At step 1 in Fig. 4.16, the SU-8 sloped walls were lithographically defined by 2-time inclined exposure with mask 1. To form the sloped walls, the preheated SU-8 was cast manually by weight onto on aluminum substrate to obtain a thickness of $1050\mu\text{m}$. The sample was softbaked for 30 minutes at 65°C and 12 hours at 110°C . The sample was exposed two times with the exposure dosage of $3000\text{mJ}/\text{cm}^2$ for each to form the vertical and sloped side. Postbaking step was 5 minutes at 65°C and 1 hour at 110°C . Full development was achieved after 15 minutes developing with ultrasonic agitation.

After the sloped walls were constructed, inverse replica molding of PDMS was performed two times to obtain the negative PDMS mould of sloped walls (see step 2 Fig. 4.16).

Step 3 and 4 illustrate the double exposure method to form the microneedle shaft and the support plate by using mask 2 and mask 3, respectively. 9g SU-8 2150 was coated on the substrate, the sample was then softbaked for 15 hours at 110°C. Double exposure includes two steps of exposure, including: step 1: 3000mJ/cm² and step 2: 300mJ/cm². Mask alignment is an important step in double exposure technique, especially at step 4 in Fig. 4.16. Specifically, when performing the shallow exposure to form the support plate, alignment error may lead to the blocking of microneedle hollow. For easier alignment, a solution called *double PEB step* was introduced by Wang et al. [79]. An additional PEB step was conducted at 110°C for 5 minutes after performing step 3 in Fig. 4.16, thus making the exposed regions become optically clearer under the built-in microscopes of the aligner machine. However, in my experiments, the microneedle shafts were relocated upon heating. The reason for this would be the exposed regions are much smaller compared to the unexposed regions. And the unexposed SU-8 regions will become liquid at PEB temperature which is normally over the glass transition temperature of SU-8 (50-60°C). Subsequently, the exposed structures will flow randomly due to the flowing of liquid SU-8. And obviously, the desired microneedles with support plate cannot be created.

At step 5 in Fig. 4.16, the microneedles were separated from the substrate during development or by using tweezers. In this step, one crucial problem is the brokenness of microneedle tips due to strong adhesion between microneedles and the substrate. With PDMS sloped wall, separation of microneedles was easily performed since cross-linked SU-8 and PDMS has very low adhesion. Therefore, quality tip profile is achievable with the process on PDMS sloped walls. Fabrication results are presented in Fig. 4.17. TMNs were fabricated with the total length of 1515µm ((627µm tip and 888µm shaft), 300µm base square and the hollow diameter of 148µm. Tip dimension was measured to be approximately 39µm as shown in Fig. 4.17b. The hollow-structure can be observed and demonstrated from the top-view image as shown in Fig. 4.17c. It indicates that the obtained microneedles may have the ability to transport fluids with center-positioned hollow structure.

Considering the results in wafer scale, more than 30 arrays in the total of 54 arrays were misaligned or damaged after separation. The possible explanations are addressed through the discussions on remaining limitations of the process on PDMS sloped walls. Although the sharp bevel tips were able to be constructed, there are several limitations with the process on PDMS sloped walls, for example: bad surface profile (e.g. non-uniform, wrinkles) and alignment error due to thermal expansion of PDMS mould and small sloped angle.

(i) *Bad SU-8 surface profile:* PDMS is a rubber elastic polymer with high chemical and thermal resistance. However, upon heating/cooling the PDMS mould was greatly deformed.

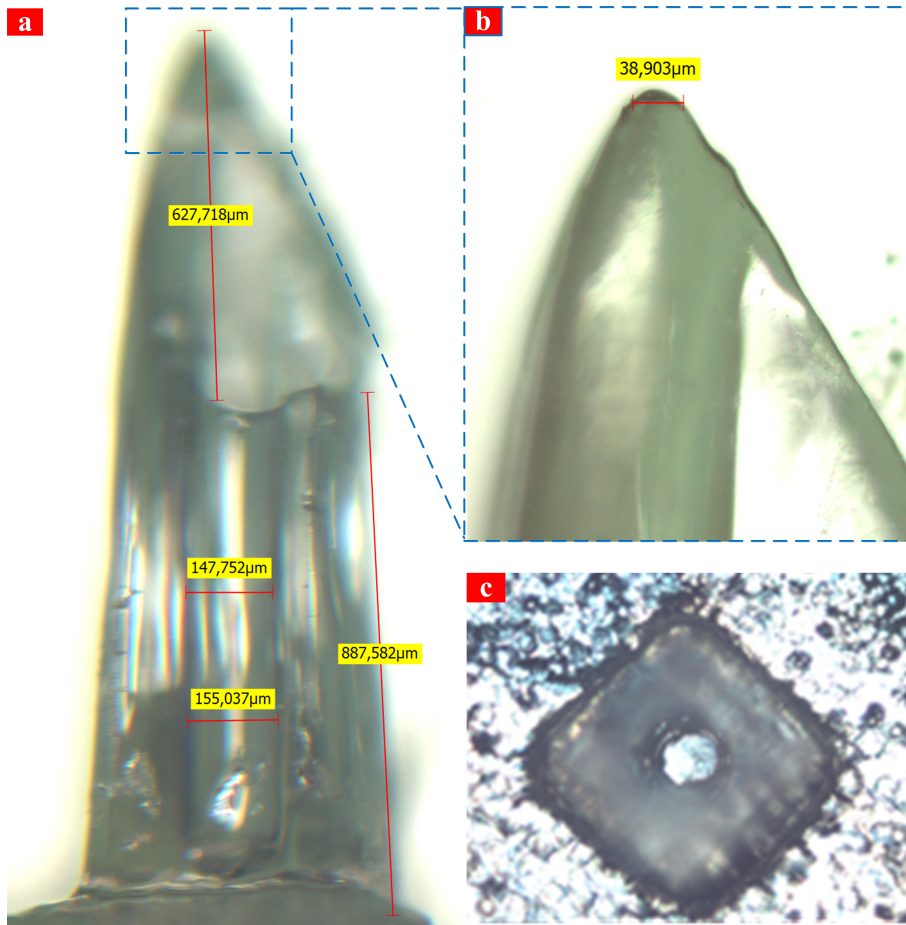


FIGURE 4.17: Optical micrographs of fabricated TMNs. (a) side view, (b) magnified image of the microneedle tip, (c) top-view. A top-view image is focused at bottom of the support plate. These figures were captured by Leica at 10x magnification.

Flat, uniform coating surface is therefore cannot be obtained. There are two possible solutions that may help to improve this problem. By applying slow cooling rate or mounting the substrate on a hard, rigid surface to reduce the thermal deformation. In my experiments, an aluminum substrate was utilized. However, the problem of wrinkles still remained.

(ii) *Misalignment due to PDMS thermal expansion*: upon heating at 110°C, PDMS will expand due to high thermal expansion. This induces a significant error on aligned structures. To fully solve this problem, the patterned on photomask should be compensated based on the total displacement of PDMS mould due to thermal expansion. The misaligned error can be calculated based on (4.1).

$$\Delta L = \alpha_L \Delta T L_0. \quad (4.1)$$

Where ΔL is total displacement (i.e. alignment error), α_L is the coefficient of thermal expansion of PDMS ($\alpha_L = 3.1 \times 10^{-4} \text{ (}^\circ\text{C}^{-1}\text{)}$). L is the original length, $L = 30\text{mm}$ (0.03m) is the distance of rightmost microneedle from the center. ΔT is temperature difference. In this case $\Delta T = 110^\circ\text{C} - 22^\circ\text{C} = 73^\circ\text{C}$. The maximum calculated alignment error $\Delta L = 0.6789\text{mm}$. Based on this number, the masks can be designed to overcome the misalignment problem.

(iii) *Misalignment due to distance (d) and sloped wall geometry*: at step 3 in Fig. 4.16, coating of a $1000\mu\text{m}$ -thick SU-8 layer induces a distance ($d = 1000\mu\text{m}$) between alignment marks on substrate and on photomask. Perfect mask alignment is thus very challenging to perform. Specifically, the alignment marks cannot be observed at the same time under the microscope of mask aligner, therefore, this error source cannot be avoided. This problem is also critical for the process performing on SU-8 sloped walls. Another factor that affect the alignment accuracy is the dimension of fabricated sloped walls. Together with the error source of distance (d), it is experimentally figured out that performing mask alignment on narrow sloped walls is very challenging. The width of sloped walls defined by inclined exposure was measured to be about $450\mu\text{m}$ (25 degree sloped angle, $1000\mu\text{m}$ height) which has the comparable size to desired microneedle width ($300\text{-}350\mu\text{m}$).

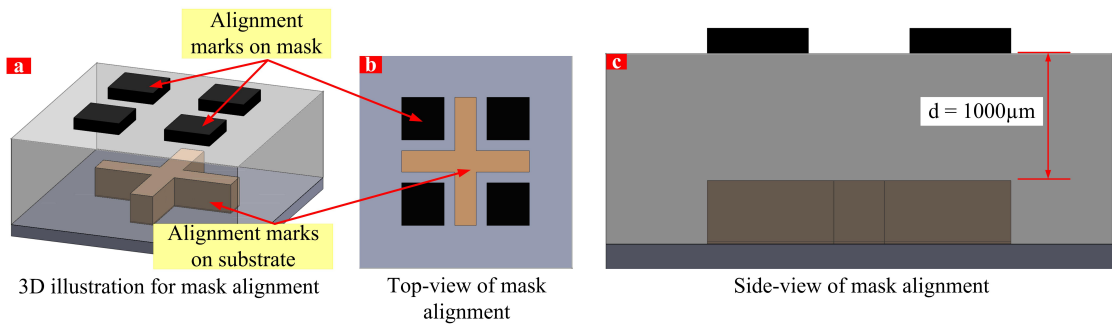


FIGURE 4.18: Misalignment due to the distance between the alignment marks on mask and substrate. A distance between the alignment marks on mask and on substrate is about $1000\mu\text{m}$ i.e. the thickness of second SU-8 layer at step 3 in Fig. 4.16. Therefore, the alignment marks cannot be brought into focus at the same time, thus leading to alignment error.

4.5.2 Fabrication of TMNs on SU-8 sloped walls

The second experiment was conducted directly on SU-8 sloped walls. By using the pre-defined structures patterned on a hard, non-deformed aluminum substrate, this process is expected to avoid the alignment error caused by thermal expansion of the substrate.

The advantages of SU-8 sloped walls patterned on aluminum substrate are: (i) the sample was no longer be expanded/ contracted upon heating and cooling, the alignment error due to thermal expansion was thus reduced significantly. (ii) the coated SU-8 layer becomes flat and smoother (i.e. no wrinkles on SU-8 surface) since the aluminum substrate is sufficiently stiff to avoid bending and deformation. However, with SU-8 sloped walls, separation of microneedles was more difficult due to strong adhesion between cross-linked SU-8 microneedles and SU-8 sloped walls. The microneedle tips were damaged as depicted in Fig. 4.20*b, c*.

One possible reason is the small angle of fabricated sloped walls. In fact, the microneedles are not strong enough with extremely sharp tips due to small sloped wall angle. Therefore, the tips will be broken easily during microneedle separation. The solution is to fabricate the

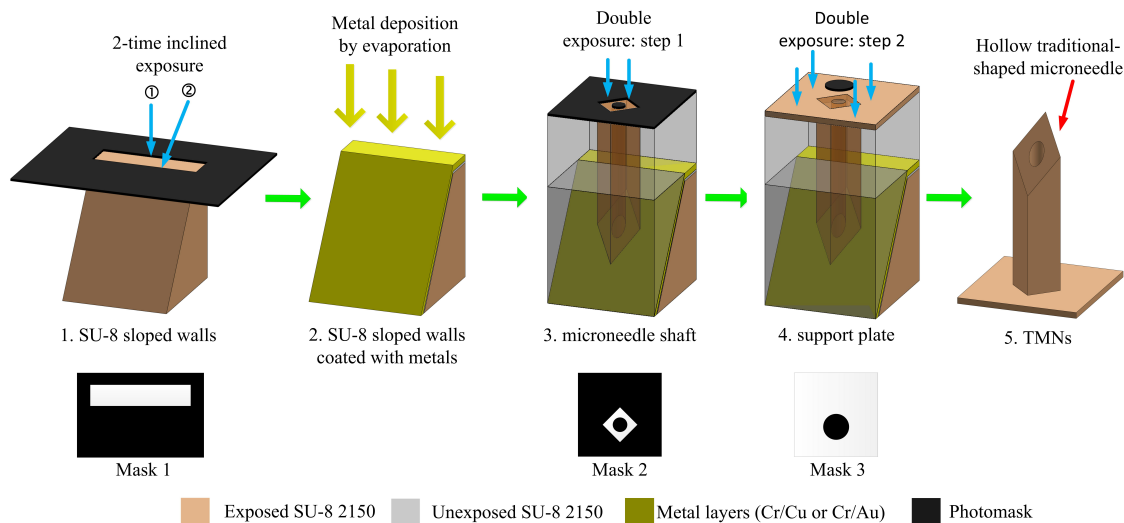


FIGURE 4.19: Process flow for fabrication of TMNs on SU-8 sloped walls. Step 1: SU-8 sloped wall; Step 2: PDMS sloped wall; Double exposure: step 3: formation of microneedle shaft, step 4: formation of support plate; Step 5: desired TMNs.

sloped wall with higher angle. However, in practice, it is not possible due to light refraction. Therefore, the surface of SU-8 sloped walls need to be modified, otherwise the microneedle tips will be damaged. In addition, surface modification may also provide better encapsulation of SU-8 into the trenches between sloped walls, i.e. less effort is required for degassing. Normally, anti-sticking layers are performed by chemical spinning. However, with $1000\mu\text{m}$ -tall sloped walls, uniform coating via spinning is not possible to achieve. The suggested technique is to use vapour deposition. In this experiment, I utilized two techniques to perform surface modification: vapour deposition of silane in vacuum chamber; thermal deposition of metals: 20nm Cr and 500nm Cu, 20nm Cr and 20nm Au. It is showed that metal coatings improved significantly SU-8 encapsulation. The experimental results showed that it was easier to separate the needles from metal coated SU-8 sloped walls than form original SU-8 sloped walls. However, some of microneedle tips still got damaged after separation. There are two phenomena that could possibly be the reason for this, including: (i) Narrow sloped walls could be the reason for weak bevel tips. The sloped walls were fabricated with the sloped angle of 25° , thus weakening the microneedle tips; (ii) The adhesion of coated metal layers on SU-8 sloped walls is not as good as on silicon wafer or metal substrate. After separation step, at some arrays the metal layers were lifted off and stick to the microneedle tips.

In the process on SU-8 sloped walls, it was very difficult to have perfect alignment when performing the second exposure step in double exposure technique. Two error sources are: (i) the distance between mask and alignment marks on sample; (ii) narrow lithographically patterned sloped walls. These two issues were addressed before in the process on PDMS sloped walls.

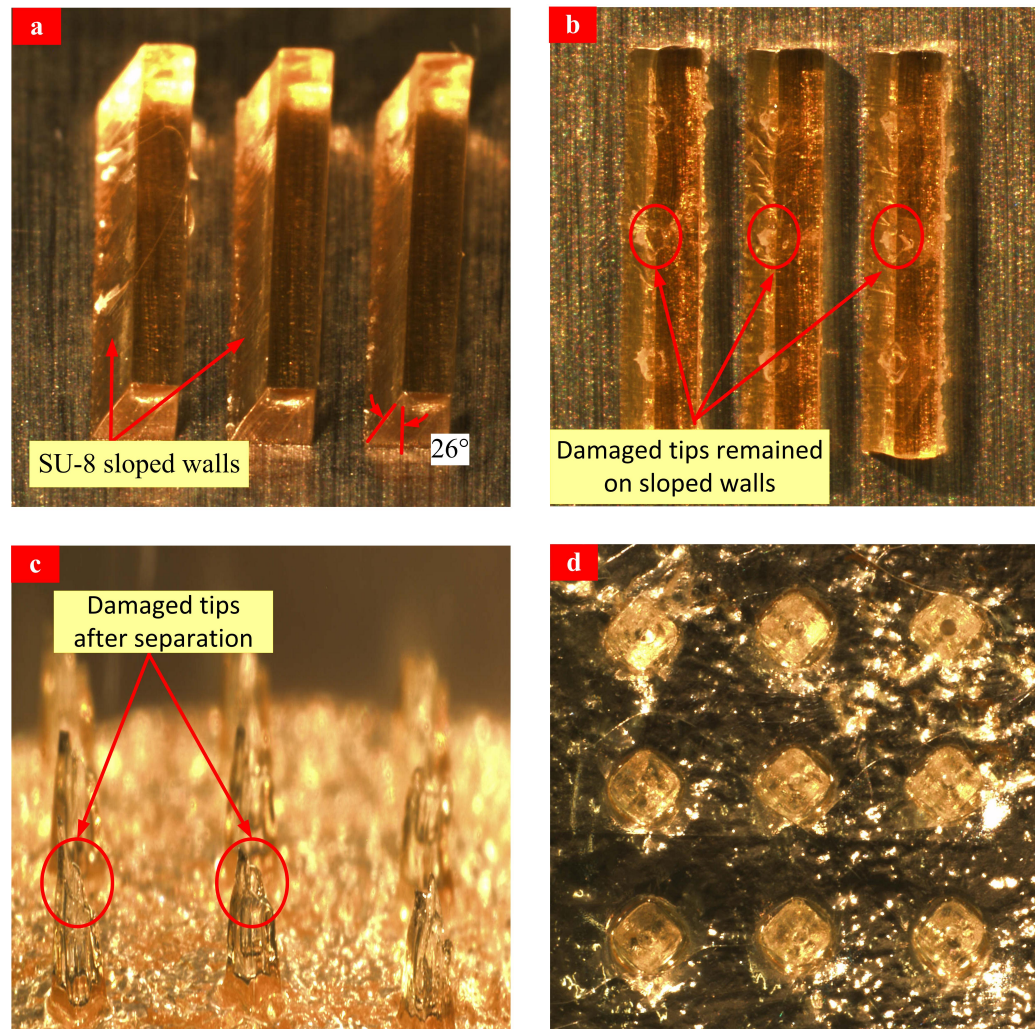


FIGURE 4.20: Tip-damaging problem caused by strong adhesion between microneedles and the sloped walls. (a) SU-8 sloped walls, (b) Damaged tip parts remained on SU-8 sloped walls, (c) Fabricated TMNs with damaged bevel tips, (d) a top-view image which verifies the existence of microneedle hollows. The figures were captured by Olympus MVX10.

4.5.3 Fabrication of TMNs on CNC-machined aluminum sloped walls

After experiments on PDMS sloped walls and SU-8 sloped walls, to address the remaining issues, a new promising approach to produce SU-8 TMNs was proposed. This approach utilized the CASW for creating the bevel tips. Instead of fabricate the sloped walls by SU-8 photolithography, the ideal of this approach is to fabricated the sloped walls with precise mechanic technology. For instance a Computerized Numerically Controlled (CNC) machine is one promising option with extremely high resolution (up to 0.01mm). The advantages of CASW are discussed in Appendix B which also presents the detailed experiments on three aluminum samples. Fig. 4.21 shows three types of sloped walls made by PDMS, SU-8 and aluminum.

Table 4.3 summaries the main limitations associated with PDMS sloped walls and SU-8 sloped walls. It also addresses the expecting superiority of CNC-machined sloped walls. It

can be observed that PDMS sloped wall provides better possibility to release the microneedle arrays compared to SU-8 sloped walls (without surface modification). However, PDMS mould induces several problems, for example bending, deformation, alignment accuracy and bad profile of coated SU-8 layer. On the other hand, SU-8 sloped walls patterned on aluminum plate can avoid the problems of substrate bending and wrinkles. But two factors of distance (d) between mask and substrate (Fig. 4.18) and limited sloped angle still remained.

TABLE 4.3: Summary of the advantages and disadvantages of TMNs fabrication on three different sloped walls, including: PDMS sloped walls (Fig. 4.21a), SU-8 sloped walls (Fig. 4.21b) and CNC-machined aluminum sloped walls (CASW) (Fig. 4.21c).

Material	Advantages	Disadvantages
PDMS sloped walls	- Low adhesion with crosslinked SU-8, easy to release the microneedles	- Large surface tension (PDMS and SU-8), difficult to perform SU-8 encapsulation. - Misalignment caused by: (i) thermal expansion (mask compensation is required), (ii) distance between alignment marks on mask and substrate, (iii) limited sloped angle.
SU-8 sloped walls	- No bending, no misalignment caused by thermal expansion.	- Tip damaging due to strong adhesion with crosslinked SU-8. Surface modification is required. - Misalignment caused by: (i) distance between alignment marks on mask and substrate, (ii) limited sloped angle.
CASW	- Flexible design dimension (height, width, sloped angle) - Better process control. - Better accuracy in mask alignment. - Microneedle length controllable with coating barrier. - Reusable sample with low manufactured cost. - Good repeatability and high throughput	- Tip damaging due to strong adhesion with crosslinked SU-8. Surface modification is required.

As can be seen from Table 4.3, the issues associated with the process on PDMS and SU-8 sloped walls limited the quality of fabricated microneedles and the overall throughput. A solution of CNC-machined aluminum sample (CAS) was introduced with the expectations to overcome the remaining limitations of SU-8 sloped walls. The advantages of CAS are listed in Table 4.3. The detail description for each advantage of CAS is presented in Appendix B. Appendix B summarizes the process to optimize method 2 for using on CAS. It is located

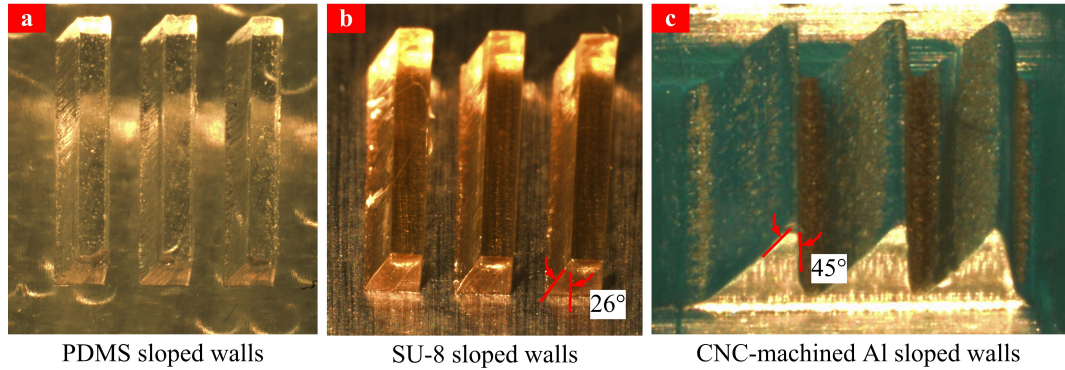


FIGURE 4.21: Three different types of sloped walls. (a) PDMS sloped walls, (b) cross-linked SU-8 sloped walls, (c) CNC-machined aluminum sloped walls.

separately to provide a detail picture of the key contribution of this thesis. In this part, two main advantages are described, including:

(i) *High flexibility in design of sloped wall dimensions*: the sloped walls can be flexibly designed with various dimensions. Therefore, sloped walls with higher angle are experimentally proved to improve the alignment accuracy. Fig. 4.22 shows the 3D sketches of CAS in Solidworks. Various sloped angle can be designed, however, in practice, the CAS was manufactured with the angle of 45° . One single angle of sloped walls simplify the manufacture process, thus saving cost and time. Fig. 4.21 shows the aluminum sloped walls fabricated with 45° sloped angle, $12\mu\text{m}$ height and $1200\mu\text{m}$ width. This width is larger than of PDMS and SU-8 sloped walls ($400\text{-}450\mu\text{m}$). Therefore, it is easier to position mask 1 (see step 3 in Fig. B.4).

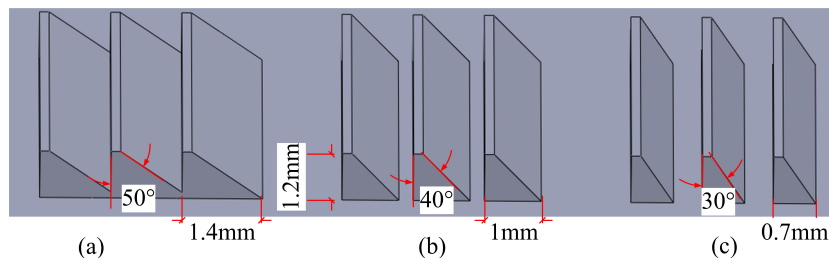


FIGURE 4.22: Highly flexible design of CNC-machined aluminum sloped walls. Aluminum sloped wall with the sloped angle of (a) 50° , (b) 40° , (c) 30° .

(ii) *Improvement in mask alignment*: the aluminum sample was designed with alignment marks positioned at top surface, thus avoiding the alignment error. There is no gap between alignment marks on mask and substrate ($d = 0$, see Fig. B.1 in Appendix B. Therefore, the alignment marks can be brought into focus at the same time, thus improving alignment accuracy.

On the other hand, there was one issue associated with method 2 on CAS - tip damaging in microneedle separation. The reason for this problem is the high adhesion between crosslinked SU-8 microneedles and the substrate. Previously, an experiment conducted on SU-8 substrate illustrated that Cr/Au worked best. However, in this case, aluminum sloped walls were utilized, therefore, another experiment is required. An experiment was conducted on one

CAS sample which has four regions coated with four materials, including: Cr/Au, Cr/Cu, silane and aluminum. The detailed experiment is presented in section B.1 in Appendix B. Again, the results confirmed that the region coated with Cr/Au provided highest possibility to successfully release the microneedles arrays.

In relation to the fabrication of microneedles on CAS, three experiments were conducted on three aluminum samples to fabricate the TMNs. The sample process as applied for PDMS sloped walls was utilized. Detail fabrication process is presented in Appendix B. Fig. 4.23 shows the TMNs fabricated with different lengths. Specifically, three aluminum samples were utilized with $700\mu\text{m}$, $1000\mu\text{m}$ and $1500\mu\text{m}$ in the height of coating barrier. Correspondingly, different microneedle lengths of $645\mu\text{m}$, $950\mu\text{m}$ and $1410\mu\text{m}$ were fabricated as shown in Fig. 4.23 a-c, respectively. In addition, the microneedles arrays were successfully fabricated with pitch size of $1500\mu\text{m}$.

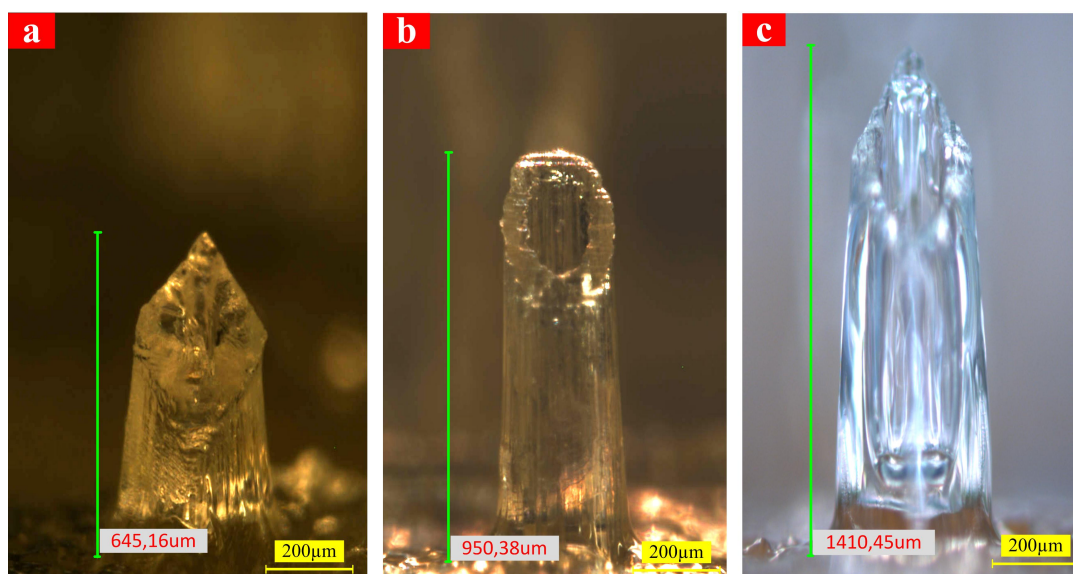


FIGURE 4.23: Optical micrographs of SU-8 TMNs fabricated with three different lengths. The microneedle length was measured to be (a) $645\mu\text{m}$, (b) $950\mu\text{m}$, (c) $1410\mu\text{m}$. The length was controlled by the height of coating barrier.

4.6 Chapter conclusions

The experiment part in this thesis aims to develop a simple, cost-effective method for fabrication of polymer-based microneedles. The process development started from method 1 (Replication of microneedles) and improved to method 2 (Direct formation of microneedles). Method 2 was introduced to overcome some limitations of method 1, providing higher capability to fabricate the polymer-based hollow microneedles. Our experiments confirmed that method 2 is relatively better than method 1 in terms of the quality of fabricated microneedle tips, repeatability, fabrication time, and cost. Specifically, when performing PDMS molding/unmolding, the high-aspect-ratio structures were easily broken, thus leading to the

imperfection or destruction of the final molded microneedles. In addition, the possibility of successfully fabricating microneedle hollows in method 2 is higher than that of method 1. The effect of light scattering was more critical because of the large opening area. In method 2, microneedle separation is easier. The process of method 2 was studied and optimized before proposing an optimal process. Two scenarios were conducted on PDMS and SU-8 sloped walls for investigation of the important factors, for example: tip damaging, substrate bending, deformation, misalignment problem...etc. Based on what have been found, an optimal process was proposed on the CNC-machined aluminum samples which were utilized as the replacement for lithographically patterned sloped walls.

The process of method 2 utilized for fabrication of TMNs can also be applied to fabricate PMNs. However, one thing should be considered during the fabrication of pyramidal tips is that the sharpness of pyramidal tips fabricated by using 4-time inclined exposure method was limited. The shape of pyramid tips was affected by the inaccurate rotations. During relative rotation of the top part (as described in Fig. 4.4a), the error may occur causing imperfect pyramidal side faces. Moreover, partially-exposed SU-8 may also affect the tip-size. One alternative to make the pyramidal tips, is using anisotropic wet etching on $\langle 100 \rangle$ silicon wafer. The fabrication of sub-micron pyramidal trenches was achievable [80, 81]. However, the tip angle is therefore about 70.6° , the pyramidal tips are then limited to about $200\mu\text{m}$ -high.

In addition, this chapter gives the answer for the motivating question number 2: "Question 2: Is it possible to fabricate and integrate the microneedle array with the proposed geometry? If yes, what kind of technologies can be applied to fabricate it? If yes, what kind of technologies can be applied to fabricate it?". The answer is yes. The microneedles with the proposed dimensions are manufacturable. The fabrication results can be summarized as follows:

1. Pyramid-shaped microneedles (PMNs): the microneedles were fabricated by using method 1 - molding of microneedles. The measured dimensions of fabricated PMNs are: $1470\mu\text{m}$ in length, $300\mu\text{m}$ in based width with the pyramidal tips of $43\mu\text{m}$.
2. Traditional-shaped microneedle (TMNs):
 - PDMS sloped walls: the $1515\mu\text{m}$ -tall TMNs were formed with the tip-size of $39\mu\text{m}$. Misalignment due to PDMS thermal expansion was observed.
 - SU-8 sloped walls: the quality of fabricated microneedles was not good. Most of the microneedles were damaged or broken, especially at the microneedle tips. Tip damaging was occurred when separating the microneedle arrays. This problem was caused by strong adhesion between microneedle and SU-8 sloped walls.
 - CNC-machined aluminum sloped walls: the microneedles were fabricated with different lengths: $645\mu\text{m}$, $950\mu\text{m}$ and $1410\mu\text{m}$ corresponding to three experiments

on three CNC-machined aluminum samples manufactured with 700 μm , 1000 μm and 1500 μm -high coating barrier, respectively. The average tip-size was measured to be 23 μm . Bevel tips were constructed in a good quality.

In conclude, method 2 performing on CNC-machined sloped walls provides good repeatability with high throughput. Three experiments were successfully conducted to produce the microneedles with the desired lengths and sharp tips. The proposed process only has one issue of tip-damaging during separation step. This issue can be addressed by coating two metal layers (Cr/Au) to lower the adhesion between crosslinked SU-8 microneedles and the aluminum surface. More than 97% of the arrays were successfully released in a good condition (e.g. no tip-damaging, flat support plate).

Chapter 5

Performance Evaluation

This chapter describes the procedure to evaluate the performance of the microfabricated microneedles in terms of mechanical properties and skin penetrability. In addition, this chapter gives the answer for two motivating questions:

Question 3: Whether the microneedles as proposed in this thesis can safely penetrate the human skin and can it survive after penetration process?

Question 4: How to evaluate and test it? Does it cause pain or uncomfortable feeling during implementation

This chapter is organized with three sections corresponding to three experiments. Experiment 1 focused on the mechanical strength by measuring the fracture forces and matching of the measured data, calculated results and simulated results. Experiment 2 studied the skin penetrability of the fabricated microneedles. The insertion test was conducted for a single microneedle and the 9x9 microneedle array. Experiment 3 examined skin penetrability of hypodermic metallic needles on human fingers.

5.1 Measurements of fracture forces

The measurement setup on Shear Tester Delvotec 5600 is shown in Fig. 5.1. The microneedle was mounted on the force driving tip. The movement is precisely controlled by a built-in motor with the resolution of 0.01N. To measure the fracture force, a rigid surface (1mm-thick aluminum plate with 69GPa in Young's modulus) was used as a penetration object. To minimize the effect of slippery, a thin layer of epoxy resin UN3082 was spun on aluminum plate. This layer provided a softer surface to immobilize the microneedle tip during measurement. The measurement error due to slippery thus can be minimized.

Measurements were conducted repeatedly three times for each of pyramid-shaped microneedles (PMNs) and traditional-shaped microneedles (TMNs). The results are shown in Table 5.1. Force-time plot was recorded and displayed on the screen as shown in Fig. 5.2. Failure point was determined automatically by the system when there is a sudden decrease of applied force. There are two points at which the microneedles were broken corresponding to tip failure and shaft failure. PMNs exhibited higher fracture forces (2.74N for tip failure and 3.45N for shaft failure) compared to TMNs (0.46N for tip failure and 2.32N for shaft failure). The average measured forces are presented in Table 1. In comparison with the results from theoretical study, the average differences in percentage are $\bar{\Delta} = 8.16\%$ and $\bar{\Delta} = 29.5\%$ for PMNs and TMNs, respectively. When the microneedle tip is broken, the total length is reduced. Fracture force thus increased. With average tip-fracture force of 2.82N, pyramidal tip may be stronger than bevel tip which only can withstand to the maximum force of 0.51N.

TABLE 5.1: Measurement of fracture force on fabricated microneedles

	Measured force (N)				Calculated force (N)	$\bar{\Delta}$ (%)
	Shaft failure	$\bar{\sigma}$	Tip failure	$\bar{\sigma}$		
PMNs	3.4	1.8%	2.82	2.0%	3.2	8.16
TMNs	2.37	2.1%	0.51	7.8%	1.7	29.5

According to the results from measurements, the hypothesis of the improved strength of PMNs is verified. In comparison to TMNs, PMNs may endure larger axial force, specifically 3.15N (1470 μ length) compared to 2.05N (1515 μ length). As inspected in Fig. 5.2, there are two secondary critical points at 2.74N (Fig. 5.2a) and 0.46N (Fig. 5.2b). At those points, the microneedle tips were initially broken at lower values: 2.74N and 0.46N respectively for PMNs and TMNs. The fractures may be resulted from the force subjection of sharp microneedle tips. However, the measured results of tip fracture force verifies the improved strength of the pyramidal tips as compared with that of the bevel tips.

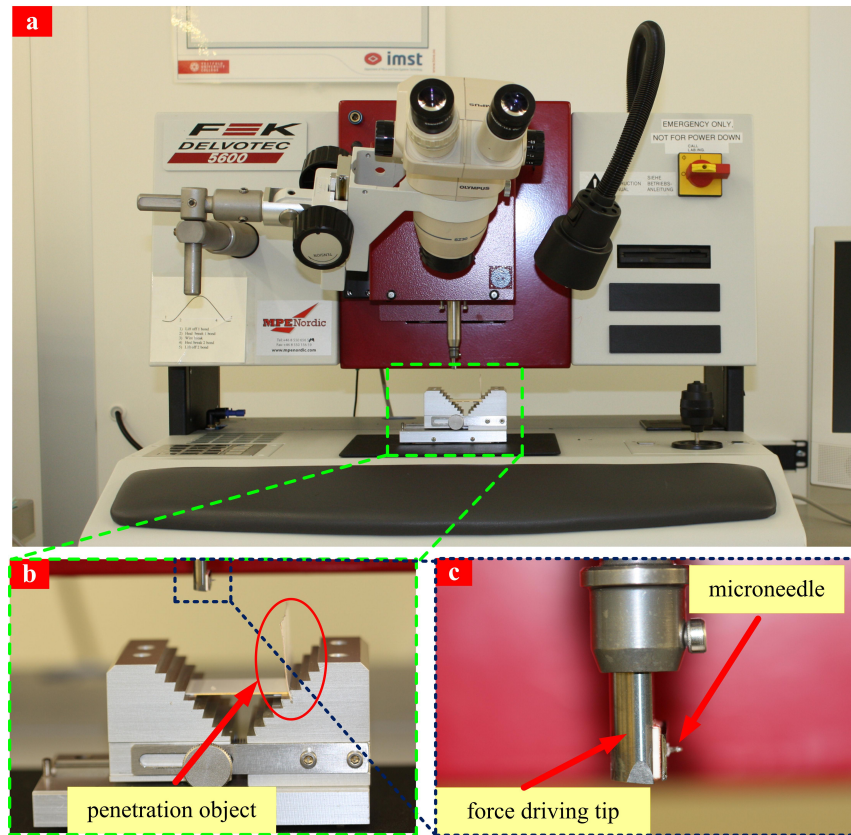


FIGURE 5.1: Measurement setup with Shear tester Delvotec 5600. (a), (b) equipment setup, (c) microneedle mounted on force driving tip. Microneedle array was bonded to the metallic surface by using a two-side copper tape. The test was conducted with an aluminum plate as the penetration object.

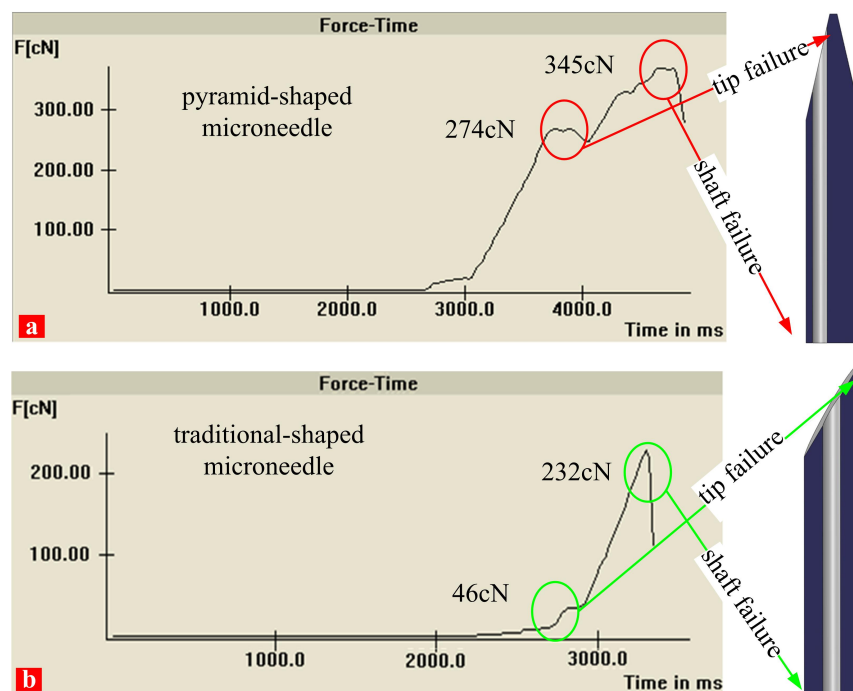


FIGURE 5.2: Measurement results of fracture force of PMNs and TMNs. The forces were recorded as a function of applying time. (a) Force-time measurement plot of PMNs, (b) Force-time measurement plot of TMNs.

By comparing the measured forces to the calculated forces of PMNs (3.2N) and TMNs (1.7N), the average force difference between calculated results and measured results is about 8.16% and 29.5% for PMNs and TMNs, respectively. Three possible reasons for this difference could be :

- *Calculation errors*: from the theoretical models. The theoretical models was developed based on several assumptions of geometry and boundary conditions. More specific, with low or average high aspect ratio structural objects, Euler's beam theory is no longer accurate. The effects of shear deformation become more critical. This limitations of the proposed theoretical model was discussed in the chapter conclusion of chapter 3.
- *Measurement errors*: the errors that may caused by the effects of slippery and friction on the testing object (i.e. a rigid aluminum plate). The errors may also come from the measurement setup, however, the accuracy of Shear tester Delvotec 5600 is 1cN (0.01N). So, this error source can be eliminated.
- *Brokenness of microneedle tips*: when the microneedle tips are initially broken at lower force values, the microneedle length will be reduced and the tip dimension will be enlarged. The endurance of the microneedles thus increases, leads to larger measured values of fracture forces.

5.2 Testing of skin penetrability on human fingers

5.2.1 Testing of microfabricated SU-8 microneedles

For practical evaluation, skin penetrability of the fabricated microneedles was assessed on volunteers' fingers through two scenarios. The first and the second scenario was conducted on a single microneedle and a 3×3 microneedles array, respectively. To implement the first test on single microneedle, a microneedle was pressed perpendicularly to the human finger by manually pushing then pulled out by metallic tweezers. On the other hand, with the second test on microneedles array, the volunteers were asked to push their fingers down to the fixed array, then stay at that position for couple of minutes before removing their fingers. The insertion process was optically inspected under the microscope Olympus MVX10.

Scenario 1: *Skin penetrability tested on single microneedle:*

The fabricated microneedles showed to be able to penetrate the skin barrier without breaking. Tip brokenness was not observed when separating the microneedles from human finger. Fig. 5.3a, b show the insertion of a single microneedle into human finger. The insertion spot was then observed under the microscope as illustrated in Fig. 5.3b. One drop of blood came out after pulling the microneedle out.

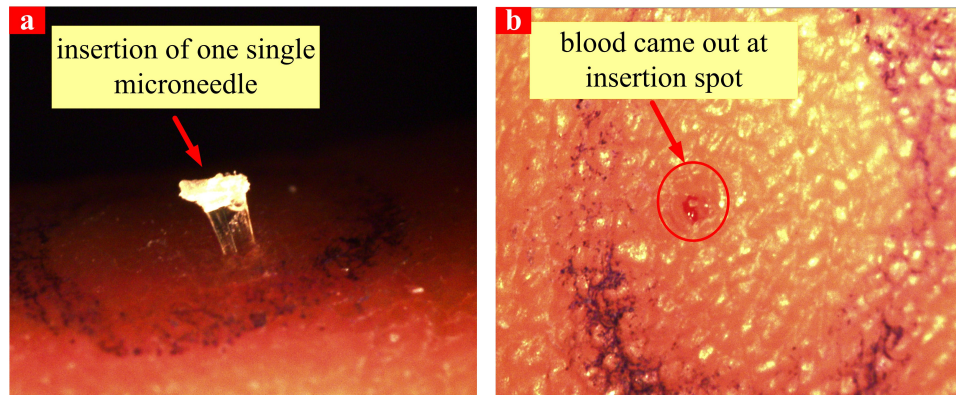


FIGURE 5.3: Scenario 1: Testing of skin penetrability with one single microneedle.

Scenario 2: *Skin penetrability tested on 3×3 microneedles arrays:*

The configuration of 3×3 microneedles array is expected to have two main advantages, including: (i) better opportunity to open the skin and collect blood with higher collection efficiency (9 times more effective than one needle), (ii) easier to perform vertical insertion with an array of 3×3 microneedles. In one test case, one recorded practical issue was the brokenness of the support plate during insertion. The optical illustrations for support plate brokenness are presented in Fig. 5.4. The support plate of the testing sample was measured to be approximately 210 μ m thick (200mW/cm² exposure dosage). The brokenness might be caused either by too large insertion force or too thin support plate.

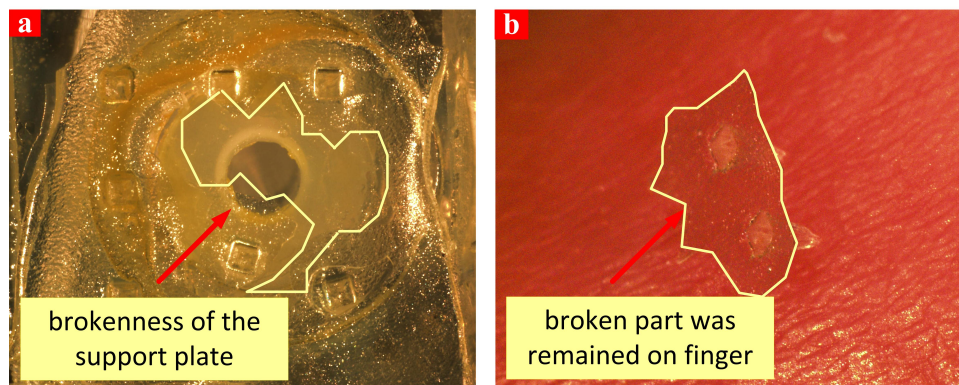


FIGURE 5.4: Brokenness of the support plate during insertion of microneedle array. (a) broken part on the integration of microneedle array, (b) broken part is left on the human skin after the microneedle array was pulled out. The support plate was measured to be about 210 μ m thick.

In practice, the insertion was performed manually. It is thus difficult to predict the exact amount of applied force. Therefore, this possibility was not considered. At each time performing the test, approximately the same force was applied. To deal with this issue, another possible solution is to fabricate the microneedles array with thicker support plate. It was expected to reduce the possibility of support plate brokenness. In practice, the adjustment in support plate thickness can be accomplished by simply increasing the exposure dosage of the second shallow exposure step in double exposure technique. The optimal thickness was

experimentally chosen to be thicker than $300\mu\text{m}$. Fig. 5.5 illustrates a successful skin penetration of a microneedles array fabricated with $330\mu\text{m}$ -thick support plate. Fig. 5.5 shows a successful insertion of an array into human finger. The results indicate that the fabricated microneedles arrays may be able to puncture human finger and reach the blood vessels.

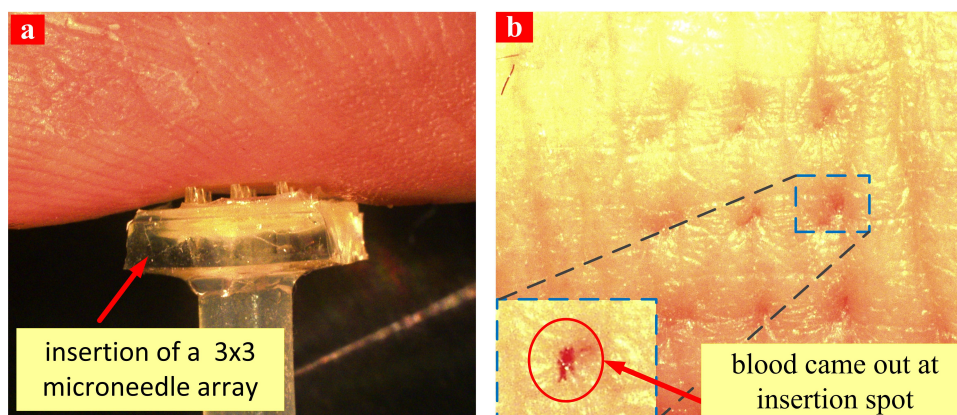


FIGURE 5.5: Scenario 2: Successful insertion of a 3×3 microneedles array. The support plate was measured to be about $330\mu\text{m}$ thick.

The fabricated microneedles arrays were successfully punctured human finger. According to the testing results, the fabricated microneedles were able to be inserted safely into human skin with the configuration of 3×3 microneedles array. It was experimentally shown that the array arranged with $1500\mu\text{m}$ and $2000\mu\text{m}$ microneedle pitch might be easier to puncture the skin compared to the array arranged with $1200\mu\text{m}$ pitch. In both scenarios, after pulling out the microneedles, at the insertion spots, as depicted in red circles in Fig. 5.3b and Fig. 5.5b, blood came out. The presence of blood implies that the microneedles may be able to reach the blood vessels.

The practical tests on human skin provide the preliminary results on the study of skin penetrability of the fabricated microneedles. The results showed that the proposed microneedles may be strong enough to puncture the human skin and long enough to reach the blood vessels at human fingers. The conducted tests are only the initial demonstrations for the mechanical properties of the first prototype of microneedle array. For further verification and validation, a more complex testing protocol is required and the microneedles need to be tested and evaluated again and again before getting close to the conclusion of a functional blood-sampling device.

5.2.2 Testing of hypodermic stainless steel needles

A test of skin penetrability on the hypodermic needle was conducted to give a comparison between the performance of fabricated microneedles and hypodermic needles in clinical applications. Regarding to the manufacture of stainless steel needles, the technologies for mass-production of hypodermic needles (i.e. normal stainless steel needles) are well-developed.

The stainless-steel tube is drawn and cut by using small dies. Extremely sharp bevel tips are manufacturable. Fig. 5.6b shows the comparison between tip-size of the bevel tips of the fabricated SU-8 microneedles and the tip of hypodermic stainless-steel needle. It can be seen that the tip-sizes are comparable. The tips are beveled and polished to be enhance the skin penetrability. In the test, hypodermic needle was inserted gently into volunteer's finger, in other words, the needle was slightly placed on the finger without insertion force. The microneedle tips were able to open the skin nicely and mostly did not cause pain. A blood drop came out after pulling the needle out. This test illustrated that the key factor for successful insertion is the sharpness and tip shape.

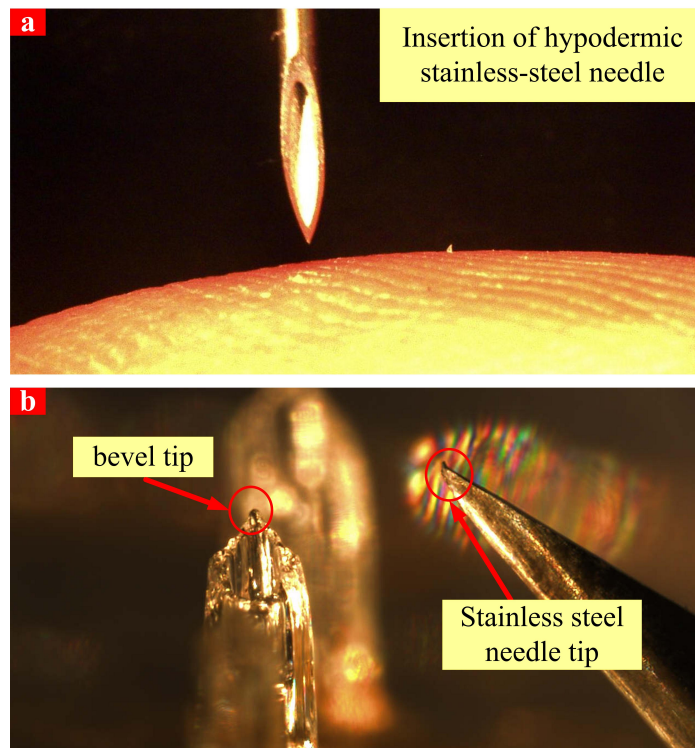


FIGURE 5.6: Testing of skin penetrability with a hypodermic stainless-steel needle. (a) insertion of needle into human finger, (b) tip-size comparison between SU-8 bevel tip and the tip of hypodermic stainless-steel needle.

5.3 Chapter conclusion

Performance evaluation of the fabricated microneedles can be summarized through the answers for two following questions:

Question 3: Whether the microneedles as proposed in this thesis can safely penetrate the human skin and can it survive after penetration process?

Question 4: How to evaluate and test it? Does it cause pain or uncomfortable feeling during implementation.

Firstly, the measurement of fracture force verified the prediction made by theoretical model and finite element method. The measured force is higher than the required insertion force to puncture human skin. Therefore, brokenness may not occur. Secondly, the tests on skin penetrability showed that the fabricated microneedles can puncture the skin. Yes, insertion of fabricated microneedles (single needle and needles array) did cause little pain at the first time when the skin was opened. However, to conclude that it can collect blood, further verification as well as validation are required.

Chapter 6

Conclusion

This thesis has achieved the main goals of design

This project aims to build a blood-sampling microneedle-based device for blood-related disease diagnostic. Firstly, this thesis has achieved three main goals which are: (i) construction of an optimal design of microneedles array with high strength for safer collection of whole blood, (ii) fabrication of SU-8 microneedles array with high aspect ratio, hollow structure and sharp tip. (iii) performing early-stage tests and demonstrations on the performance of the fabricated microneedle array in terms of skin penetrability and collection ability. Secondly, this thesis has contributed to the research field of SU-8 microneedles with three main contributions of this thesis are summarized as follows:

1. Development of a theoretical model for geometry optimization. A model developed to study the fracture force of structural members which are polymer-based microneedles. The accuracy of this model was verified by finite element method and practical measurements. The obtained results from calculations, simulations and measurements, show that the proposed model may be useful for designing microneedles, with high strength for blood extraction. The model can also be applied to other structures of microneedles for geometry optimization. Details about this model is presented in Article P1.
2. Development of a simple, robust method to fabricate SU-8 microneedles. With one single step with SU-8 lithography, a method with the utilization of CNC-machined aluminum sample (CAS) showed to be potentially manufacturable. The advantages of the proposed process are: (i) Low-cost fabrication of CAS, (ii) high flexibility of fabricated microneedles (i.e. different lengths, tip angle) due to controllable CAS dimensions, (iii) a promising method for mass-production of microneedles due to low chemical consumption, good repeatability, CAS reusability and high throughput.

3. Proposing a simple solution, namely "separated lines", to reduce the effect of thermal stress in thick SU-8 films. By separating the arrays with $500\mu\text{m}$ -wide lines, the phenomenon of wafer bending as subjected to thermal stress was greatly reduced.

In addition, this thesis has also provided interesting preliminary results for further development of this project in blood-sampling microneedle-based devices. According to the results from the practical tests on skin penetrability, the sharpness and shape of microneedle tips are the most important factors that determines whether the microneedles can open the skin and collect blood or not. It is therefore suggested that the studies on blood-collection microneedles should focus on fabrication of microneedles with extremely sharp tips. The sharpness of microneedle tips is the limitation remained in the experiment part in this thesis. There are several potential approaches, for example:

- *Sharper microneedles are achievable higher higher-resolution CNC-machined aluminum sample:* the aluminum surface could be polished before being used in order to reduce the roughness, thus improving the profile of fabricated tips.
- *Gray tone lithography - a new approach to fabricate complex 3D structure:* with gray tone mask, complex 3-dimensional SU-8 structures can be fabricated by using gray-scale photolithography [82, 83]. The principle is to control the distribution of features patterned on the photomasks, thus control the exposure dosage of the UV light.
- *The method to produce and sharpen the fabricated microneedle:* to minimize as low insertion pain as possible, diminutive tips are highly desirable. The sharp tips may gently open the skin and take out blood without causing hurt. One worthy studied approach is the fabrication of sharper microneedles with higher-resolution CNC samples in method 2.
- *Fabrication of metallic microneedles:* Metallic microneedles may also be a good option for extremely sharp microneedle tip. To fabricate metallic microneedles, electrode plating is one of the most frequently-used approach for metal deposition.

Regarding to practical operation of microneedles, in the future research, two aspects should be considered in order to manufacture the functional devices, including: (i) packaging of the microneedles array, (ii) biological verification and validation of functional microneedle prototypes.

Appendix A

Mathematical derivations

In Appendix A, the detailed expressions of $I_z(x)$, $Q_z(x,y)$ and $D(x,y)$ for cross-section region 2-5 were respectively derived. The two most complicated cross-sectional areas are at region 3 and 4. The illustrations to calculate $I_z(x)$ for regions 3 and 4 are presented in Fig. A.1 b, c. The results are presented below:

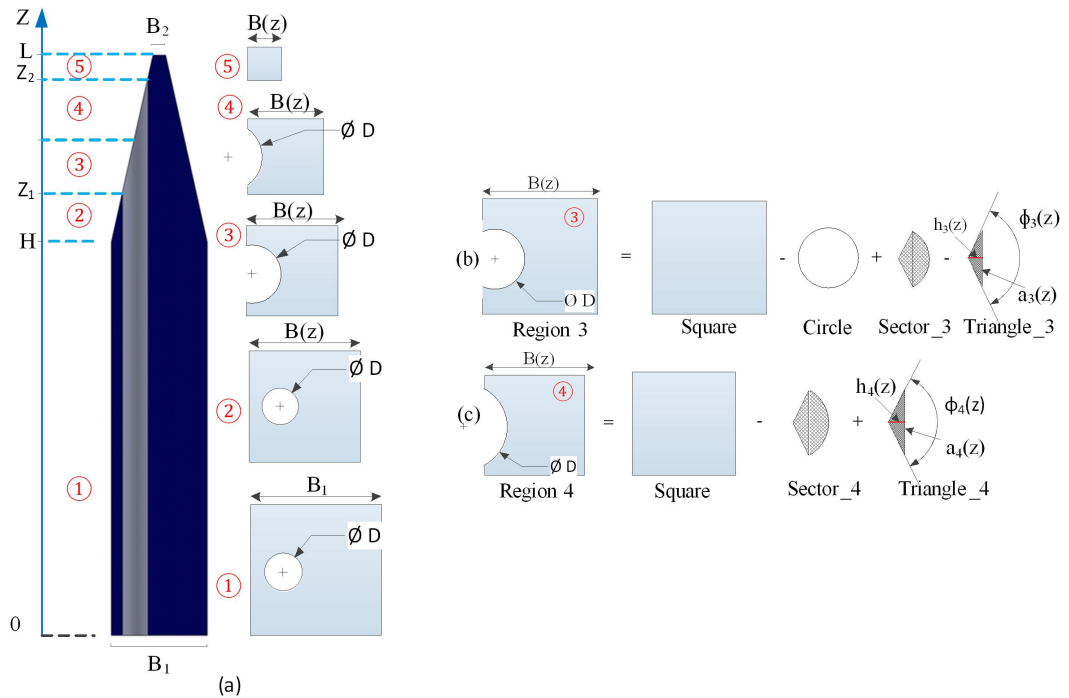
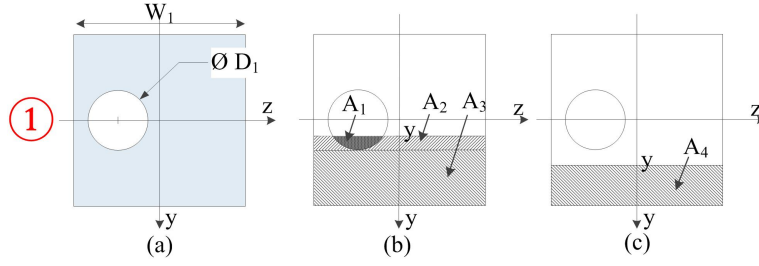


FIGURE A.1: Five cross sections of PMNs. (a) five cross sections correspond to five regions along z-direction; (b), (c) illustrations for calculation of inertia moment in Regions 3 and 4, respectively. They are the most difficult regions for calculating inertia moment due to the dependence on z of all geometrical variables.

1. **Region 1:** x from *Tip* to L FIGURE A.2: Cross section at region 1. (a) inertia moment, (b), (c) illustrate for Q_{1a} and Q_{1b} (a) **Second moment of area $I_z(\mathbf{x})$:**

$$I_1 = \frac{W_1^4}{12} - \frac{\pi D_1^4}{4 \cdot 2} \quad (\text{A.1})$$

(b) **First moment of area $Q_z(\mathbf{x}, \mathbf{y})$:**

- y from 0 to R_1

$$Q_{1a}(x, y) = Q_{A_3} + Q_{A_2} - Q_{A_1}$$

$$Q_{1a}(x, y) = W_1 \frac{\frac{W_1^2}{4} - y^2}{2} + W_1 \frac{\frac{W_1^2}{4} - R_1^2}{2} - \int_{\sqrt{-R_1^2 - y^2}}^{\sqrt{R_1^2 - y^2}} \int_y^{\sqrt{R_1^2 - z^2}} y dy dz \quad (\text{A.2})$$

- y from R_1 to $W_1/2$

$$Q_{1b}(x, y) = Q_{A_4}(x, y) = W_1 \frac{\frac{W_1^2}{4} - y^2}{2} \quad (\text{A.3})$$

(c) **Width $D(\mathbf{x}, \mathbf{y})$ corresponding to differential dx :**

- y from 0 to R_2

$$D_{1a}(x, y) = W_1 - 2\sqrt{R_1^2 - y^2} \quad (\text{A.4})$$

- y from R_1 to $W_1/2$

$$D_{1b}(x, y) = W_1 \quad (\text{A.5})$$

2. **Region 2:** x from X_2 to *Tip*(a) **Second moment of area $I_z(\mathbf{x})$:**

$$I_2 = \frac{W(x)^4}{12} - \frac{\pi D_2^4}{4 \cdot 2} \quad (\text{A.6})$$

(b) **First moment of area $Q_z(\mathbf{x}, \mathbf{y})$:**

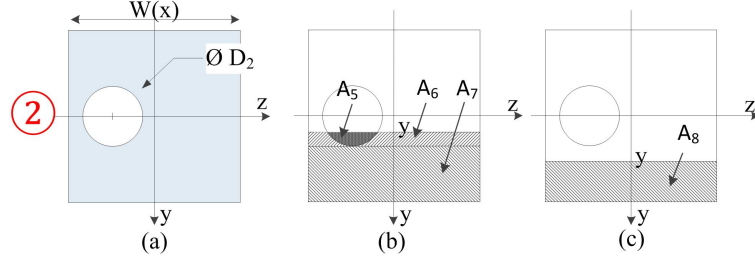


FIGURE A.3: Cross section at region 2. (a) inertia moment, (b), (c) illustrate for Q_{2a} and Q_{2b}

- y from 0 to R_2

$$\begin{aligned}
 Q_{2a}(x, y) &= Q_{A_7} + Q_{A_6} - Q_{A_5} \\
 &= W(x) \frac{\frac{W(x)^2}{4} - y^2}{2} + W(x) \frac{\frac{W(x)^2}{4} - R_2^2}{2} - \int_{-\sqrt{R_1^2 - y^2}}^{\sqrt{R_2^2 - y^2}} \int_y^{\sqrt{R_2^2 - z^2}} y dy dz
 \end{aligned} \tag{A.7}$$

- y from R_2 to $W_x/2$

$$Q_{2b}(x, y) = Q_{A_8}(x, y) = W(x) \frac{\frac{W(x)^2}{4} - y^2}{2} \tag{A.8}$$

(c) **Width $D(x, y)$ corresponding to differential dx :**

- y from 0 to R_1

$$D_{2a}(x, y) = W(x) - 2\sqrt{R_2^2 - y^2} \tag{A.9}$$

- y from R_2 to $W_x/2$

$$D_{2b}(x, y) = W(x) \tag{A.10}$$

3. Region 3: x from $(X_1 + X_2)/2$ to X_2

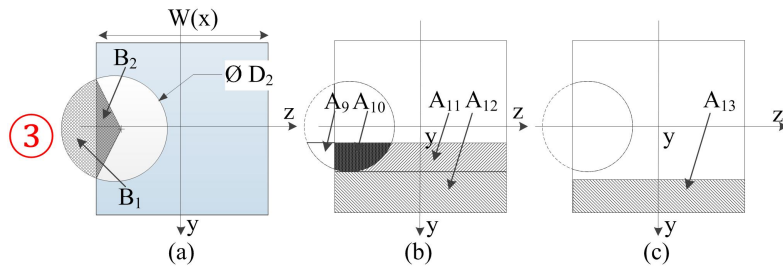


FIGURE A.4: Cross section at region 3. (a) inertia moment, (b), (c) illustrate for Q_{3a} and Q_{3b}

(a) **Second moment of area $I_z(x)$:**

$$\begin{aligned}
 I_3 &= I_{\text{square}.W(x)} - I_{\text{Circle}.D_2} + I_{B_1} - I_{B_2} \\
 &= \frac{W(x)^4}{12} - \frac{\pi D_2^4}{4 \cdot 2} + (\phi_3(x) - 2\sin\phi_3(x)) \frac{D_2^4}{128} - \frac{h_3(x)a_3^3(x)}{48}
 \end{aligned} \tag{A.11}$$

where $h_3(x) = \frac{W(x)}{2} - \frac{W_1}{4}$, $a_3(x) = 2\sqrt{R_2^2 - h_3(x)^2}$ and $\phi_3(x) = 2acrCos\left(\frac{h_3(x)}{R_2}\right)$

(b) **First moment of area $Q_z(x,y)$:**

- y from 0 to R_2

$$\begin{aligned} Q_{3a}(x,y) &= Q_{A_{11}} + Q_{A_{12}} - (Q_{A_{10}} - Q_{A_9}) \\ &= W(x) \frac{\frac{W(x)^2}{4} - y^2}{2} + W(x) \frac{W(x)^2}{4} - R_2^2 - \left(\int_{-\sqrt{R_2^2-y^2}}^{\sqrt{R_2^2-y^2}} \int_y^{\sqrt{R_2^2-z^2}} y dy dz \right. \\ &\quad \left. - \int_{-\sqrt{R_2^2-y^2}}^{-h_3(x)} \int_y^{\sqrt{R_2^2-z^2}} y dy dz \right) \end{aligned} \quad (A.12)$$

- y from R_2 to $W_1/2$

$$Q_{3b}(x,y) = Q_{A_{13}}(x,y) = W(x) \frac{\frac{W(x)^2}{4} - y^2}{2} \quad (A.13)$$

(c) **Width $D(x,y)$ corresponding to differential dx :**

- y from 0 to $a_3(x)/2$

$$D_{3a}(x,y) = W(x) - (h_3(x) + \sqrt{R_1^2 - y^2}) \quad (A.14)$$

- y from $a_3(x)/2$ to R_2

$$D_{3b}(x,y) = W(x) - 2\sqrt{R_1^2 - y^2} \quad (A.15)$$

- y from R_2 to $W_x/2$

$$D_{3c}(x,y) = W(x) \quad (A.16)$$

4. **Region 4:** x from X_1 to $(X_1 + X_2)/2$

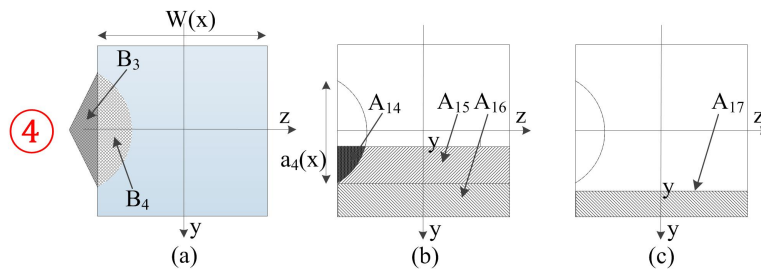


FIGURE A.5: Cross section at region 4. (a) inertia moment, (b), (c) illustrate for Q_{4a} and Q_{4b}

(a) **Second moment of area $I_z(x)$:**

$$\begin{aligned} I_3 &= I_{square-W(x)} - I_{B_4} + I_{B_3} \\ &= \frac{W(x)^4}{12} - (\phi_4(x) - 2\sin\phi_4(x)) \frac{D_2^4}{128} + \frac{h_4(x)a_4^4(x)}{48} \end{aligned} \quad (A.17)$$

where $h_4(x) = \frac{W_1}{4} - \frac{W(x)}{2}$, $a_4(x) = 2\sqrt{R_2^2 - h_4(x)^2}$ and $\phi_4(x) = 2acr\text{Cos}\left(\frac{h_4(x)}{R_2}\right)$

(b) **First moment of area $Q_z(x,y)$:**

- y from 0 to R_2

$$\begin{aligned} Q_{4a}(x, y) &= Q_{A16} + Q_{A15} - Q_{A14} \\ &= W(x) \frac{\frac{W(x)^2}{4} - y^2}{2} + W(x) \frac{\frac{W(x)^2}{4} - \frac{a_4^2}{4}}{2} - \int_{-\sqrt{R_2^2 - y^2}}^{-h_4(x)} \int_y^{\sqrt{R_2^2 - z^2}} y dy dz \end{aligned} \quad (\text{A.18})$$

- y from R_2 to $W_1/2$

$$Q_{4b}(x, y) = Q_{A17}(x, y) = W(x) \frac{\frac{W(x)^2}{4} - y^2}{2} \quad (\text{A.19})$$

(c) **Width $D(x,y)$ corresponding to differential dx :**

- y from 0 to $a_4(x)/2$

$$D_{4a}(x, y) = W(x) - (\sqrt{R_1^2 - y^2} - h_4(x)) \quad (\text{A.20})$$

- y from $a_3(x)/2$ to $W_x/2$

$$D_{4b}(x, y) = W(x) \quad (\text{A.21})$$

5. Region 5: x from 0 to X_1

(a) First moment of area $Q_z(x,y)$:

$$I_5 = I_{\text{square}_W(x)} \quad (\text{A.22})$$

(b) Second moment of area $I_z(x)$:

$$Q_5(x, y) = W(x) \frac{\frac{W(x)^2}{4} - y^2}{2} \quad (\text{A.23})$$

(c) Width $D(x,y)$ corresponding to differential dx :

$$D_5(x, y) = W(x) \quad (\text{A.24})$$

Appendix B

A simple, robust fabrication method with CNC-machined aluminum sample

This part presents the development of a new method which has been developed based on the ideal of method 2. The core ideal of this method is the utilization of a CNC-machined aluminum samples (CAS). This appendix chapter begins with the descriptions for the advantages of CAS followed by the design of CAS. In the experiment part, three scenarios were conducted on three CAS manufactured with three different heights of coating barrier. Three types of traditional-shaped microneedles (TMNs) were fabricated with $645\mu\text{m}$, $950\mu\text{m}$ and $1410\mu\text{m}$ in length. Very sharp bevel tips with the with the tip-size of $23\mu\text{m}$ were manufacturable.

B.1 Advantages of CNC-machined aluminum sample in microneedle fabrication

As mentioned in chapter 4, 5, a sample made by aluminum with pre-defined structures is an promising replacement for SU-8 sloped walls. This replacement may greatly improve the quality of fabricated microneedles as well as the fabrication process itself. Moreover, with CAS, the possibility to develop a low-cost, simple method with high throughput becomes more potential. Most importantly, it can give the solutions to overcome several fabrication issues associated with SU-8 and PDMS sloped walls. The advantages of CNC-machined aluminum sloped walls (CASW) are presented as follows:

- (i) **Flexible design dimension:** high flexibility with controllable dimension of sloped walls (i.e. sloped angle, height and width of sloped walls). With CASW, the limitation in sloped

angle can be solved (maximum degree angle = 25).

(ii) **Better process control:** with significantly stronger aluminum plate, it is able to solve the problems of wafer bending (SU-8 sloped walls) and thermal expansion (PDMS sloped walls)

(iii) **Better accuracy in mask alignment:** the alignment marks are brought to the surface, therefore, there is no gap between the alignment marks on mask and on substrate. The illustration for this improvement is shown in Fig. B.1. In fact, with PDMS and SU-8 sloped walls fabricated with inclined exposure, the existence of the gap ($d = 1000\mu\text{m}$ as depicted in Fig. B.1c, d) cannot be avoided. On the other hand, as can be seen in Fig. B.1b, the CAS is designed with $d = 0$. On the other hand, PDMS and SU-8 sloped walls which were fabricated by using inclined exposure, the existence of the gap ($d = 1000\mu\text{m}$ as depicted in Fig. B.1c, d) cannot be avoided. The alignment marks therefore can be brought into focus at the same time, thus reducing significantly alignment error. Practical demonstration will be presented in the next section.

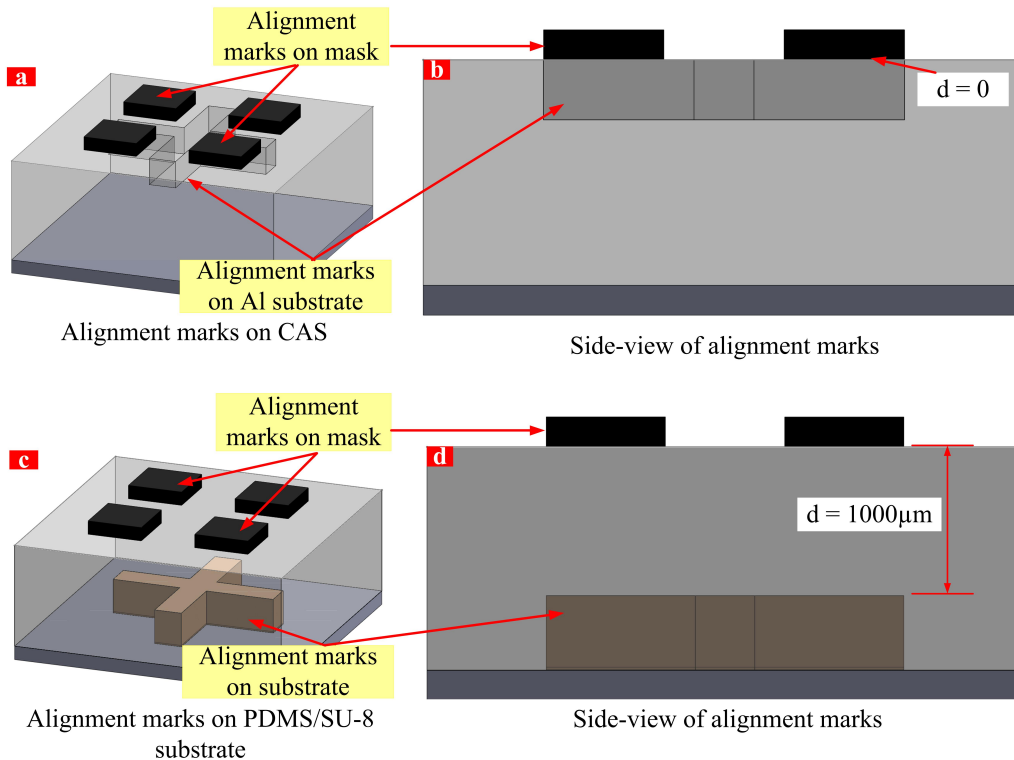


FIGURE B.1: Illustration for the improved accuracy in mask alignment. (a) 3D view, (b) side-view of mask alignment on CAS; (c) 3D view, (d) side-view of mask alignment on PDMS/SU-8 substrate. With CAS, there is no gap between the alignment marks on the mask and substrate in CAS. Therefore, the alignment marks can be brought into focus at the same time, thus improving the alignment accuracy.

(iv) **Microneedle length controllable:** by designing the barrier height which is depicted in Fig. B.2, the length of microneedle shaft can be controlled. Moreover, the barrier also helps to prevent SU-8 flowing out, subsequently leads to a reduction in the thickness of coated SU-8 layer. Microneedles with different length can be fabricated by controlling the height of

coating barrier.

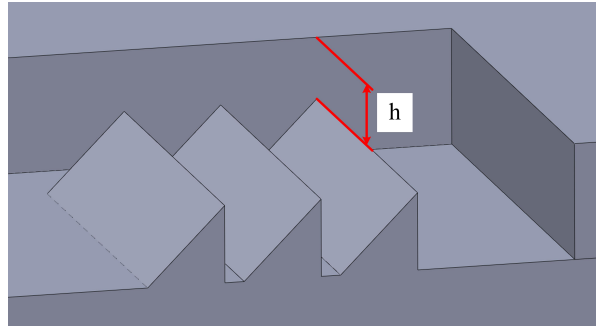


FIGURE B.2: Illustration for coating barrier.

(vi) **Reusable sample with low manufactured cost:** the aluminum sample can be manufactured by using well-established CNC-precision machine which allows fabrication of high-precision sample with reasonable cost. After each process, the aluminum sample can be reused with several cleaning step. With high stability and good strength, the structures are expected to be not damaged after lithography process.

(v) **Good repeatability and high throughput:** the process on aluminum sample enables the possibility for mass production of polymer-based microneedles. In this project, aluminum samples were designed with the size of 3-inch wafer in order to reuse the photomasks. For further project, the aluminum sample can be designed with bigger size, for example with the size of 4", 6" or 8" wafer. It would significantly improve the overall throughput.

B.2 Design of CNC-machined aluminum sloped walls

Three samples with pre-defined CASW were designed by SolidWorks and fabricated by using CNC-precision machine with the resolution of 0.01mm. Specifically, the sloped walls were designed with 45-degree sloped angle, 1.2mm-high and 1.2-wide sloped walls as shown in Fig. B.4. To control the length of microneedles, the outer barrier was designed to be higher than the sloped walls, creating a coating barrier. Coating barrier helps to control precisely the SU-8 thickness, thus controlling the microneedle length. Three samples were fabricated with different barrier height: $h_1 = 700\mu\text{m}$, $h_2 = 1000\mu\text{m}$ and $h_3 = 1500\mu\text{m}$ as depicted in Fig. B.3. With these samples, the microneedle lengths were expected to be $700\mu\text{m}$, $1000\mu\text{m}$ and $1500\mu\text{m}$ with $300\mu\text{m}$ -thick support plate.

B.3 Problem of damaged tips and surface modification

When performing the experiment on original aluminum sample, most of the microneedles were damaged at their tips. The explanation for this would be a high adhesion between

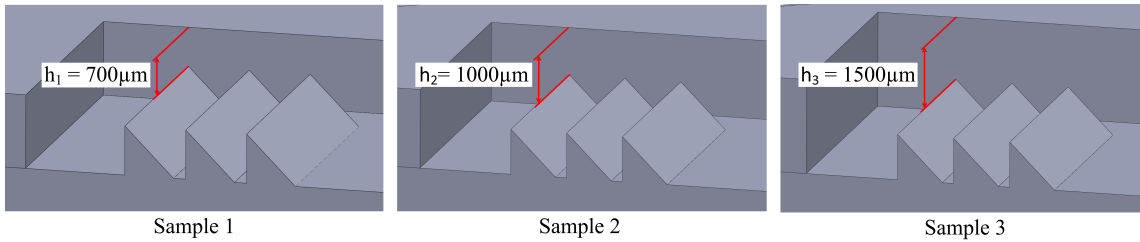


FIGURE B.3: Illustration for three different coating heights. (a) $h_1 = 700\mu\text{m}$, (b) $h_2 = 1000\mu\text{m}$, (c) $h_3 = 1500\mu\text{m}$.

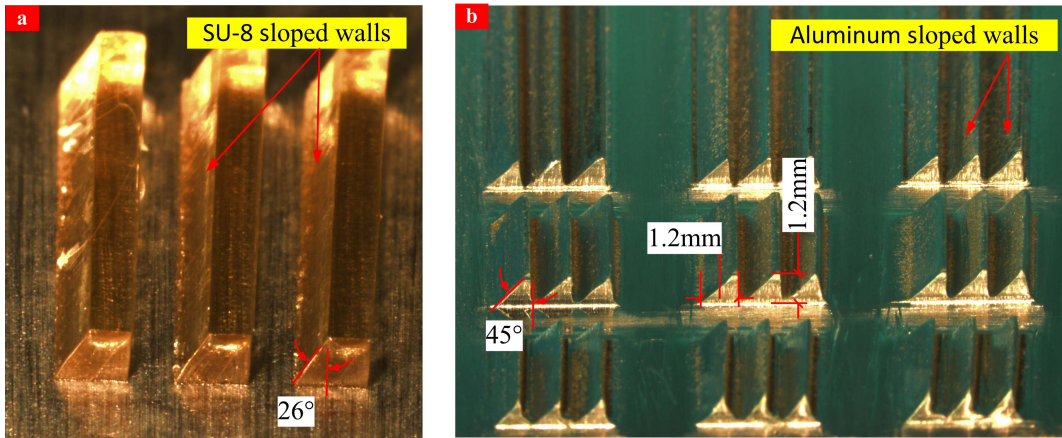


FIGURE B.4: Optical micrographs of SU-8 sloped walls and CNC-machined aluminum sloped walls. (a) SU-8 sloped walls fabricated by 2-time inclined exposure, (b) aluminum sloped walls manufactured by CNC precise-mechanic machine.

cross-linked SU-8 and the aluminum substrate. The broken tips were remained on the sloped walls an result in tip destruction. To solve this problem, the aluminum surface has to be modified. Typically, the suggested method is to coat a layer of material which has lower adhesion with SU-8, for example metals (copper, gold) or anti-sticking chemicals (silane). The prefer method is to perform coating as evaporation. Three materials were utilized to modify the surface of aluminum sample, including silane (vacuum coating), chromium-copper (Cr/Cu) (thermal evaporation), chromium-gold (Cr/Au) (thermal evaporation).

The investigation of the most suitable material for adhesion lowering was performed in scenario 1 on a CAS 1. The sample was divided into 4 regions coated with Cr/Au, Cr/Cu, silane and no coating (i.e. original aluminum surface), respectively. Fig. B.5 presents the distribution of microneedle arrays on 4 regions after 10-minute developing. It can be seen that in region 1 of gold coating, all the arrays were peeled off. On the other hand, only 6 out of 12 arrays in region 2 of copper coating were automatically peeled off after 10-minute developing. In region 3 and 4, there was no automatic separation. The arrays were manually released by using tweezers. The efficiency of each coating material was evaluated through two factors: the percentage of damaged arrays and the mechanism to separate the microneedles. The required development time is important for separating the microneedle arrays as well as the flatness of the support plates. The data was recorded and presented in Table B.1.

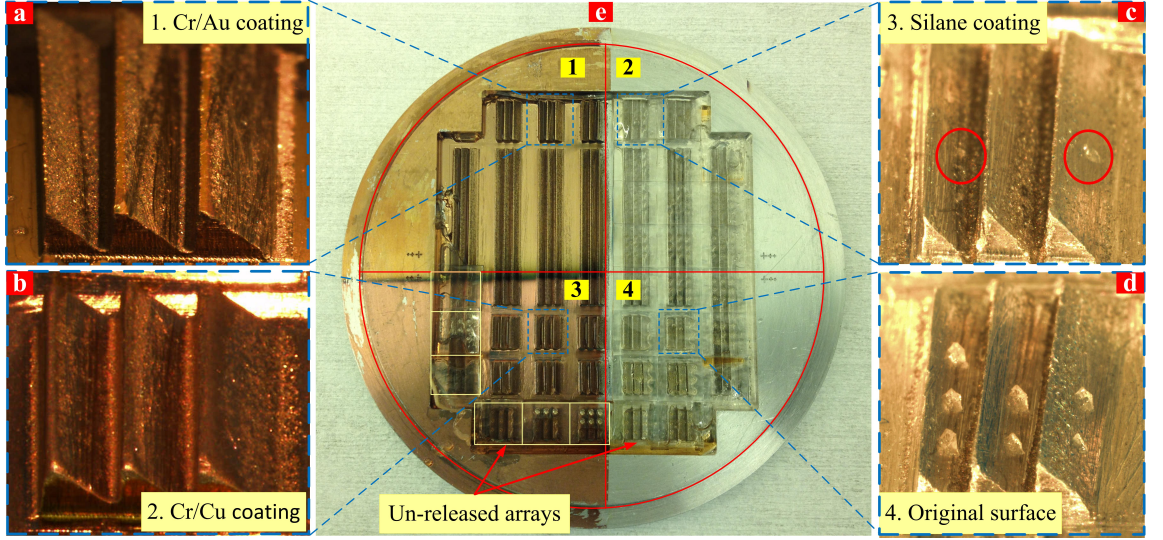


FIGURE B.5: Illustration for three different methods for surface modification. (a) 20nm Cr and 20nm Au coated by using thermal evaporation, (b) 20nm Cr and 500nm Cu coated by using thermal evaporation, (c) silane coated by using vacuum chamber, (d) original aluminum surface, (e) arrangement of 4 regions on aluminum sample. Copper and gold were utilized due to their low adhesion with cross-linked SU-8.

TABLE B.1: Comparison between different methods to lower the adhesion of the surface of CAS.

Scenario No.	Surface modification	Percentage of damaged arrays	Separation method	Quality of the support plate	Development time
1	1. Cr/Au	0% (0/15)	100% self-released	flat	10 minutes
	2. Cr/Cu	40% (6/15)	60% self-released	60% flat	15 minutes
	3. Silane	83% (10/12)	manually released	deformed	25 minutes
	4. Al	100% (12/12)	manually released	deformed	25 minutes
2	Cr/Au	3.7% (2/54)	96.3% self-released	flat	10 minutes
3	Cr/Au	1.8% (1/54)	98.2% self-released	flat	10 minutes

B.4 Fabrication of traditional-shaped microneedles

To demonstrate the advantages of aluminum sloped walls as mentioned above, three CAS were utilized for fabrication of TMNs. The process flow is presented in Fig. B.6. The fabrication process includes three main steps, including: (i) deposition of metal layers (Cr/Au), (ii) double exposure (step 1 and step 2), (iii) microneedle separation. A layer of 20nm-thick chromium was deposited by using thermal evaporation, being used as adhesion layer. A 20nm-thick gold layer was then deposited on the sample coated with chromium. This gold layer is the target layer to reduce the adhesion between the substrate and cross-linked SU-8 microneedles. In addition, surface modification with metallic layers provides better SU-8 encapsulation, less effort is required for degassing. Double exposure technique was performed

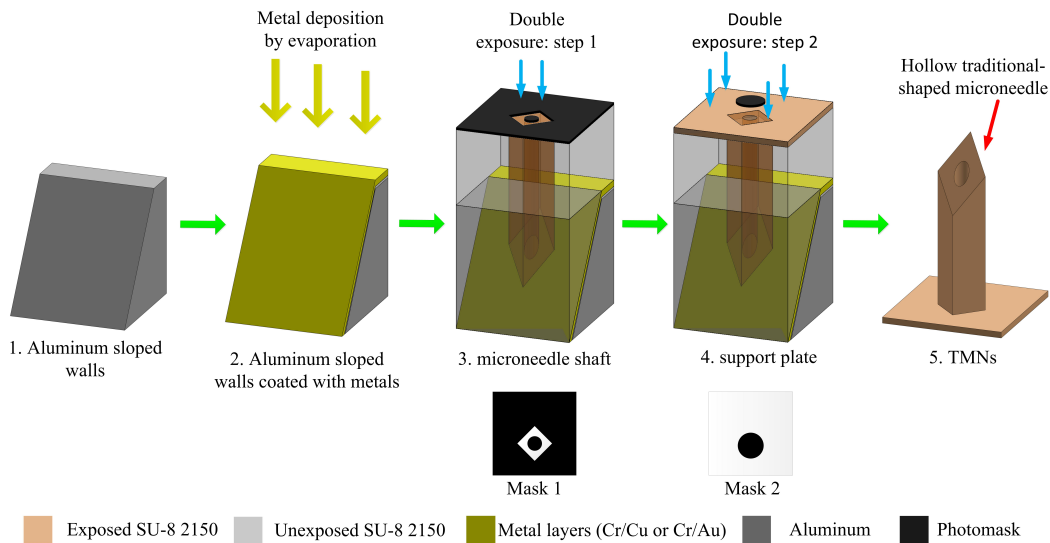


FIGURE B.6: Process flow for fabrication of TMNs using method 2 and CAS.

with exposure dosage of $3000\text{mJ}/\text{cm}^2$ and $300\text{mJ}/\text{cm}^2$ to construct the microneedle shaft and the support plate, respectively. Double exposure technique is illustrated at step 3,4 in Fig. B.6. The sample was developed for 10 minutes in developer mr-Dev 60 with ultrasonic agitation. The microneedles were released automatically during development process. Gentle separation with tweezers may be needed. The aluminum samples were reusable by cleaning with Acetone in ultrasonic machine.

The traditional-shaped microneedles were fabricated with sharp bevel tip ($23\mu\text{m}$ tip-size). Three types of microneedles were fabricated with the total length of $645\mu\text{m}$, $950\mu\text{m}$ and $1410\mu\text{m}$ corresponding to scenario 1, 2 and 3, respectively. It is experimentally showed that the fabrication time was significantly reduced since the first lithography step to form the sloped walls was not performed. More specific, about one third of the fabrication time was saved. In addition, this process showed to be potentially beneficial in terms of chemical consumption, because only one process of SU-8 lithography is needed.

In conclude, the performance of method 2 with the utilization of CAS was greatly improved in term of fabrication quality. With the advantages of less time-consuming, high efficiency in chemical consumption, high throughput and good repeatability, the proposed method is very promising for mass-production of polymer-based microneedle arrays.

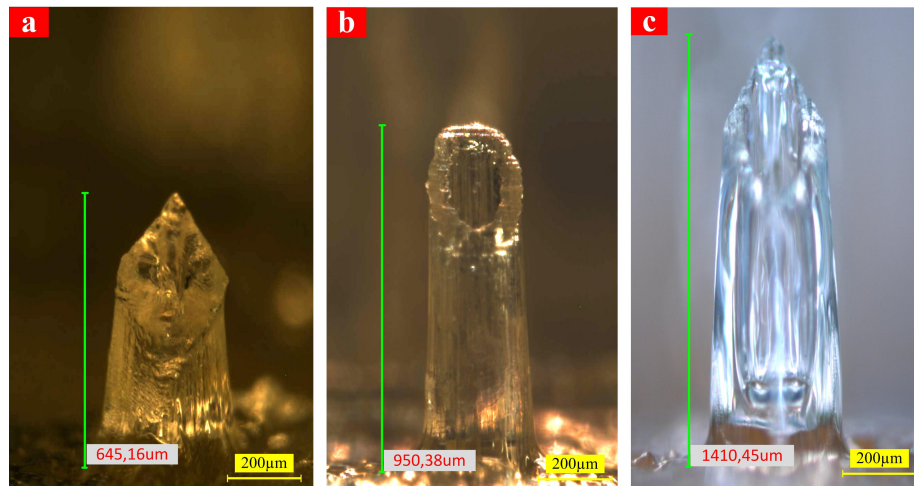


FIGURE B.7: Optical micrographs of SU-8 TMNs fabricated with CNC-machined aluminum samples. The microneedle length was measured to be (a) $645\mu\text{m}$, (b) $950\mu\text{m}$, (c) $1410\mu\text{m}$. The length was controlled by the height of coating barrier.

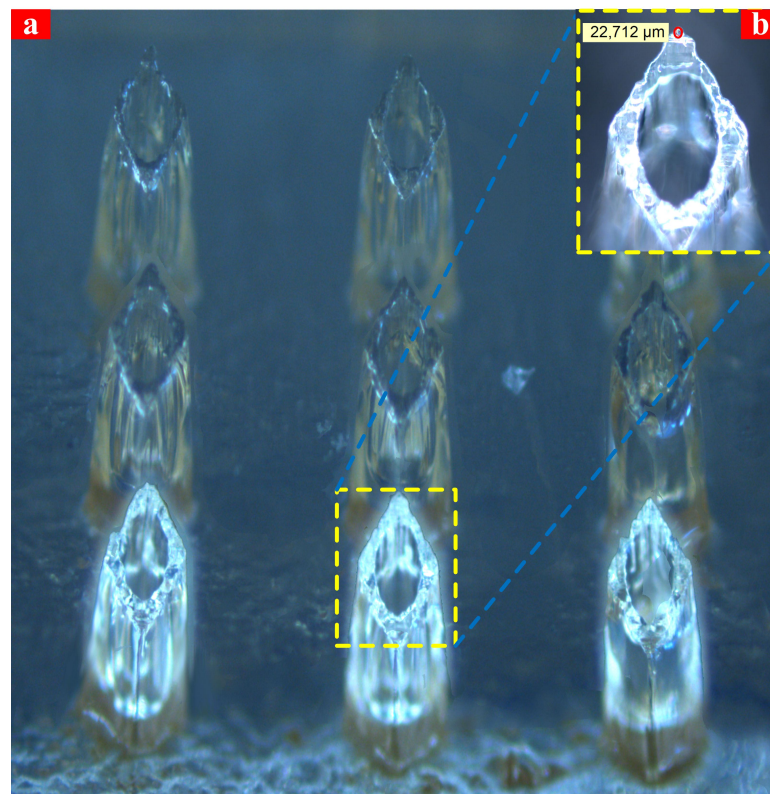


FIGURE B.8: Optical micrographs of microneedle array fabricated with CNC-machined aluminum samples. (a) an array of 3×3 $1410\mu\text{m}$ -long microneedles obtained from scenario 3, (b) focused image of the bevel tip. Tip-size was measured to be approximately $23\mu\text{m}$.

Bibliography

- [1] *Poor blood circulation at fingers*. [Online]. Available: <http://www.buzzle.com/articles/poor-circulation-in-fingers.html>
- [2] J. G. Hamilton, "Needle phobia: a neglected diagnosis." *The Journal of family practice*, 1995.
- [3] M. R. Prausnitz, "Analysis: Overcoming skin's barrier: The search for effective and user-friendly drug delivery," *Diabetes technology & therapeutics*, vol. 3, no. 2, pp. 233–236, 2001.
- [4] P. Zhang, C. Dalton, and G. A. Jullien, "Design and fabrication of mems-based microneedle arrays for medical applications," *Microsystem technologies*, vol. 15, no. 7, pp. 1073–1082, 2009.
- [5] E. Mukerjee, S. Collins, R. Isseroff, and R. Smith, "Microneedle array for transdermal biological fluid extraction and in situ analysis," *Sensors and Actuators A: Physical*, vol. 114, no. 2, pp. 267–275, 2004.
- [6] Winkipedia, *Needle gauge comparison chart*. [Online]. Available: http://en.wikipedia.org/wiki/Needle_gauge_comparison_chart
- [7] R. K. Sivamani, D. Liepmann, and H. I. Maibach, "Microneedles and transdermal applications," 2007.
- [8] R. K. Sivamani, B. Stoeber, G. C. Wu, H. Zhai, D. Liepmann, and H. Maibach, "Clinical microneedle injection of methyl nicotinate: stratum corneum penetration," *Skin Research and Technology*, vol. 11, no. 2, pp. 152–156, 2005.
- [9] K. Kim, D. S. Park, H. M. Lu, W. Che, K. Kim, J.-B. Lee, and C. H. Ahn, "A tapered hollow metallic microneedle array using backside exposure of su-8," *Journal of Micromechanics and Microengineering*, vol. 14, no. 4, p. 597, 2004.
- [10] S.-C. Kuo and Y. Chou, "Novel polymer microneedle arrays and pdms micromolding," *Tamkang J Sci Eng*, vol. 7, no. 2, pp. 95–98, 2004.

-
- [11] C. G. Li, C. Y. Lee, K. Lee, and H. Jung, "An optimized hollow microneedle for minimally invasive blood extraction," *Biomedical microdevices*, vol. 15, no. 1, pp. 17–25, 2013.
- [12] A. Folch, *Introduction to BioMEMS*. CRC Press, 2012.
- [13] B. Stoeber and D. Liepmann, "Arrays of hollow out-of-plane microneedles for drug delivery," *Microelectromechanical Systems, Journal of*, vol. 14, no. 3, pp. 472–479, 2005.
- [14] P. Griss and G. Stemme, "Novel, side opened out-of-plane microneedles for microfluidic transdermal interfacing," in *Micro Electro Mechanical Systems, 2002. The Fifteenth IEEE International Conference on*. IEEE, 2002, pp. 467–470.
- [15] K. Tsuchiya, N. Nakanishi, Y. Uetsuji, and E. Nakamachi, "Development of blood extraction system for health monitoring system," *Biomedical microdevices*, vol. 7, no. 4, pp. 347–353, 2005.
- [16] J.-H. Park, M. G. Allen, and M. R. Prausnitz, "Biodegradable polymer microneedles: fabrication, mechanics and transdermal drug delivery," *Journal of Controlled Release*, vol. 104, no. 1, pp. 51–66, 2005.
- [17] S. Henry, D. V. McAllister, M. G. Allen, and M. R. Prausnitz, "Microfabricated microneedles: a novel approach to transdermal drug delivery," *Journal of Pharmaceutical Sciences*, vol. 87, no. 8, pp. 922–925, 1998.
- [18] N. Wilke, A. Mulcahy, S.-R. Ye, and A. Morrissey, "Process optimization and characterization of silicon microneedles fabricated by wet etch technology," *Microelectronics Journal*, vol. 36, no. 7, pp. 650–656, 2005.
- [19] Y.-T. Chen, C.-C. Hsu, C.-H. Tsai, and S.-W. Kang, "Fabrication of microneedles," *Journal of Marine Science and Technology*, vol. 18, no. 2, pp. 243–248, 2010.
- [20] B. P. Chaudhri, F. Ceyskens, P. De Moor, C. Van Hoof, and R. Puers, "A high aspect ratio su-8 fabrication technique for hollow microneedles for transdermal drug delivery and blood extraction," *Journal of Micromechanics and Microengineering*, vol. 20, no. 6, p. 064006, 2010.
- [21] S. P. Davis, W. Martanto, M. G. Allen, and M. R. Prausnitz, "Hollow metal microneedles for insulin delivery to diabetic rats," *Biomedical Engineering, IEEE Transactions on*, vol. 52, no. 5, pp. 909–915, 2005.
- [22] K. Lee, H. C. Lee, D.-S. Lee, and H. Jung, "Drawing lithography: Three-dimensional fabrication of an ultrahigh-aspect-ratio microneedle," *Advanced Materials*, vol. 22, no. 4, pp. 483–486, 2010.

- [23] S. J. Moon and S. S. Lee, "A novel fabrication method of a microneedle array using inclined deep x-ray exposure," *Journal of Micromechanics and Microengineering*, vol. 15, no. 5, p. 903, 2005.
- [24] S. Khumpuang, M. Horade, K. Fujioka, and S. Sugiyama, "Geometrical strengthening and tip-sharpening of a microneedle array fabricated by x-ray lithography," *Microsystem technologies*, vol. 13, no. 3-4, pp. 209–214, 2007.
- [25] N. Matsuzuka, Y. Hirai, and O. Tabata, "A novel fabrication process of 3-d microstructures by double exposure in standard deep x-ray lithography," in *Micro Electro Mechanical Systems, 2004. 17th IEEE International Conference on. (MEMS)*. IEEE, 2004, pp. 681–684.
- [26] S. Lee *et al.*, "Fabrication of microneedle array using inclined liga process," in *TRANSDUCERS, Solid-State Sensors, Actuators and Microsystems, 12th International Conference on, 2003*, vol. 2. IEEE, 2003, pp. 1546–1549.
- [27] S. J. Moon, S. S. Lee, H. Lee, and T. Kwon, "Fabrication of microneedle array using liga and hot embossing process," *Microsystem technologies*, vol. 11, no. 4-5, pp. 311–318, 2005.
- [28] Y. Choi, M. A. McClain, M. C. LaPlaca, A. B. Frazier, and M. G. Allen, "Three dimensional mems microfluidic perfusion system for thick brain slice cultures," *Biomedical microdevices*, vol. 9, no. 1, pp. 7–13, 2007.
- [29] S. A. Burton, F. L. Frederickson, K. J. Hansen, R. P. Simmers, P. T. Fenn, C. S. Moeckly *et al.*, "Hollow microneedle array and method," Nov. 17 2009, uS Patent App. 13/128,066.
- [30] K. Yung, Y. Xu, C. Kang, H. Liu, K. Tam, S. Ko, F. Kwan, and T. M. Lee, "Sharp tipped plastic hollow microneedle array by microinjection moulding," *Journal of Micromechanics and Microengineering*, vol. 22, no. 1, p. 015016, 2012.
- [31] J. D. Williams and W. Wang, "Study on the postbaking process and the effects on uv lithography of high aspect ratio su-8 microstructures," *Journal of Micro/Nanolithography, MEMS, and MOEMS*, vol. 3, no. 4, pp. 563–568, 2004.
- [32] Y.-J. Chuang, F.-G. Tseng, and W.-K. Lin, "Reduction of diffraction effect of uv exposure on su-8 negative thick photoresist by air gap elimination," *Microsystem technologies*, vol. 8, no. 4-5, pp. 308–313, 2002.
- [33] P. Jin, K. C. Jiang, and N. Sun, "Microfabrication of ultra-thick su-8 photoresist for microengines," in *Micromachining and Microfabrication*. International Society for Optics and Photonics, 2003, pp. 105–110.

- [34] W. Wang and S. A. Soper, *Bio-MEMS: technologies and applications*. CRC Press, 2006.
- [35] J. D. Williams and W. Wang, "Using megasonic development of su-8 to yield ultra-high aspect ratio microstructures with uv lithography," *Microsystem technologies*, vol. 10, no. 10, pp. 694–698, 2004.
- [36] F. Ceyssens, B. P. Chaudhri, C. Van Hoof, and R. Puers, "Fabrication process for tall, sharp, hollow, high aspect ratio polymer microneedles on a platform," *Journal of Micromechanics and Microengineering*, vol. 23, no. 7, p. 075023, 2013.
- [37] R. J. Cox, J. D. Gelorme, and S. A. Gutierrez, "Photoresist composition and printed circuit boards and packages made therewith," Nov. 21 1989, uS Patent 4,882,245.
- [38] J. M. Shaw, J. D. Gelorme, N. C. LaBianca, W. E. Conley, and S. J. Holmes, "Negative photoresists for optical lithography," *IBM Journal of Research and Development*, vol. 41, no. 1.2, pp. 81–94, 1997.
- [39] A. Rashidian, D. Klymyshyn, M. T. Aligodarz, M. Boerner, and J. Mohr, "Su-8 resonator antenna," in *Antennas and Propagation Society International Symposium (APSURSI), 2010 IEEE*. IEEE, 2010, pp. 1–4.
- [40] S.-H. Cho, H. M. Lu, L. Cauller, M. I. Romero-Ortega, J.-B. Lee, and G. A. Hughes, "Biocompatible su-8-based microprobes for recording neural spike signals from regenerated peripheral nerve fibers," *Sensors Journal, IEEE*, vol. 8, no. 11, pp. 1830–1836, 2008.
- [41] K. V. Nemani, K. L. Moodie, J. B. Brennick, A. Su, and B. Gimi, "In vitro and in vivo evaluation of su-8 biocompatibility," *Materials Science and Engineering: C*, vol. 33, no. 7, pp. 4453–4459, 2013.
- [42] G. Voskerician, M. S. Shive, R. S. Shawgo, H. v. Recum, J. M. Anderson, M. J. Cima, and R. Langer, "Biocompatibility and biofouling of mems drug delivery devices," *Biomaterials*, vol. 24, no. 11, pp. 1959–1967, 2003.
- [43] Y. Cheng, H.-L. Tsai, K. Sugioka, and K. Midorikawa, "Fabrication of 3d microoptical lenses in photosensitive glass using femtosecond laser micromachining," *Applied Physics A*, vol. 85, no. 1, pp. 11–14, 2006.
- [44] C.-H. Lin, L. Jiang, Y. Chai, H. Xiao, S.-J. Chen, and H. Tsai, "Fabrication of microlens arrays in photosensitive glass by femtosecond laser direct writing," *Applied Physics A*, vol. 97, no. 4, pp. 751–757, 2009.
- [45] B. G. Johnston, "Column buckling theory: historic highlights," *Journal of Structural Engineering*, vol. 109, no. 9, pp. 2086–2096, 1983.

- [46] W. G. Smith, "Analytic solutions for tapered column buckling," *Computers & structures*, vol. 28, no. 5, pp. 677–681, 1988.
- [47] J. Ji, F. E. Tay, J. Miao, and C. Iliescu, "Microfabricated microneedle with porous tip for drug delivery," *Journal of Micromechanics and Microengineering*, vol. 16, no. 5, p. 958, 2006.
- [48] J. D. Zahn, N. H. Talbot, D. Liepmann, and A. P. Pisano, "Microfabricated polysilicon microneedles for minimally invasive biomedical devices," *Biomedical microdevices*, vol. 2, no. 4, pp. 295–303, 2000.
- [49] M. N. Abser, "Solid silicon microneedles for safe and effective drug delivery to human eye," *Journal of Electrical Engineering*, vol. 36, no. 2, pp. 28–34, 2011.
- [50] J. Ji, F. E. Tay, J. Miao, and C. Iliescu, "Microfabricated microneedle with porous tip for drug delivery," *Journal of Micromechanics and Microengineering*, vol. 16, no. 5, p. 958, 2006.
- [51] X. Kong, P. Zhou, and C. Wu, "Numerical simulation of microneedles' insertion into skin," *Computer Methods in Biomechanics and Biomedical Engineering*, vol. 14, no. 9, pp. 827–835, 2011.
- [52] R. Feng and R. J. Farris, "Influence of processing conditions on the thermal and mechanical properties of su8 negative photoresist coatings," *Journal of Micromechanics and Microengineering*, vol. 13, no. 1, p. 80, 2003.
- [53] B. Li, M. Liu, and Q. Chen, "Low-stress ultra-thick su-8 uv photolithography process for mems," *Journal of Micro/Nanolithography, MEMS, and MOEMS*, vol. 4, no. 4, pp. 043 008–043 008, 2005.
- [54] R. L. Norton, *Machine design: an integrated approach*. Pearson Prentice Hall New Jersey, 2006, vol. 3.
- [55] D. Bodhale, A. Nisar, and N. Afzulpurkar, "Design, fabrication and analysis of silicon microneedles for transdermal drug delivery applications," in *The Third International Conference on the Development of Biomedical Engineering in Vietnam*. Springer, 2010, pp. 84–89.
- [56] M. Ashraf, S. Tayyaba, A. Nisar, N. Afzulpurkar, D. Bodhale, T. Lomas, A. Poyai, and A. Tuantranont, "Design, fabrication and analysis of silicon hollow microneedles for transdermal drug delivery system for treatment of hemodynamic dysfunctions," *Cardiovascular Engineering*, vol. 10, no. 3, pp. 91–108, 2010.
- [57] Winkipedia, *Timoshenko Beam Theory*. [Online]. Available: http://en.wikipedia.org/wiki/Timoshenko_beam_theory

- [58] M. Han, D.-H. Hyun, H.-H. Park, S. S. Lee, C.-H. Kim, and C. Kim, "A novel fabrication process for out-of-plane microneedle sheets of biocompatible polymer," *Journal of micromechanics and microengineering*, vol. 17, no. 6, p. 1184, 2007.
- [59] M. Ramasubramanian, O. Barham, and V. Swaminathan, "Mechanics of a mosquito bite with applications to microneedle design," *Bioinspiration & biomimetics*, vol. 3, no. 4, p. 046001, 2008.
- [60] L. Du and Q. Wang, "Experimental study on ultrasonic stress relief for cured su-8 photoresist layer," *Microelectronic Engineering*, vol. 87, no. 12, pp. 2555–2560, 2010.
- [61] L. Du, Q. Wang, and X. Zhang, "Reduction of internal stress in su-8 photoresist layer by ultrasonic treatment," *Science China Technological Sciences*, vol. 53, no. 11, pp. 3006–3013, 2010.
- [62] Y.-K. Yoon, J.-H. Park, F. Cros, and M. G. Allen, "Integrated vertical screen microfilter system using inclined su-8 structures," in *Micro Electro Mechanical Systems, 2003. MEMS-03 Kyoto. IEEE The Sixteenth Annual International Conference on.* IEEE, 2003, pp. 227–230.
- [63] M. Han, W. Lee, S.-K. Lee, and S. S. Lee, "3d microfabrication with inclined/rotated uv lithography," *Sensors and Actuators A: Physical*, vol. 111, no. 1, pp. 14–20, 2004.
- [64] K.-Y. Hung, H.-T. Hu, and F.-G. Tseng, "Application of 3d glycerol-compensated inclined-exposure technology to an integrated optical pick-up head," *Journal of Micromechanics and Microengineering*, vol. 14, no. 7, p. 975, 2004.
- [65] S. K. Mitra and S. Chakraborty, *Microfluidics and Nanofluidics Handbook: fabrication, implementation, and applications.* CRC Press, 2011, vol. 2.
- [66] Z.-g. Ling and K. Lian, "New fabrication techniques of su-8 fiber holder with cantilever-type elastic microclips by inclined uv lithography in water using single mylar mask," *Microsystem technologies*, vol. 16, no. 3, pp. 405–410, 2010.
- [67] H. Sato, D. Yagyu, S. Ito, and S. Shoji, "Improved inclined multi-lithography using water as exposure medium and its 3d mixing microchannel application," *Sensors and Actuators A: Physical*, vol. 128, no. 1, pp. 183–190, 2006.
- [68] F.-G. Tseng and H.-T. Hu, "A novel micro optical system employing inclined polymer mirrors and fresnel lens for monolithic integration of optical disk pickup heads," in *TRANSDUCERS, Solid-State Sensors, Actuators and Microsystems, 12th International Conference on, 2003*, vol. 1. IEEE, 2003, pp. 599–602.

- [69] Y.-J. Chuang, F.-G. Tseng, and W.-K. Lin, "Reduction of diffraction effect of uv exposure on su-8 negative thick photoresist by air gap elimination," *Microsystem technologies*, vol. 8, no. 4-5, pp. 308–313, 2002.
- [70] J. Wallach and L. Gibson, "Mechanical behavior of a three-dimensional truss material," *International Journal of Solids and Structures*, vol. 38, no. 40, pp. 7181–7196, 2001.
- [71] J. Kim, D. Cho, and R. S. Muller, "Why is (111) silicon a better mechanical material for mems," *Proc. Transducers 2001*, pp. 662–665, 2001.
- [72] P. R. Besser, "Method to control mechanical stress of copper interconnect line using post-plating copper anneal," Apr. 9 2002, uS Patent 6,368,967.
- [73] E. H. Conradie and D. F. Moore, "Su-8 thick photoresist processing as a functional material for mems applications," *Journal of Micromechanics and Microengineering*, vol. 12, no. 4, p. 368, 2002.
- [74] S. F. Edwards, P. Maier, and J. Shultz-Harder, "Direct bonded heat spreader," Jul. 22 1997, uS Patent 5,650,662.
- [75] Y. Lee, H. Kuo, C. Lee, T. Lu, S. Wang, and S. Chiou, "High-temperature stability of 650-nm resonant-cavity light-emitting diodes fabricated using wafer-bonding technique on silicon substrates," *Photonics Technology Letters, IEEE*, vol. 19, no. 14, pp. 1060–1062, 2007.
- [76] C.-H. Lin, G.-B. Lee, B.-W. Chang, and G.-L. Chang, "A new fabrication process for ultra-thick microfluidic microstructures utilizing su-8 photoresist," *Journal of Micromechanics and Microengineering*, vol. 12, no. 5, p. 590, 2002.
- [77] R. Feng and R. J. Farris, "Influence of processing conditions on the thermal and mechanical properties of su8 negative photoresist coatings," *Journal of Micromechanics and Microengineering*, vol. 13, no. 1, p. 80, 2003.
- [78] F. Blanco, M. Agirregabiria, J. Garcia, J. Berganzo, M. Tijero, M. Arroyo, J. Ruano, I. Aramburu, and K. Mayora, "Novel three-dimensional embedded su-8 microchannels fabricated using a low temperature full wafer adhesive bonding," *Journal of Micromechanics and Microengineering*, vol. 14, no. 7, p. 1047, 2004.
- [79] P.-C. Wang, S.-J. Paik, S. Chen, S. Rajaraman, S.-H. Kim, and M. G. Allen, "Fabrication and characterization of polymer hollow microneedle array using uv lithography into micromolds," 2013.
- [80] N. C. Lindquist, P. Nagpal, K. M. McPeak, D. J. Norris, and S.-H. Oh, "Engineering metallic nanostructures for plasmonics and nanophotonics," *Reports on Progress in Physics. Physical Society (Great Britain)*, vol. 75, no. 3, p. 036501, 2012.

-
- [81] N. C. Lindquist, T. W. Johnson, P. Nagpal, D. J. Norris, and S.-H. Oh, “Plasmonic nanofocusing with a metallic pyramid and an integrated c-shaped aperture,” *Scientific reports*, vol. 3, 2013.
- [82] A. Rammohan, P. K. Dwivedi, R. Martinez-Duarte, H. Katepalli, M. J. Madou, and A. Sharma, “One-step maskless grayscale lithography for the fabrication of 3-dimensional structures in su-8,” *Sensors and Actuators B: Chemical*, vol. 153, no. 1, pp. 125–134, 2011.
- [83] J.-J. Yang, Y.-S. Liao, and C.-F. Chen, “Fabrication of long hexagonal micro-lens array by applying gray-scale lithography in micro-replication process,” *Optics communications*, vol. 270, no. 2, pp. 433–440, 2007.

Publications

Publications enclosed in this thesis

P1: **Hoa Le Thanh**, Hai Le The, Nhut Tran-Minh, Vy Nguyen, Frank Karlsen, "Optimal design and fabrication of polymer-based microneedle for safe collection of whole blood", submitted to Special Issue for Micro and Nano Letters, May 2014.

P2: **Hoa Le-Thanh**, Nhut Tran-Minh, Hai Le The, Frank Karlsen, "A Novel Design of Hollow Microneedle for Blood Extraction", in Proc. of IEEE-International Conference on Nano/Micro Engineered and Molecular Systems, pp. 430-435, April 2014.

P3: **Hoa Le-Thanh**, Nhut Tran-Minh, Hai Le The, Frank Karlsen, "A Study on Mechanical Strength of Pyramid-Shaped Microneedle", in Proc. of IEEE-Middle East Conference on Biomedical Engineering, pp. 29-32, February 2014.

Publications not enclosed in this thesis

P4: Hai Le The, **Hoa Le Thanh**, Nhut Tran-Minh, and Frank Karlsen, "Optimal design of an effective passive micromixer with shifted trapezoidal blades using wide Reynolds number range", accepted by Journal of Micromechanics and Microengineering May 2014.

P5: Hai Le The, Nhut Tran-Minh, **Hoa Le-Thanh**, Frank Karlsen, "A Novel Micromixer with Multimixing Mechanisms for High Mixing Efficiency at Low Reynolds Number", in Proc. of IEEE-International Conference on Nano/Micro Engineered and Molecular Systems, pp. 651-654, April 2014.

P6: Hai Le The, Nhut Tran-Minh, **Hoa Le-Thanh**, Frank Karlsen, "A Novel Passive Micromixer with Trapezoidal Blades for High Mixing Efficiency at Low Reynolds Number Flow", in Proc. of IEEE-Middle East Conference on Biomedical Engineering, pp. 25-28, February 2014.

P7: Nhut Tran-Minh, **Hoa Le-Thanh**, Frank Karlsen, "Analytical and Numerical Approaches for Optimization Design of MEMS Based SU-8 Microneedles", ACBIT2013, Japan. To be published in: Computer Methods and Programs in Biomedicine.

Publication P1:

P1: **Hoa Le Thanh**, Hai Le The, Nhut Tran-Minh, Vy Nguyen, Frank Karlsen, "Optimal design and fabrication of polymer-based microneedle for safe collection of whole blood", submitted to Special Issue for Micro and Nano Letters, May 2014.

Optimal design of the polymer-based microneedle for improved collection of whole blood from human fingers

Hoa Le Thanh, Hai Le The, Nhut Tran-Minh, Vy Nguyen, Kaiying Wang and Frank Karlsen

Department of Micro and Nano Systems Technology (IMST), Buskerud and Vestfold University College, Postboks 235, 3603 Kongsberg, Norway.
E-mail: thanhhoa.hcmut@gmail.com

In this paper, a highly applicable theoretical model and a simple, inexpensive mold-based method was introduced to design and fabricate the pyramid-shaped SU-8 microneedle. The main purpose was to be able to extract blood at point-of-care sites from up to 80% of typical nurse-home patients with a disorder of blood circulation in the fingers and toes (Raynaud's phenomenon). Geometry optimization was conducted based on the study of fracture force which can be accurately predicted by the proposed theoretical model. The accuracy of the proposed theoretical model was confirmed by the finite element study and practical measurement. For practical verification, measurement of fracture force was conducted on fabricated SU-8 microneedles, including: 1470 μm -tall pyramid-shaped microneedle and 1515 μm -tall traditional-shaped microneedle. The measurement results confirmed the improved strength of the proposed pyramid-shaped microneedle, especially of the pyramidal tips which can exhibit significantly higher applied force with 2.82N compared to 0.51N of bevel tip. The practical tests of skin penetrability on human fingers showed that the microneedles fabricated with the proposed geometry may be sharp and strong enough to safely puncture the human skin and long enough to reach the blood vessels.

1. Introduction: Early diagnostic and pre-disease detection are extremely important to increase patient survival rates. Accuracy and reliability is highly desirable for adequate selection of suitable therapeutics. The project of POCNAD has been done in order to develop a platform for rapid screening or diagnosis clinical or environmental variations that is related-gene activity. The platform is desired to operate with seven main functions of patient sample collection, concentration/separation, pre-treatment, preparation, purification, amplification and target detection. For blood-sampling device, hypodermic needles are traditionally utilized in every health care system for direct collection from blood veins. However, with numbers of downsides, such as: insertion pain, tissue trauma [1], patient discomfort or needle phobia [2], lack of convenience and user-friendly ability [3], the requirement of expertise and specialized medical knowledge for implementation [4], the utilization of hypodermic needles has been replaced by a new approach of Sample Collection Related (SCR) micro-scale needles i.e. microneedles. Especially for patients who need periodic and continuous monitoring, e.g. diabetic patients [5]. The first main purpose of SCR micro needle arrays is to make human blood available in any health station, nurse homes or family homes. The second main purpose is to make it possible to extract blood from a typical point-of-care setting including patients or old people with very low blood circulation. The main challenge for the health personal with low blood circulation or a disorder blood circulation (Raynaud's phenomenon) or reduced systolic pressures in the fingers is the challenge including conventional needles to get out any whole blood sample.

During practical implementation of microneedles, brokenness of microneedle, particularly tip fracture, is one of the most crucial issues. Broken part may remain inside the human skin or enter the blood vessels, causing injury, inflammation or abrasion. Therefore, geometry optimization is highly desirable, especially with blood-sampling microneedle (length must be longer than 1500 μm [6]). One frequently-used approach is to minimize the failure possibility to ensure as high safety as possible. Previously, numbers of studies on mechanical failure have been conducted with either mathematical or simulation models [7-10]. The failure criteria of yield strength and shear strength may provide better accuracy for the prediction of fracture force [11].

In this study, we propose a stronger design of pyramid-shaped microneedle (PMNs) that may exhibit safer skin penetration. The improved mechanical strength of PMNs was verified by the comparison of fracture force with traditional-shaped microneedle (TMNs). Then, the geometry optimization was conducted based on the proposed pyramid-shaped microneedle. The accuracy and reliability of the fracture analysis of the proposed pyramid-shaped hollow microneedles was verified by finite element method with COMSOL and practical measurements. To fabricate high-aspect-ratio hollow microneedles, we utilized mold-based method in [12]. According to this method, conventional SU-8 lithography and PDMS micromolds are combined to develop a low-cost, simple method with good repeatability and high throughput. Skin penetrability our proposed pyramid-shaped hollow microneedle is also tested by inserting a single/array of pyramid-shaped microneedle into the human fingers to evaluate the practical performance of the fabricated PMNs in many aspects, such as: mechanical failures, skin penetrability and extraction ability.

2. Geometry optimization by structural analysis: PMNs are expected to improve the mechanical performance (i.e. larger force endurance) with the special features of the square base, off-center lumen and pyramidal tip. The structural strength of PMNs was studied through the investigation of fracture forces, including critical buckling load (P_{cr}) and maximum bending force (P_b). The dimension of each geometrical feature can also be optimized with the study on fracture forces.

2.1 Analytical and numerical solutions: The first failure mechanism to be considered is structural buckling. To calculate critical buckling load (P_{cr}), (1) was utilized. This formula has been used in numbers of studies to compute P_{cr} of varied cross-section structures, such as tapered hollow microneedles [8] and square pyramid column [11]. In our previous work [13], this approach was applied particularly for PMNs. In this letter, (1) was utilized to estimate P_{cr} of two different designs of microneedles: PMNs and TMNs.

$$P_{cr} = \frac{E\pi^2}{2L^3} \int_0^L \sum_{i=0}^n I(z) \cdot \cos^2\left(\frac{\pi z}{2L}\right) dz \quad (1)$$

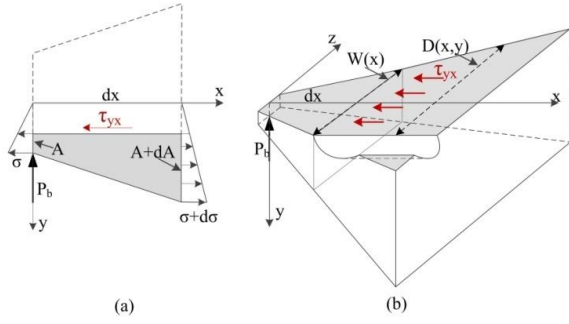


Fig. 1 Illustrations for shear stress derivation. σ and $\sigma+d\sigma$ are normal stress distributed on the area A and $A+dA$. τ_{yx} is assumed to be uniform in z -direction. P_b represents for the distributed bending force acting on y -direction.

a Stress balance in xOy plane

b Distribution of shear stress (τ_{yx}) in pyramidal tip

The second failure mechanism is due to transverse force, i.e. bending force. Typically, bending force is most likely to induce fracture at the microneedle shaft at which is subjected to the largest bending moment. However, microneedle tips are considerably breakable due to diminutive tip-size ($\sim 40\mu\text{m}$). The possibility of tip failure may be subsequently higher than that of shaft failure. In this paper, we developed a theoretical model to compute the magnitude of shear stress when the microneedle is subjected to a distributed bending force. With higher applicability to various structural designs, this model may predict more accurately the fracture bending force. As illustrated in Fig. 1a, the equation of stress balance in x -direction is presented in (2).

$$\int_A \sigma dA + \tau_{yx} A_{xy} = \int_{A+dA} (\sigma + d\sigma) dA \quad (2)$$

$$\Rightarrow \int_A \sigma dA + \tau_{yx} D(x, y) dx = \int_{A+dA} (\sigma + d\sigma) dA \quad (3)$$

$$\Rightarrow \left(\frac{M(x)}{I_z(x)} + d \left(\frac{M(x)}{I_z(x)} \right) \right) \int_{A+dA} y dA - \frac{M(x)}{I_z(x)} \int_A y dA = \tau_{yx} D(x, y) dx \quad (4)$$

The integrals in (4) is observed to be the expression for the first moment of area $Q_z(x, y)$. Consequently, (4) becomes:

$$\Rightarrow \left(\frac{M(x)}{I_z(x)} + d \left(\frac{M(x)}{I_z(x)} \right) \right) (Q_z - dQ_z) - \frac{M(x)}{I_z(x)} Q_z = \tau_{yx} D(x, y) dx \quad (5)$$

Equation (5) can be simplified by neglecting high-order components. Thus, the final expression of shear stress (τ_{xy}) can be deduced as follows:

$$\tau_{xy} = \tau_{yx} = \frac{1}{D(x, y)} \left(\frac{M(x)}{I_z(x)} \frac{dQ_z}{dx} + Q_z \frac{d}{dx} \left(\frac{M(x)}{I_z(x)} \right) \right) \quad (6)$$

where $D(x, y)$ is the applying width of shear stress, $Q_z(x, y)$ and $I_z(x)$ is the first and second moment of area, $M(x)$ is the bending moment resulted from the distributed bending force P_b . All components are illustrated in Fig. 1b.

For PMNs, the components in (6) were computed for five different cross sectional areas corresponding to five regions of x . The calculations were conducted by programming with Maple software. The theoretical results were then verified by COMSOL simulator under the same boundary conditions. Specifically, the whole structural parameters were variable except the bottom is set to be fixed constraint. A distributed force $P_b = 0.105\text{N}$ is applied on the shaded area in Fig. 2a with $X_0 = 152\mu\text{m}$. The values of shear stress can be

extracted from the stress tensor. Distribution of τ_{xy} is presented in x - y coordinates, and it is assumed to be uniform in z -direction and symmetrical on y -axis.

2.2 Analytical analysis results and numerical simulation results: Fig. 2 shows the matching of shear stress between analysis results and simulation results. There are two critical points, 1st MAX (global maximum at X_0) and 2nd MAX (local maximum at diminutive edge) (see Fig. 2), at which fracture is most likely to happen. A good matching between analysis results and simulation results can be observed in Fig. 2, 3. The standard deviation is about 6.5% and 25.4% for the 1st and 2nd MAX point, respectively. Since the concentrated stress is distributed in a diminutive edge at 2nd MAX point, the magnitude of τ_{yx} is significantly increased. In practice, the fabricated microneedle will not exhibit this problem because the fabrication of extremely sharp features is very challenging in practice. However, the prediction of τ_{yx} at 2nd MAX helps to verify the accuracy of our proposed model. Fig. 3b depicts how τ_{yx} at 1st MAX point reduces with an increase in X_0 . Also, the tip failure is most likely to occur before shaft failure. By comparing $(\tau_{yx})_{\text{max}}$ to the shear strength of SU-8 (19.5MPa), P_b can be deduced.

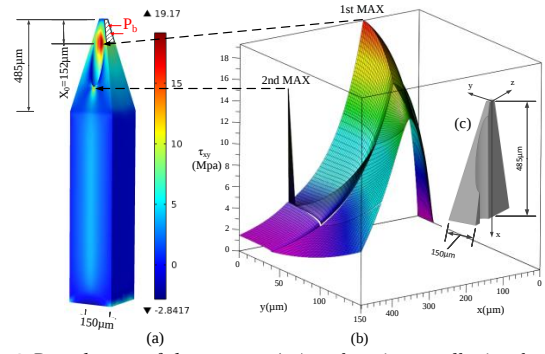


Fig. 2 Distribution of shear stress (τ_{xy}) at the microneedle tip when P_b is applied in the shaded area ($X_0=152\mu\text{m}$)

a 3D distribution from simulation results

b 3D distribution from theoretical calculation

c Illustration for system coordinates on a half of pyramidal tip

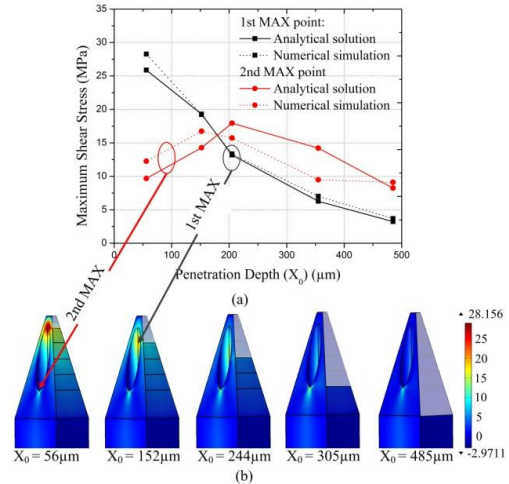


Fig. 3 Matching of the results from simulation and calculation results

a 2D plot of the matching of τ_{xy} magnitude at 1st and 2nd MAX point

b 3D distribution of τ_{xy} from simulation with $X_0: 56\mu\text{m} - 485\mu\text{m}$

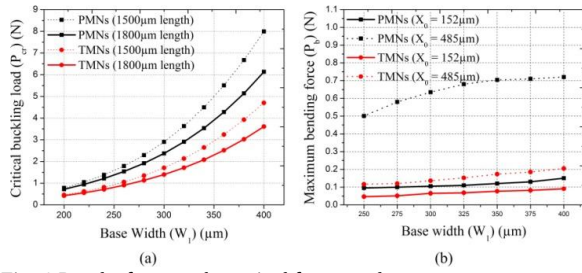


Fig. 4 Results from mathematical frameworks

a Critical buckling load (P_{cr}) versus base width (W_1)

b Maximum bending force (P_b) versus base width (W_1)

The relationship between P_{cr} and base width (W_1) was investigated with W_1 ranges from 200μm to 400μm. The effect of length (L) was also taken into account with two values of L : 1800μm and 1500μm. The results are shown in Fig. 4. The endurance of PMNs against axial force is about 1.7 times higher than that of TMNs, verifying the improved strength of PMNs. In Fig. 6b, we can see that the possibility of tip brokenness is significantly high when $X_0 = 152\mu\text{m}$ (i.e. the puncturing point of microneedle into human skin). When $W_1 = 300\mu\text{m}$, $L = 1500\mu\text{m}$, the proposed PMNs can withstand 2.94N (axial force) and 0.105N (bending force at $X_0 = 152\mu\text{m}$) compared to 1.71N (axial force) and 0.065N (bending force at $X_0 = 152\mu\text{m}$) of TMNs. The theoretical results show that the pyramidal tip may be stronger than bevel tip in terms of bending force resistance.

With the same procedure as presented, this model can be applied for other structures, such as: traditional-shaped microneedle, tapered-tip microneedle or truncated cone microneedle, for more accurate prediction of fracture bending force.

3. Fabrication of microneedles: To develop an inexpensive method with high throughput for fabrication of microneedle, two mold-based methods with SU-8 epoxy photoresist (MicroChem, Newton, MA) were proposed and compared (see Fig. 6). Fig. 6a, b presents the procedure to construct the pyramidal tips by using 4-time inclined exposure. The top part is relatively rotated 90° at each time of exposure. The actual tip angle will be reduced due to the effect of light refraction ($n_{\text{air}} = 1$, $n_{\text{SU-8}} = 1.668$ [14]). Therefore, a tip angle of 25° is achievable with a 35-degree-angle aluminum holder.

Fig. 6c presents the concept of two fabrication methods, including: method 1 (molding of microneedles) and method 2 (direct formation of microneedles). The difference between two methods is at step 2-4 in Fig. 6c. At step 1 in Fig. 6c, SU-8 coating was performed by using weight-controlled method i.e. the thickness of coated layer is controlled by weighting SU-8 2150 ($\rho = 1.19 \text{ kg/m}^3$) before pouring to the substrate. 600μm-thick and 1100μm-thick SU-8 layers are achievable with 3.3g and 5.8g SU-8 2150, respectively. The sample was soft-baked for 15 minutes at 65°C and 4 hours at 95°C followed by 4-time inclined exposure with the exposure dosage of 700mJ/cm² for each time of exposing. The 500μm-tall pyramidal tips were obtained after 10-minute development. With the process on silicon wafer, wafer bending is a serious issue, which subsequently may lead to misalignment, poor adhesion and cracks. We proposed a solution, named "separated line", to reduce the effect of internal stress in multilayer structures of thick SU-8 film, which subsequently may cause wafer bending [15]. Separated lines are patterned on a photomask to separate and reduce the stress applying

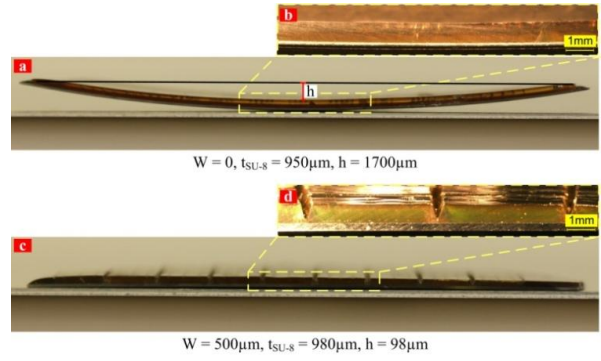


Fig. 5 Bending problem and the solution of separated lines

a, b 950μm-thick SU-8 layer, $W = 0$, $h = 1700\mu\text{m}$

c, d 980μm-thick SU-8 layer, $W = 500\mu\text{m}$, $h = 98\mu\text{m}$

area (see Fig. 5c, d), thus provide more space for SU-8 to expand/compress upon heating/cooling. The optimal width of separated line (W) was numerically and experimentally studied to be 500μm. A test on 3-inch silicon wafer was conducted to examine the advantage of separated line. The wafer bending reduced significantly from 1700μm (see Fig. 5a) to 98μm (see Fig. 5c) for the cases of without separated lines and with 500μm-wide separated lines, respectively.

In method 2 is firstly considered. At step 2.2, primary PMDS mold with pyramidal tips were constructed by performing inverse molding two times. A 1000μm-thick SU-8 layer was then coated on the PDMS mold. The sample was soft-baked for 15 minutes at 65°C and 10 hours at 95°C. Double exposure step was then conducted with the exposure dosage of 3000mJ/cm² and 300mJ/cm² to form the microneedle shaft and the support plate, respectively. The hollow microneedle array was obtained after 30-minute development with ultrasonic agitation followed by gentle separation. On the other hand, in method 1, after the pyramidal tips were constructed, a master mold of microneedle-shaped holes was obtained after exposure (step 2.1). The primary PDMS mold was created by performing inverse PDMS molding twice (see step 3.1 in Fig. 6c).

Our experiments indicate that method 2 is relatively better than method 1 in terms of the quality of fabricated microneedle tips, repeatability, fabrication time, and cost. At step 3.1 in Fig. 6c, when performing PDMS molding/unmolding, the high-aspect-ratio structures were easily broken, subsequently leads to the imperfection or destruction of the final molded microneedles. In addition, the possibility of successfully fabricating microneedle hollows in method 2 is higher than that of method 1. The effect of light scattering is more critical at step 4.1 in Fig. 6c because of the large opening area (80μm diameter of patterned feature). In method 2, microneedle separation is easier.

For the fabrication of TMNs, we utilized method 2. The bevel tip was created on a 25° sloped wall. The microneedle shaft, hollow, and the support plate were formed by double exposure. TMNs were obtained after SU-8 development and separation. PMNs were fabricated with 1470μm in total length (490μm tip and 980μm shaft), 310μm in base width, 80μm in hollow diameter, tip-size of 43μm, and 210μm - 330μm thick in support plate. TMNs were fabricated with 1515μm in total length (627μm tip and 888μm shaft), 314μm in base width, 80μm in hollow diameter, tip-size of 39μm, and 200μm thick in support plate.

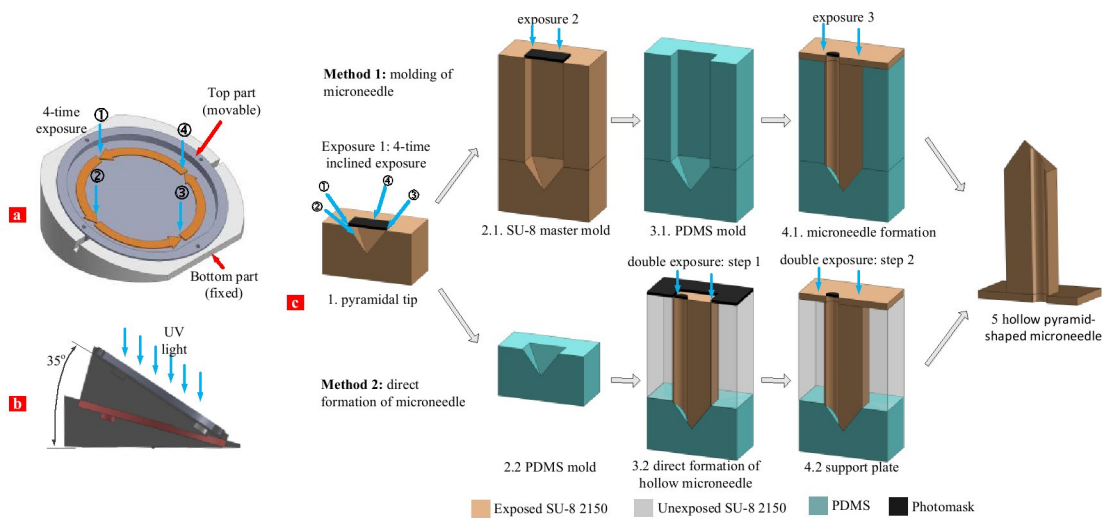


Fig. 6 Illustrations for fabrication of polymer-based hollow microneedles.

- a Principle of the inclined exposure. The top part is movable and can be rotated 90 degree relative to the bottom part. The sample was exposed four times to form the pyramidal structure
- b Illustration for the inclined exposure with the aluminum holder
- c Process flow of two methods for the fabrication of microneedles, the figures are shown in cross-sectional view

4. Performance evaluation:

4.1 Measurement of fracture force: The measurement setup on Shear Tester Delvotec 5600 is shown in Fig. 7. The microneedle is mounted on the force driving tip. The movement is precisely controlled by a built-in motor with the resolution of 0.01N. To measure the fracture force, a rigid surface (1mm-thick aluminum plate with 69GPa in Young's modulus) was used as a penetration object. To minimize the effect of slippery, a thin layer of epoxy resin UN3082 was spun on aluminum plate. This layer provides a softer surface to immobilize the microneedle tip. Thus, the measurement error due to slippery can be minimized. The measurements were conducted repeatedly three times each for PMNs and TMNs.

Force-time plot was recorded and displayed on the screen as shown in Fig. 8. Failure point was determined automatically by the system when there is a sudden decrease of applied force. There are two points at which the microneedles were broken corresponding to tip failure and shaft failure. PMNs exhibited higher fracture forces (2.74N for tip failure and 3.45N for shaft failure) compared to TMNs (0.46N for tip failure and 2.32N for shaft failure).

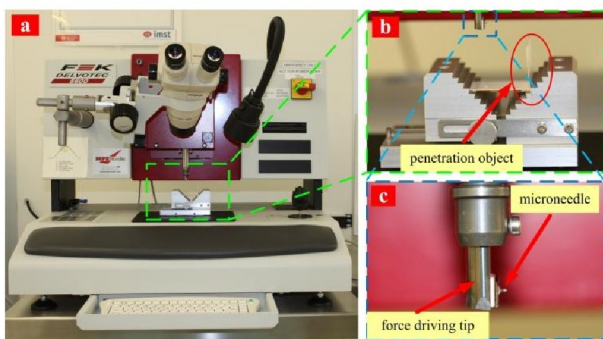


Fig. 7 Photo of testing instrument for measurement of fracture force
 a Equipment setup on Shear Tester Delvotec 5600
 b Microneedle and penetration object (aluminum plate)
 c Microneedle is mounted on the force driving tip

The average measured forces are presented in Table 1. In comparison with the results from theoretical study, the average differences in percentage are 8.16% and 29.5% for PMNs and TMNs, respectively. When the microneedle tip is broken, the total length is reduced. Fracture force thus increased. With average tip-fracture force of 2.82N, pyramidal tip may be stronger than bevel tip which only can withstand to the maximum force of 0.51N.

Table 1: The measured results of fracture axial force

Type of MNs	Measured force (N)				Calculated force (shaft failure) (N)	Difference (shaft failure) (%)
	Shaft failure	$\bar{\sigma}$ (%)	Tip failure	$\bar{\sigma}$ (%)		
PMNs	3.4	1.8	2.82	2.0	3.2	8.16
TMNs	2.37	2.1	0.51	7.8	1.7	29.5

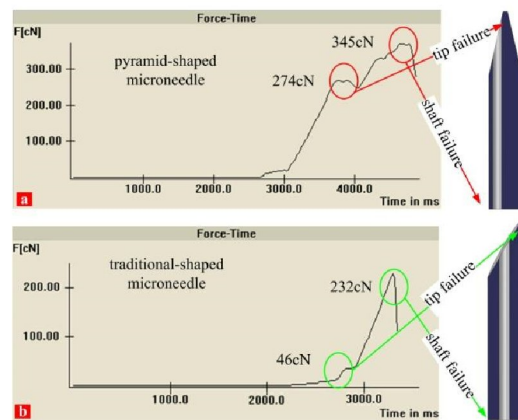


Fig. 8 Measurement results of fracture force of PMNs and TMNs. The forces were recorded as a function of applying time.
 a Force-time measurement plot of PMNs
 b Force-time measurement plot of TMNs

4.2 Skin penetrability: Skin penetrability of the fabricated microneedles was assessed on volunteers' fingers, as shown in Fig. 8. Two scenarios were conducted on human fingers for a single microneedle and a 3x3 microneedle array. The microneedles were pressed perpendicularly against the human finger by manually pushing then pulled out by metallic tweezers. The insertion process was optically inspected under the microscope Olympus MVX10 as depicted in Fig. 9.

In scenario 1, the single PMNs were safely inserted into human skin. The fabricated microneedles showed to be able to penetrate the skin barrier without breaking. Tip brokenness was not observed when separating the microneedles from human finger. Fig. 9a, b show an inserted PMNs and the insertion spot at which the presence of blood was observed. In scenario 2, an array of PMNs was successfully punctured human finger. According to the testing results, the fabricated PMNs (42x42µm tip) were able to insert safely into human skin with the configuration of microneedle array. Specifically, it is easier to perform vertical insertion on 3x3 array than a single microneedle. Moreover, the pre-positioned microneedles on the array made it possible for vertical insertion. The array fabricated with 1500µm and 2000µm microneedle pitch was experimentally proved to be potentially penetrable into human skin compared to the array with 1200µm pitch. To avoid brokenness of the support plate, the thickness of the support plate can be controlled by adjusting the exposure dosage at step 4.2 in Fig. 6c. The optimal thickness was experimentally chosen to be thicker than 300µm. Fig. 9c, d illustrate a successful skin penetration of fabricated microneedles array with 330µm-thick support plate (300mJ/cm²).

After separation of single microneedle and array of microneedles, at the insertion spots, as depicted in red circles in Fig. 9b, d, blood came out. The appearance of blood implies that the microneedles may be able to reach the blood vessels. Moreover, it also gives the preliminary results for further development of microneedle-based blood-sampling devices.

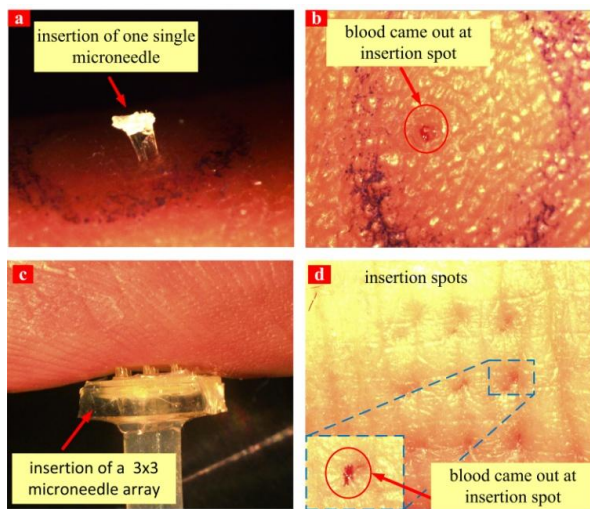


Fig. 9 Skin penetrability was tested on volunteer's finger with one single PMNs and a 3x3 array of PMNs. After insertion, insertion spots can be inspected on the volunteer's finger.

- a Inserted single PMNs into human finger
- b Insertion spot of single PMNs on human finger
- c Inserted PMNs array into human finger
- d Insertion spot of 3x3 array of PMNs on human finger

5. Conclusion: This paper proposed an optimal design of the pyramid-shaped microneedle for whole blood collection. The geometry of the proposed microneedle is optimized to minimize the possibility of brokenness. A mathematical model was introduced to predict the fracture bending force based on shear strength criterion with the verifications of simulation and measurement on fracture force. The proposed method of direct formation of microneedles experimentally showed to be potentially feasible for mass-production. In addition, the concept of method 2 opens a new path to develop an inexpensive method that suitable for mass-production. We suggest constructing an aluminum-based sample with pre-defined structures for a replacement of pyramidal tips (PMNs), sloped walls (TMNs). This aluminum sample can be fabricated with a conventional CNC machine. An adequate testing protocol is necessary for more accurate biological evidences. Further testing have to done in order to prove whether these microneedles are more useful for collection of whole blood from fingers with reduced systolic blood pressure.

6. Acknowledgments: This work was conducted at Buskerud and Vestfold University College with the support from two companies: Norchir and ORP.

7. References:

- [1] McAllister, D. V., Allen, M. G., Prausnitz, M. R. : 'Microfabricated microneedles for gene and drug delivery', Annual Review of Biomedical Engineering, 2002, 2, (1), pp. 289-313.
- [2] Hamilton, J. G. : 'Needle phobia: a neglected diagnosis', The Journal of family practice, 1995.
- [3] Prausnitz, M. R., : 'Analysis: Overcoming skin's barrier: The search for effective and user-friendly drug delivery', Diabetes technology & therapeutics, 2001, 3, (2), pp. 233-236.
- [4] Zhang, P., Dalton, C., Jullien, G. A., : 'Design and fabrication of mems-based microneedle arrays for medical applications', Microsystem technologies, 2009, 15, (7), pp. 1073-1082.
- [5] Mukerjee, E., Collins, S., Isseroff, R., and Smith, R., : 'Microneedle array for transdermal biological fluid extraction and in situ analysis', Sensors and Actuators A: Physical, 2004, 114, (2), pp. 267-275.
- [6] Li, C. G., Lee, C. Y., Lee, K., and Jung, H. : 'An optimized hollow microneedle for minimally invasive blood extraction', Biomedical microdevices, 2013, 15, (1), pp. 17-25.
- [7] Kuo, S.C, Chou, Y., : 'A Novel Polymer Microneedle Arrays and PDMS Micromolding', Tamkang Journal of Science and Engineering, 2004, 7, pp. 95-98.
- [8] Kim, K., Park D. S., Lu, H. M., Che, W., Kim, K., Lee, J.B., Ahn, C.H., : 'A tapered hollow metallic microneedle array using backside exposure of SU-8', Journal of Micromechanics and Microengineering, Apr. 2004, 14, (4), pp. 597-603.
- [9] Zahn, J., Talbot, N., Liepmann, D., Pisano, A., : 'Microfabricated Polysilicon Microneedles for Minimally Invasive Biomedical Devices', Biomedical Microdevices, 2000, 2, pp. 295-303.
- [10] Tsuchiya, K., Nakanishi, N., Nakamachi, E., : 'Development of blood extraction system designed by female mosquito's blood sampling mechanism for bio-MEMS', Biomedical Applications of Micro- and Nanoengineering, 2005, 5651, pp. 379-388.

- [11] Ji, J., Tay, F. E., Miao, J., Iliescu, C. : 'Microfabricated microneedle with porous tip for drug delivery', *Journal of Micromechanics and Microengineering*, 2006, **16**, (5), 958.
- [12] Luttge, R., Berenschot, E. J., de Boer, M. J., Altpeter, D. M., Vrouwe, E. X., van den Berg, A., Elwenspoek, M. : 'Integrated lithographic molding for microneedle-based devices', *Journal of Microelectromechanical Systems*, 2007, **16**, (4), pp. 872-884.
- [13] Hoa Le-Thanh, Nhut Tran-Minh, Hai Le The, Frank Karlsen, : 'A Novel Design of Hollow Microneedle for Blood Extraction', *IEEE-International Conference on Nano/Micro Engineered and Molecular Systems*, 2014, pp. 430-435.
- [14] Mitra, S. K., Chakraborty, S., : 'Microfluidics and Nanofluidics Handbook: fabrication, implementation, and applications', CRC Press, 2011, 2.
- [15] Li, B., Liu, M., Chen, Q., : 'Low-stress ultra-thick SU-8 UV photolithography process for MEMS', *Journal of Micro/Nanolithography, MEMS, and MOEMS*, 2005, **4**, (4), pp. 043008-043008.

Publication P2:

P2: **Hoa Le-Thanh**, Nhut Tran-Minh, Hai Le The, Frank Karlsen, "A Novel Design of Hollow Microneedle for Blood Extraction", in Proc. of IEEE-International Conference on Nano/Micro Engineered and Molecular Systems, pp. 430-435, April 2014.

A Novel Design of Hollow Microneedle for Blood Sample Collection

Hoa Le-Thanh, Nhut Tran-Minh, Hai Le The, Frank Karlsen

Abstract— In this study, a novel design of microneedle is proposed based on structural and fluidic analysis. For blood collection applications, a hollow microneedle is designed with optimal features. The features and size of this microneedle provide improved structural strength for optimal skin penetration. Mechanical evaluations are studied with intensive calculations of maximum allowance axial and transverse forces, followed by numerical simulation of the insertion process. In addition, the fluid behavior is also investigated. The dual diameter design of the hollow part was shown to maximize the extraction efficiency and minimize the clogging problem for high-volume collection of blood. Our study proposes a design guideline on making a high-performance microneedle for blood collection.

Keywords—hollow microneedle; mechanical failures, structural analysis; fluidic analysis, shear rate, blood clogging

I. INTRODUCTION

In clinical point of view, a user friendly, representative and point-of-care related sampling of biological components is an important initial process for diagnostic and treatment. The traditional sampling process is normally conducted at hospitals with hypodermic needles and cannot be done without educated personal. However, they are associated with some issues like pain, discomfort, possible failure, complications, and invasiveness due to large structural geometry. With metallic needles, biocompatibility is also a critical problem that needs to be considered.

One of promising alternatives would be the fabricated microneedles. In order to reach the blood vessels in the upper dermis, microneedles have to be fabricated in millimeter-scale length ($\sim 1500\mu\text{m}$) with addition desired features such as: sharp tip, small contact area, biocompatible material, etc. But the problem of mechanical failures then becomes more critical with an increasing aspect ratio. In relation to mechanical failure, numbers of studies have been conducted with either mathematical or simulation models [1-5]. The solutions have been given for typical geometries of microneedles such as: traditional-shaped, truncated cone, and tapered microneedles. However, a full picture of designing guidelines has not been provided since these models are applied for microneedles with intermediate length and simple structures.

The motivation of this study is to propose a new design of microneedle with better mechanical strength and collection efficiency for invasive blood collection. Potential failures of high microneedles will be investigated in terms of critical buckling load and maximum bending force. An analytical solution for our proposed microneedle will be derived in detail without any geometrical assumptions. The performance of microneedles will be tested with various parameter settings before achieving proper design specifications.

The rest of this paper is organized as follows. Section II briefly describes our proposed microneedle and its special features. Section III presents the underlying theory. Section IV demonstrates the hypothesis mentioned in Section II. Section V discusses the results and introduces an optimal geometry of our proposed microneedle. Finally, Section VI concludes the paper.

II. SPECIFICATIONS OF PYRAMID-SHAPED MICRONEEDLE

Microneedles are typically designed with a variety of shapes which are imitations of natural needles. Female mosquito's fascicle is one example with long, slender, hollow tube. The mechanical strength of microneedles is one of main concerns. A microneedle should not be broken during the insertion process. The broken part may remain inside the human body, causing injury or abrasion.

Theoretical calculation and simulation have shown that our proposed microneedle has a high mechanical strength. Improved mechanical properties are obtained by using the following structural features: pyramid tip, square base, and asymmetrical position of microneedle hollow. Moreover, with a dual-diameter hollow, our proposed microneedle may improve collection ability due to an increasing shear rate in the body of the microneedle. Therefore, the possibility of blood coagulation can be minimized.

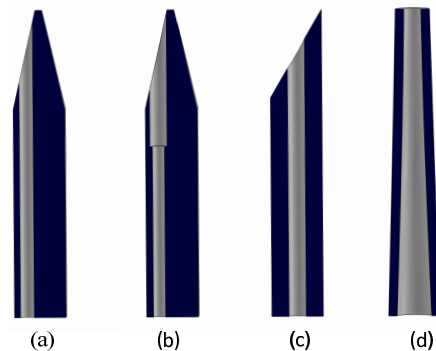


Figure 1. Horizontal cross sections of our proposed microneedles: (a) microneedle with uniform diameter hollow, (b) microneedle with dual-diameter hollow, in which the diameter of the tip is bigger than diameter of the body; compared with (c) traditional-shaped microneedle [1], (d) tapered hollow microneedle [2]. The brighter parts indicate the hollows of the microneedles

Hoa Le-Thanh is with Vestfold University College, Postboks 2243, N-3103 Tonsberg, Norway (Phone: +47 94246434, e-mail: Hoa.Le.Thanh@student.hive.no).

Nhut Tran-Minh is with Vestfold University College, Postboks 2243, N-3103 Tonsberg, Norway (e-mail: Nhut.Tran-minh@hive.no).

Hai Le The is with Vestfold University College, Postboks 2243, N-3103 Tonsberg, Norway (Tel.: ++47(0)41-18-68-21, Email: thehai_hcmu@yahoo.com).

Frank Karlsen is with Vestfold University College, Postboks 2243, N-3103 Tonsberg, Norway (e-mail: Frank.Karlsen@hive.no).

III. METHODS FOR PERFORMANCE EVALUATION

In this section, the theoretical solutions are presented. It begins by considering the applicability of Euler's theory, followed by the derivation of critical buckling load and maximum bending force. In addition, the insertion force is also studied with numerical simulation in COMSOL. Lastly, Casson's model is used to model blood flow.

A. Consideration of applicability of Euler's theory:

The strategy for evaluating mechanical strength of our proposed microneedle is to estimate failure forces by using Euler's elastic theory. As noticed before, in elastic buckling model, Euler's theory is only applicable for "long" column which has slenderness ratio (S) larger than critical slenderness ratio (S_{cr}). The formulas for S and S_{cr} are expressed as follows:

$$S = \frac{L_{eff}}{r_g} = \frac{2.1L}{\sqrt{I_{min}/A}}, \quad (1)$$

$$S_{cr} = \sqrt{\frac{2\pi^2 E}{\sigma_y}}, \quad (2)$$

where L_{eff} is the effective length for fixed-free column, r_g is radius of gyration, I_{min} is the minimum inertia moment, A is cross section area, E and σ_y are Young's modulus and yield strength of the material, respectively.

For short and intermediate regions (i.e. $S < S_{cr}$), there is no exact solution for calculating critical buckling load except approximate compensations. The most commonly used solutions are Johnson's linear (tough materials), parabolic formulas (brittle materials), and Secant's formula (eccentrically loaded). Previously, Zahn et al [3] also used Johnson's parabolic formula to estimate critical buckling load of his in-plane microneedles. The applicability of Euler's theory will be proven in Section IV.

B. Mechanical strength - Axial force

In this paper, the study of P_{cr} and F_b will be implemented with the performance comparison of the following microneedles: our proposed microneedle with uniform diameter hollow, our proposed microneedle with dual-diameter hollow, traditional-shaped microneedle proposed by Kou et al [1], and tapered microneedle proposed by Kim et al [2]. At failure point, axial component is called critical buckling load which can be calculated by using (3) derived in [2].

$$P_{cr} = \frac{E\pi^2}{2L^3} \int_0^L \sum_{i=0}^n I(z) \cdot \cos^2\left(\frac{\pi z}{2L}\right) dz \quad (3)$$

In (3), $I(z)$ is inertia moment. In our proposed microneedle, cross section of the microneedle is not constant but varies due to z-direction. There are five shapes of cross section which are shown in Fig. 2, thus the final value of P_{cr} consists of five integrals corresponding to five cross sections. For each region, the formula for $I(z)$ will be presented as follows:

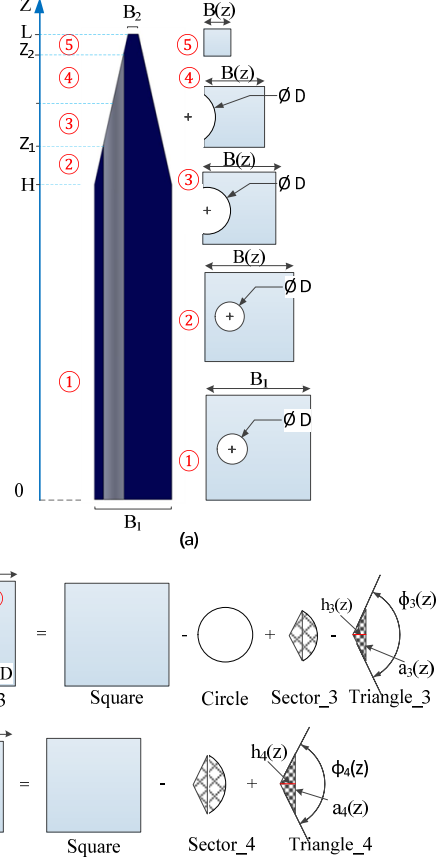


Figure 2. Cross sections of our proposed microneedle. (a) five cross sections correspond to five regions along z-direction; (b), (c) illustrations for calculation of inertia moment in Regions 3 and 4, respectively. They are the most difficult regions for calculating inertia moment due to the dependence on z of all geometrical variables.

- Region 1: z from 0 to H

$$I_1 = \frac{B_1^4}{12} - \frac{\pi D^4}{4 \cdot 2}. \quad (4)$$

- Region 2: z from H to Z_1 : $B(z) = B_1 - \frac{B_2 - B_1}{L} z$

$$I_2 = \frac{B(z)^4}{12} - \frac{\pi D^4}{4 \cdot 2}. \quad (5)$$

- Region 3: z from Z_1 to Z_2

$$I_3 = I_{square} - I_{circle} + I_{sector_3} - I_{triangle_3} \quad (6)$$

$$I_3 = \frac{B(z)^4}{12} - \frac{\pi D^4}{4 \cdot 2} + (\phi_3(z) - 2 \sin \phi_3(z)) \frac{D^4}{128} + \frac{(h_3(z)a_3(z))^3}{48} \quad (7)$$

- Region 4: z from Z_2 to Z_3

$$I_4 = I_{square} - I_{sector_4} + I_{triangle_4}, \quad (8)$$

$$I_4 = \frac{B(z)^4}{12} + (\phi_4(z) - 2 \sin \phi_4(z)) \frac{D^4}{128} + \frac{h_4(z)a_4(z)^3}{48}, \quad (9)$$

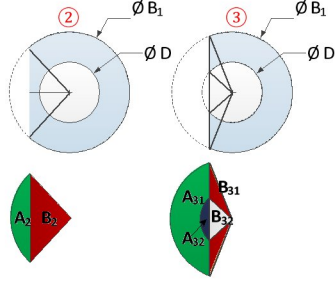


Figure 3. Examples for the cross section view at the tip of traditional-shaped microneedle. At the body, cross section is a hollow circle with outer and inner diameter is B_1 and D , respectively.

where $h_3(z)$, $a_3(z)$, $h_4(z)$, $a_4(z)$, $\phi_3(z)$, $\phi_4(z)$, $d_3(z)$ and $d_4(z)$ can be calculated based on basic geometry mathematic from Fig. 2(b) and Fig. 2(c).

- **Region 5: z from Z_3 to L**

$$I_5 = \frac{B(z)^4}{12} \quad (10)$$

With traditional-shaped microneedle as in Fig. 1(c), the calculations are more complicated than in our first proposed microneedle structure as in Fig. 1(a). On the other hand, cross section of tapered microneedle is simpler with the subtraction between inertia moment of circulars. Fig. 3 presents the illustrations of two most difficult sections at the tip of traditional-shaped microneedle structure followed by the corresponding formulas:

$$I_2 = I_{\text{circle}_{B1}} - I_{\text{circle}_{D}} + I_{\text{sector}_{A_2}} - I_{\Delta_{B_2}} \quad (11)$$

$$I_3 = I_{\text{circle}_{B1}} - I_{\text{circle}_{D}} - I_{\text{sector}_{A_{31}}} + I_{\text{sector}_{A_{32}}} - I_{\Delta_{B_{31}}} + I_{\Delta_{B_{32}}} \quad (12)$$

All computations are done by Maple 16 and the results will then be presented in Section IV.

C. Mechanical strength - Transverse force

In this part, criterion of maximum normal stress (σ_z) is applied to investigate failure due to transverse force. Brokenness is most likely to happen at the point of maximum stress, i.e. outermost edges at bottom of microneedle. And the formula for calculating maximum bending force (F_b) is as follow:

$$F_b = \frac{\sigma_y I}{cL} \quad (13)$$

This failure criterion is only applicable when neglecting the contributions of local stresses, i.e. concentrated stresses, which potentially cause cracks and propagation of cracks. This problem is especially critical for brittle materials such as cured SU-8. The detail calculations for F_b will be presented in Section IV.

D. Model of blood flow in microneedle

Microneedles are normally integrated as an array for high-volume collection of blood. In order to draw blood out, a certain value of negative pressure should be applied at the output of microneedle integration. In relation to collection



Figure 4. Design of dual-diameter microneedle hollow.

efficiency, clogging problem should be considered for continuous collection. Dealing with this problem, a dual-diameter hollow is proposed with diameter of tip (D_{tip}) is larger than diameter of body (D_{body}) as in Fig. 4. The idea is to create an increasing velocity from tip to body to increase shear rate. Optimal value of D_{tip} and D_{body} can be obtained from fluidic analysis.

The blood flow can be modeled by Casson's equation [4].

$$Q = -\frac{\pi D^4}{128\mu_c} \frac{\Delta P}{L} \left(1 - \frac{16}{7}\xi^{\frac{1}{2}} + \frac{4}{3}\xi - \frac{1}{21}\xi^4\right). \quad (14)$$

In (14), ΔP is pressure drop, Q is flow rate, D is hollow diameter, $\rho = 1060 \text{ kg/m}^3$ is blood density $\mu_c = \mu_p e^{2.19H_1}$ is the degree of Casson viscosity, $\mu_p = 0.00125 \text{ Ns/m}^2$ is the viscosity for a blood plasma, $\xi = \frac{4\tau_{yc} - L}{D \Delta P}$ is the stress ratios, and $\tau_{yc} = 0.004 \text{ N/m}^2$ is the Casson yield stress.

E. Simulation of skin penetration

For a fuller understanding of the mechanical picture when microneedle penetrates the skin, a numerical simulation is conducted. The required skin piercing pressure of 3.18MPa was indicated by Wilke et al in [6]. This value is used as a boundary condition for microneedle model in COMSOL 4.3. The answer for question of how much stress will be created with applied pressure of 3.18MPa will be given in the next section.

IV. RESULTS

A. Consideration of applicability of Euler's theory:

(Introduce briefly the general purposes of conducting six scenario)

In this paper, SU-8 2150 is used to fabricate our proposed microneedles with the mechanical properties of $E = 4.02 \text{ GPa}$ and $\sigma_y = 34 \text{ MPa}$. With $L = 1800 \mu\text{m}$, $S_{cr} = 48.3$ is obtained by using (1) and S can be calculated using (2). S is varied due to an increase in base width (B_1). This relationship is demonstrated in Table I and in Scenario 1.

• **Scenario 1:** The values of critical buckling load obtained from Euler and Johnson models are illustrated in Fig. 4. P_{cr} calculated with Johnson's formula critical buckling load of the proposed design is 3.4%, which is smaller than P_{cr} obtained from (3) when $B_1 = 300 \mu\text{m}$. Therefore, Euler's theory is still applicable for further calculations of critical buckling load with an error span of 3.4%.

TABLE I. SLENDERNESS RATIO AND ΔP_{cr} VERSUS BASE WIDTH

B_1 (μm)	280	285	290	295	300	305	310	315
S	49.7	48.9	48.1	47.3	46.6	45.9	45.2	44.5
ΔP_{cr} (%)	0	0	0.93	2.18	3.4	4.9	6.34	7.81

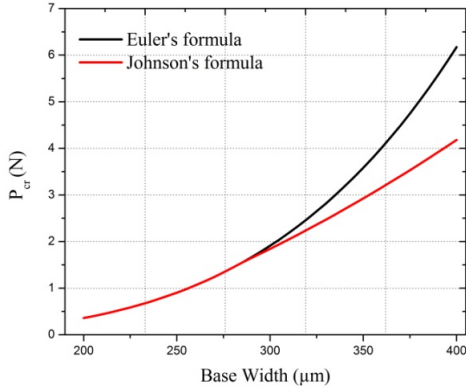


Figure 5. The comparison of P_{cr} between Euler and Johnson's models, applying for the proposed structure (without pyramid tip). P_{cr} from Johnson's formula is smaller than the value obtained from Euler's formula.

B. Mechanical strength

This section evaluates the mechanical performance of our proposed microneedle by comparing its P_{cr} and F_b with those of other proposed microneedles in Fig. 1. Testing procedure is established with four following scenarios.

Fig. 6 and Fig. 7 demonstrate the dependence of P_{cr} on microneedle length (L) and base width (B_1). Obviously, our proposed microneedle has higher P_{cr} compared to other design in the whole testing range of variables. In the interest range in length from $1500\mu\text{m}$ to $1800\mu\text{m}$, P_{cr} of dual-diameter hollow microneedle decreases from 2.84N to 2.27N . These values are approximately two times higher than those of other designs: 1.45N - 1.09N for traditional-shaped microneedle and 1.2N - 0.84N for tapered microneedle. Scenarios 3 and 4 also investigate the effect of dual-diameter hollow on P_{cr} . With $D_{tip}=100\mu\text{m}$, $D_{body}=80\mu\text{m}$, P_{cr} decreases slightly and the change in D_{body} does not degrade structural strength of our proposed microneedle. Additionally, mechanical strength becomes stronger when B_1 increases. The verification could be seen in Fig. 7 and Fig. 8.

• Scenario 2: P_{cr} and microneedle length

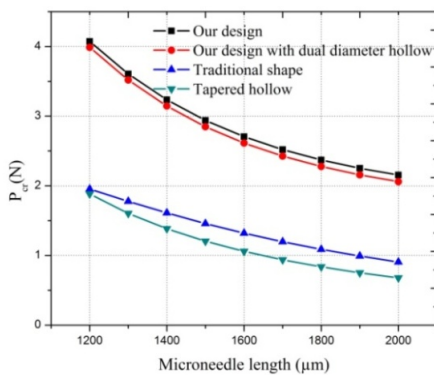


Figure 6. Critical buckling load (P_{cr}) versus microneedle length. P_{cr} tends to decrease when length increases. With a microneedle length in the range $1200\text{-}2000\mu\text{m}$, P_{cr} of our proposed microneedle is significantly higher than that of previously proposed microneedles.

• Scenario 3: P_{cr} and base width of microneedle

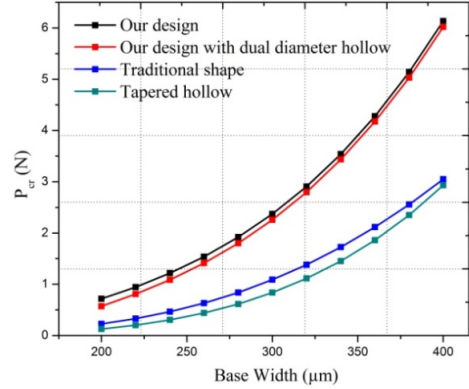


Figure 7. Critical buckling load (P_{cr}) versus base width. P_{cr} increases when the base width increases and P_{cr} of our proposed microneedle is approximately 2.3 time larger than that of traditional-shaped and tapered microneedles.

• Scenario 4: Maximum bending force

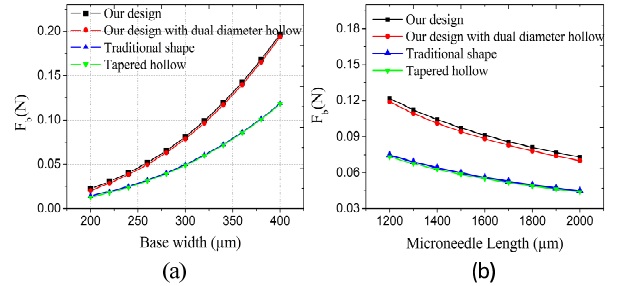


Figure 8. (a) Maximum bending force (F_b) versus base width, (b) Maximum bending force versus microneedle length. Our proposed microneedle has relatively higher F_b (approximately two times) compared to traditional shape microneedle and tapered microneedle.

• Scenario 5: Simulation of the insertion force

This scenario shows the ability of safe injection of our proposed microneedle. A pressure of 3.18MPa is applied uniformly over an area, called force-applying area (A). When microneedle penetrates deeply into skin, A also rises with the increasing penetration depth (D).

Fig. 9 presents insertion force and first principal stress (σ_p) corresponding to five different values of D . Second point of $D = 152\mu\text{m}$ (Z_2 in Fig. 2) illustrates the punctured position due to the deformation of skin before being penetrated. At this point, $\sigma_p = 7.05\text{MPa}$ which then rises to the maximum value of 12.3MPa at $D = 244\mu\text{m}$, i.e. point of $(Z_1+Z_2)/2$ in Fig. 2. Tress will be released when D reaches $580\mu\text{m}$ with $\sigma_p = 4.71\text{MPa}$.

Fig. 10 illustrates how force is applied and the resulting deformation of microneedle ($D = 580\mu\text{m}$, 1.22N). In Fig. 10(b), stress is distributed primarily at the top and bottom parts of microneedle. Therefore, crack and brokenness are most likely to happen at these regions. Moreover, the structure is slightly bent with maximum displacement of $6.23\mu\text{m}$.

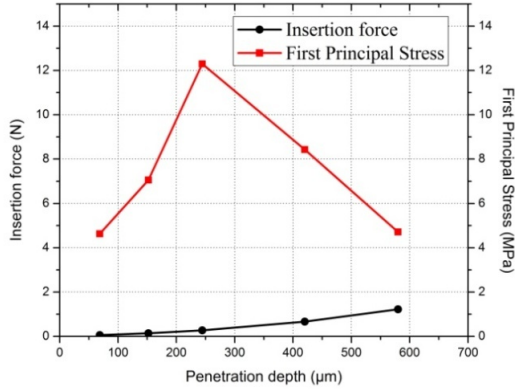


Figure 9. Insertion force and First Principal Stress caused by insertion pressure (3.18MPa) at different penetration depth.

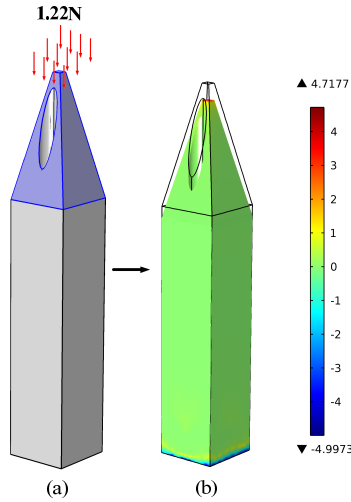


Figure 10. Microneedle under insertion force of 1.22N; (a) force-applying area; (b) deformation of microneedle

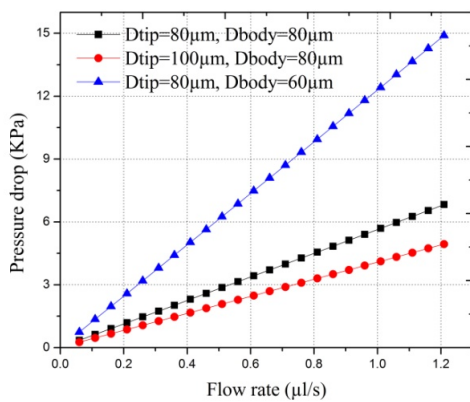


Figure 11. Flow rate versus pressure drop for three types of lumen. Pressure drop on the dual-diameter design with $D_{tip}=100\mu\text{m}$, $D_{body}=80\mu\text{m}$ (red line with circle marker) is relatively lower than two others. In other words, it provides higher volumetric rate at the same value of applied negative pressure.

B. Model of blood flow in microneedle

Scenario 6: Flow rate versus pressure drop

In this scenario, collection efficiency of two types of microneedle hollow (Fig. 1a,b) are analyzed and the results are shown in Fig. 11. The collection ability refers to drop pressure (ΔP) in a system, which is the necessary negative pressure that needs to be applied in order to achieve a certain flow rate (Q). Typically, ΔP is expected to be as small as possible for any fluidic device.

With $Q = 1\mu\text{l/s}$, a dual-diameter hollow ($D_{tip}=100\mu\text{m}$, $D_{body}=80\mu\text{m}$) has the lowest drop pressure of 4.1KPa compared to 5.6KPa for single diameter hollow and 12.4KPa for dual-diameter hollow ($D_{tip}=80\mu\text{m}$, $D_{body}=60\mu\text{m}$).

V. DISCUSSIONS

A. Mechanical strength

Theoretical calculation and simulation show that our proposed microneedles have improved mechanical properties. Specifically, the proposed microneedle can tolerate higher critical buckling load and higher bending force as shown in Fig. 6 - Fig. 8. These improvements could come from the optimal geometry of our microneedles. In fact, inertia moment of square is higher than circle with the same area. The structure with a square cross-section is thus stiffer and possibly can bear higher axial and transverse forces.

In simulation of insertion force as show in Fig. 9, as long as σ_p is kept smaller than the yield strength of material, i.e. $\sigma_y = 34\text{MPa}$, failure will not happen. However, failure may happen at point of $(Z_1+Z_2)/2$ where σ_p reaches its maximum. This issue will become more critical when insertion force increases.

In this paper, we examine the failure due to normal stress generated by bending force. However, bending force may also induce shear stress acting along y,z-axis. As be noticed, failure due to shear stress is one of the critical failure mechanisms that should not be neglected. Moreover, the calculations in this paper are conducted for concentrated force. However, resistance forces are practically distributed in a specific force-applying area. Thus maximum bending force particularly should be treated as a uniformly distributed force. These two aspects should be taken into account in failure analysis.

B. Model of blood flow in microneedle

One advantage of dual-diameter hollow is low pressure drop. Low drop pressure will benefit the system in terms of stability and working efficiency.

Moreover, in UV lithography, transmission of lights becomes difficult with a millimeter-range layer of SU-8 due to light scattering phenomenon. With small hollow diameter (for example $60\mu\text{m}$), high aspect ratio structure may not be easy to obtain. Therefore, with the chosen of diameters ($D_{tip}=100\mu\text{m}$, $D_{body}=80\mu\text{m}$), fabrication of ultra-high microneedles can be easier with relative large dimension of printed features on mask.

C. Design criteria for our proposed microneedle

According to the results shown previously in section VI, an optimized geometrical specifications for microneedle is chosen based on the following criteria:

- *Base width:* Base width of microneedle can be designed in the range from 275 μm to 325 μm , which provides $P_{cr} > 1.83\text{N}$ and $F_b > 0.054\text{N}$. In this range, microneedle can be treated as long column and be able to use Euler's theory. In this paper, it was chosen for another reason, i.e. due to the ability of unmolding SU-8 microneedle from PDMS mould.
- *Microneedle length:* 1500 μm -1800 μm . However, it cannot be fabricated with $L > 1800\mu\text{m}$ due to the limitation of SU-8 coating - reflowing of SU-8 as developed by Lin et al. in [7].
- *Tip angle:* 30°. There is a trade-off between insertion force and mechanical strength. Moreover, an inclined angle is limited up to 40° due to small distance between base and UV light source in Mask Aligner Karl Suss, MA 150 CC.
- *Cylindrical hollow:* dual-diameter hollow with $D_{tip}=100\mu\text{m}$, $D_{body}=80\mu\text{m}$ introduces an increase in shear rate in the body part of microneedle. The value of 80 μm is chosen because diameter hollow for blood extraction must be bigger than 50 μm [8].

VI. CONCLUSION

This paper proposes a design of pyramid-shaped microneedle for continuous blood collection that requires strong microneedle. Our results from mathematical frameworks confirm that our proposed microneedle can tolerate higher applied forces compared to other previous designs. In addition, the new design of dual-diameter hollow shows the ability to reduce blood clogging, thus improving collection efficiency.

Further studies are to fabricate and to test our proposed microneedles. The following fabrication techniques can be used: lithography with ultra-thick SU-8 2150, and PDMS replica molding. The pyramid tip can be constructed by multiple exposures with a certain angle, i.e. tip angle. In addition, failure mechanism due to shear stress will also be investigated in our next work.

REFERENCES

- [1] S.C Kuo and Y. Chou, "A Novel Polymer Microneedle Arrays and PDMS Micromolding," *Tamkang Journal of Science and Engineering*, vol. 7, pp. 95-98, 2004.
- [2] K. Kim, D. S. Park, H. M. Lu, W. Che, K. Kim, J.B. Lee, and C.H. Ahn, "A tapered hollow metallic microneedle array using backside exposure of SU-8," *Journal of Micromechanics and Microengineering*, vol. 14, no. 4, pp. 597-603, Apr. 2004.
- [3] J. Zahn, N. Talbot, D. Liepmann, and A. Pisano, "Microfabricated Polysilicon Microneedles for Minimally Invasive Biomedical Devices," *Biomedical Microdevices*, vol. 2, pp. 295-303, 2000.
- [4] K. Tsuchiya, N. Nakanishi, and E. Nakamachi, "Development of blood extraction system designed by female mosquito's blood sampling mechanism for bio-MEMS," *Biomedical Applications of Micro- and Nanoengineering*, vol. 5651, pp. 379-388, 2005.
- [5] F. Amin and S. Ahmed, "Design, modeling and simulation of MEMS-based silicon Microneedles," *Journal of Physics: Conference Series*, vol. 439, no. 012049, pp. 1-13, 2013.
- [6] N. Wilke, C. Hibert, J. O'Brien, and A. Morrissey, "Silicon microneedle electrode array with temperature monitoring for electroporation," *Sensors and Actuators A: Physical*, vol. 123-124, pp. 319-325, 2005.
- [7] G.-B. L. Che-Hsin Lin, Bao-Wen Chang, and A. G.-L. Chang, "A new fabrication process for ultra-thick microfluidic microstructures utilizing SU-8 photoresist," *Journal of Micromechanics and Microengineering*, vol. 12, pp. 590-597, 2002.
- [8] C. G. Li, C. Y. Lee, K. Lee, and H. Jung, "An optimized hollow microneedle for minimally invasive blood extraction," *Biomed Microdevices*, vol. 15, pp. 17-25, Feb. 2013.

Publication P3:

P3: **Hoa Le-Thanh**, Nhut Tran-Minh, Hai Le The, Frank Karlsen, "A Study on Mechanical Strength of Pyramid-Shaped Microneedle", in Proc. of IEEE-Middle East Conference on Biomedical Engineering, pp. 29-32, February 2014.

A Study on Mechanical Strength of Pyramid-Shaped Microneedle

Hoa Le-Thanh*, Nhut Tran-Minh, Hai Le The, Frank Karlsen

Abstract— This paper introduces a novel design of hollow microneedle for efficient blood extraction. With special features such as square base and pyramid tip, our proposed microneedle may have better mechanical strength compared with that of previously proposed microneedles. We also provide mathematical frameworks for analyzing both mechanical strength and fluidic transport efficiency of microneedles. To evaluate the performance of our microneedle compared with that of previously proposed microneedles we conduct intensive calculations with various parameter settings. According to calculation results, our proposed microneedle may be optimal for blood collection. Moreover, our proposed microneedle provides continuous blood collection with higher volumes because of its optimal hollow width with recommended applied pressure.

Keywords—microneedle; blood extraction; mechanical failure analysis; fluid mechanics

I. INTRODUCTION

Disease diagnostics are mostly analyzed from fluids in which blood is one of priceless sources, containing much information about health status of the object. Blood is a problematic complex fluid due to the none-Newtonian behaviors, the very large number of cells and polymers and the coagulation force. Blood is traditionally collected by hypodermic needle which normally causes pain and requires medical implementation. Therefore, a painless alternative such as, a micro-scale needle, that is able to handle whole blood was introduced.

In [1], the authors introduce numerical simulation for traditional shaped microneedle. They study blood filling process with surface tensions acting as driving force instead of investigation fluidic behaviors. In contrast, the authors in [2] only focus on analytical solution for critical buckling load of tapered hollow microneedle which is weaker with significant increase in microneedle length (longer than 1500 μm), introduces possibility of failure. As study in [3], a microneedle for blood extraction is designed only based on simulations of bending force and fluid flow without producing mathematical models. Moreover, only one test with specific dimension of the microneedle is carried out. Therefore, it does not provide good guidelines for designers. Motivated by the above issues, in this paper we propose a new design of microneedle that

may be stronger and more efficient for blood extraction and initial treatment.

The rest of this paper is organized as follows. In Section 2, we describe the novel design of our proposed microneedle and its advantages. In Section 3, we provide mathematical models to analyze the structural strength for all and blood flowing inside microneedles. In Section 4, calculation results are presented and discussed. Optimal design is then selected based on the analysis results of mechanical strength and fluid flow. Finally, Section 5 concludes the paper.

II. THE NOVEL DESIGN OF OUR PROPOSED MICRONEEDLE

In the practical use of microneedle, one of the most critical problems is the brokenness of microneedle tip. Therefore, designing a microneedle with strong structure is extremely important. In this paper, we propose a stronger and more efficient microneedle. Fig. 1 shows four different microneedles and the corresponding cross-sections of all microneedles i.e. our proposed microneedle, traditional shaped microneedle [1], double lumen microneedle [3] and tapered hollow microneedle [2].

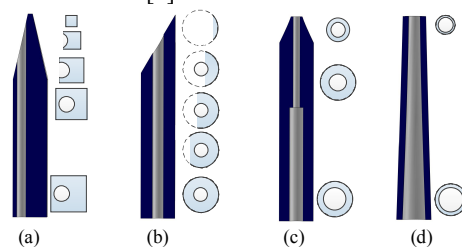


Figure 1. Different microneedles and their cross sectional areas. (a) our proposed microneedle, (b) traditional shaped microneedle [1], (c) double lumen microneedle [3], (d) tapered hollow microneedle [2]

The geometrical structure of our proposed microneedle has the following special features. Firstly, with square base, our proposed microneedle can tolerate higher axial and transverse forces because the inertia moment of square is approximately 1.69 times bigger than that of circle with the same dimension. Second, with pyramid tip, our proposed microneedle reduces the insertion force because of smaller contact area compared to the tip of double lumen microneedle [3] and tapered hollow microneedle [2]. Third, the cylindrical lumen our proposed microneedle is not placed exactly in the middle of the microneedle but in the side face of pyramid tip, making the tip stronger. If the center of hollow is at middle of structure, the contact area will be much smaller, inducing higher possibility of failure. All above advantages of our microneedle will be proved mathematically in Section 3 and Section 4 with various input parameters.

Hoa Le-Thanh is with Vestfold University College, Postboks 2243, N-3103 Tonsberg, Norway (Phone: +47 94-24-64-34, e-mail: Hoa.Le.Thanh@student.hive.no).

Nhut Tran-Minh is with Vestfold University College, Postboks 2243, N-3103 Tonsberg, Norway (e-mail: Nhut.Tran-minh@hive.no).

Hai Le The is with Vestfold University College, Postboks 2243, N-3103 Tonsberg, Norway (Tel.: ++47(0)41-18-68-21, Email: the-hai_hcmut@yahoo.com).

Frank Karlsen is with Vestfold University College, Postboks 2243, N-3103 Tonsberg, Norway (e-mail: Frank.Karlsen@hive.no).

III. MATHEMATICAL FRAMEWORKS FOR EVALUATING THE PERFORMANCE OF MICRONEEDLES

In this section, we present step-by-step the mathematical frameworks for evaluating two important characteristics of microneedles: the mechanical strength of and fluid transport efficiency.

A. Analytical model of mechanical strength

Microneedle is designed to pierce deeply into the dermis layer in order to effectively extract blood. However, during penetration process, the skin acts as a mechanical barrier, resisting the insertion of microneedle. Skin resistance is modeled as axial and horizontal forces which may make microneedle bend or break. At failure point, these forces are called critical buckling load (P_{cr}) and maximum bending force (F_b). In this section, we derived mathematical expressions to calculate P_{cr} and F_b for four different shapes of microneedles in Fig. 1.

The compressive load (U_c) and strain bending energy (U_s) can be expressed as

$$U_c = P\lambda = \frac{P}{2} \int_0^L \left(\frac{dY(z)}{dz} \right)^2 dz, \quad (1)$$

$$U_s = \int_0^L \frac{M(z)^2}{2EI(z)} dz. \quad (2)$$

According to Euler's beam theory, the critical buckling load (P_{cr}) of P is obtained by giving (1) equals to (2). This is called the energy method. Thus, the final formula for P_{cr} is

$$P_{cr} = \frac{E\pi^2}{2L^3} \int_0^L I(z) \cos^2 \left(\frac{\pi z}{2L} \right) dz, \quad (3)$$

where λ is the displacement, E is Young's modulus, L is the total length of column, $Y(z)$ is the deflected shape, $M(z)$ is the bending moment and $I(z)$ is the inertia moment.

The general formula of inertia moment used in (3) can be presented as

$$I(z) = \sum_{i=1}^5 I_i(z), \quad (4)$$

where $I_i(z)$ is the function of inertia moment for each cross-section when z increases from 0 to microneedle length.

We will derive formulas of inertia moments for all microneedles in the following parts by adding or subtracting the inertia moments of basic shapes such as square, circle,

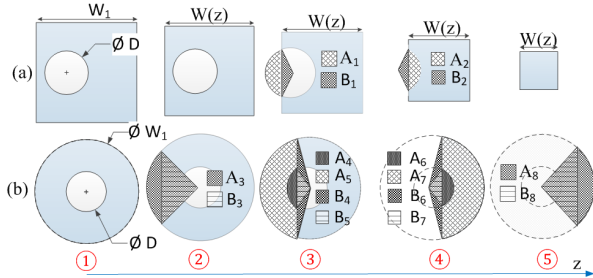


Figure 2. Cross-sections of different microneedles. (a) our proposed microneedle, (b) traditional shaped microneedle [1]

circular sector and triangle. Fig. 2 shows in detail the cross sections of our proposed microneedle and the microneedle designed by Kuo et al. In Fig. 2, A_i and B_i refer to corresponding circular sector and triangle at each cross sectional area.

Firstly, we derive the expression for $I_i(z)$ of our proposed microneedle which is composed of five cross sectional areas as in Fig. 2a

$$I_1 = I_{\text{square}_W1} - I_{\text{circle}_D}, \quad (5)$$

$$I_2 = I_{\text{square}_W(z)} - I_{\text{circle}_D}, \quad (6)$$

$$I_3 = I_{\text{square}_W(z)} - I_{\text{circle}_D} + I_{A_1} - I_{B_1}, \quad (7)$$

$$I_4 = I_{\text{square}_W(z)} + I_{A_2} - I_{B_2}, \quad (8)$$

$$I_5 = I_{\text{square}_W(z)}. \quad (9)$$

In the above equations, I_1 and I_2 are simply obtained by subtracting the inertia moment of circle with diameter D from the inertia moment of square with dimension $W(z)$. $W(z)$ is a z -dependent function which can be calculated as

$$W(z) = W_1 - \frac{W_2 - W_1}{L_{\text{tip}}} z, \quad (10)$$

where W_1 is the width of base, W_2 is the width of microneedle tip and L_{tip} is the length of pyramid tip.

Second, the inertia moments of traditional shaped microneedle can be calculated with same method that applied for our proposed microneedle above.

$$I_1 = I_{\text{circle}_W1} - I_{\text{circle}_D} \quad (11)$$

$$I_2 = I_{\text{circle}_W1} - I_{\text{circle}_D} + I_{A_3} - I_{B_3} \quad (12)$$

$$I_3 = I_{\text{circle}_B1} - I_{\text{circle}_D} - I_{A_5} + I_{B_5} + I_{A_4} - I_{B_4} \quad (13)$$

$$I_4 = I_{A_7} - I_{B_7} + I_{B_6} - I_{A_6} \quad (14)$$

$$I_5 = I_{A_8} - I_{B_8} \quad (15)$$

Third, the inertia moments of double lumen microneedle as illustrated in Fig. 3a are calculated as follows

$$I_1 = I_{\text{circle}_W1} - I_{\text{circle}_D1}, \quad (16)$$

$$I_2 = I_{\text{circle}_W1} - I_{\text{circle}_D2}, \quad (17)$$

$$I_3 = I_{\text{circle}_W(z)} - I_{\text{circle}_D2}. \quad (18)$$

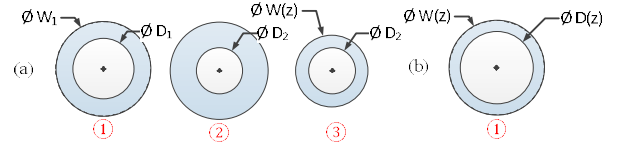


Figure 3. Cross-sections of different microneedles. (a) double lumen microneedle [3], (b) tapered hollow microneedle [2]

Lastly, for the tapered hollow microneedle there is only one formula for inertia moment as

$$I_1 = I_{\text{circle_W}(z)} - I_{\text{circle_D}(z)}. \quad (19)$$

The effect of maximum bending force is also investigated. According to Euler's beam theory, the formula for maximum bending force (F_b) is derived as

$$F_b = \frac{\sigma_y I}{cL}, \quad (20)$$

where σ_y : the yield strength, I is the inertia moment, c is the distance from the neutral axis (z axis in this case) to the outermost edge of the microneedle, L is the length of the microneedle. All of the computations are done by Maple 16 and the results are presented in Section 4.

B. Analytical model of blood transport efficiency

In microneedle design, the diameter of hollow is significantly important to blood transport efficiency. We investigate blood flow in the hollow of microneedle by using three models. The first model of blood flow rate is developed by Oka in [5] as

$$Q = -\frac{\pi R^4 \Delta P}{8\eta L} \left(1 - \frac{16}{7} \xi^2 + \frac{4}{3} \xi - \frac{1}{21} \xi^4\right), \quad (21)$$

where Q is the flow rate, R is inner radius, η is the Casson's coefficient of viscosity, ξ is the shear stress which is presented in (22).

$$\xi = \frac{4\tau_{yc}}{D} \left(\frac{-\Delta P}{L}\right)^{-1} \quad (22)$$

Two other models are the models that we derive from the modified Bernoulli's equation [6] as follows

$$\Delta P = \frac{128\mu QL}{\pi D^4} + \rho \sum K \frac{8Q^2}{\pi^2 D^4} - \rho g(Z_1 - Z_2), \quad (23)$$

where μ is the kinematic viscosity of blood, ΔP is pressure drop, Q is flow rate, D is diameter, ρ is blood density, and K is inertial minor loss.

Equation (23) is a quadratic function of Q . By solving (23) we obtain the second model of blood flow rate in case of without gravity effect as

$$Q = \frac{32\eta L \pi + \sqrt{1024\eta^2 L^2 \pi^2 + 2\rho \Delta P \pi^2 D^4 \sum K + 2\rho^2 g^2 \pi^2 D^4 (Z_1 - Z_2)}}{4\rho \sum K} \quad (24)$$

The third model of blood flow rate in case of with gravity effect is then derived from (24) as

$$Q = \frac{32\eta L \pi + \sqrt{1024\eta^2 L^2 \pi^2 + 2\rho \Delta P g \pi^2 D^4 \sum K + 2\rho^2 g^2 \pi^2 D^4 (Z_1 - Z_2)}}{4\rho \sum K} \quad (25)$$

IV. PERFORMANCE EVALUATION AND DISCUSSIONS

In this section, we evaluate the structural strength of our proposed microneedle compared with that of previous microneedle by changing several design parameters such as length, base size, and hollow diameter. We also show how

well blood flows in our microneedle with different pressure drop and hollow diameter.

Table I presents the parameter settings of three scenarios for evaluating the strength of our proposed microneedle. Firstly, critical buckling load (P_{cr}) is examined in scenario 1 and 2 by changing microneedle length (L_1) and hollow diameter (D). Secondly, maximum bending force (F_b) is studied in scenario 3, by changing microneedle width (W_1).

Fig. 4 and Fig. 5 show that the structural strength of our proposed microneedle is significantly higher than that of the other microneedles in all settings of microneedle length and hollow diameter. Specifically, in Fig. 4 when $L=1800\mu\text{m}$, the critical buckling load of our design is 2.371N which is approximately two times bigger than 1.09N, 1.19N, and 0.837N of traditional shaped microneedle, tapered hollow microneedle, and double lumen microneedle, respectively. Fig. 4 also illustrates that the cylindrical hollow should be placed on the side face of the pyramid tip for stronger structure. In Fig. 5, when changing microneedle hollow diameter our proposed microneedle also has better strength under axial force. However, the change in D does not induce much difference in critical buckling force. Therefore, the design of hollow must be based on a criterion of fluidic analysis, which will be presented in the next subsection.

TABLE I. TEST PROCEDURE FOR CRITICAL BUCKLING LOAD AND BENDING FORCE

	Scenario	Variable	Range (μm)	Values (μm)
P_{cr}	1 - Fig. 4	L	1200 - 2000	$W_1=300$ $D=80$
	2 - Fig. 5	D	50 - 120	$L=1800$ $W_1=300$
F_b	3 - Fig. 6	W_1	200 - 400	$L=1800$ $D=80$

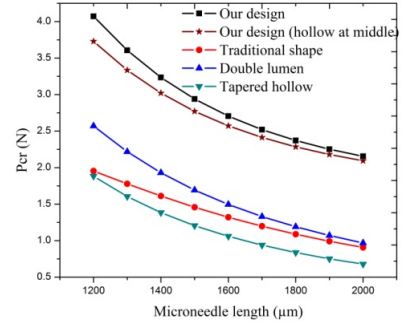


Figure 4. Critical buckling loads with change of microneedle length

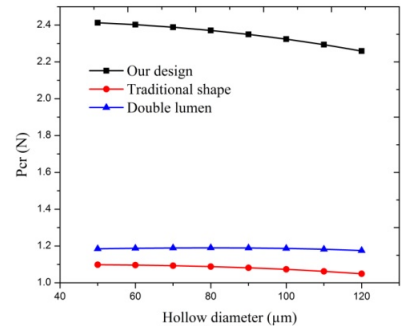


Figure 5. Critical buckling loads with change of hollow diameter

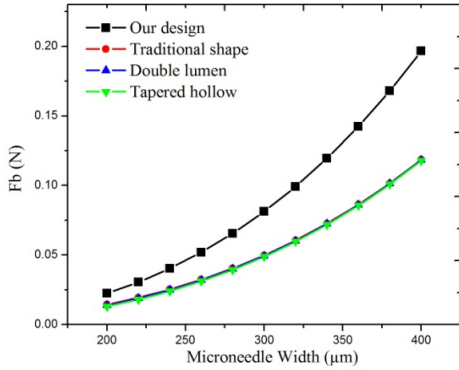


Figure 6. Maximum bending force with change of microneedle width

Fig. 6 shows the impact of square base on bending force with different hollow diameter. As we can see in Fig. 6, with square cross section our proposed microneedle has $F_b=0.081\text{N}$, which is 1.65 times stronger than $F_b=0.049\text{N}$ of the rest three microneedles with circular cross-sections.

Additionally, the value of critical buckling load 2.371N for one single microneedle, the total critical force for a 3×3 microneedle array is 21.34N . In related to skin resistance, the necessary pressure for piercing human skin is 3.18MPa , then the required penetration force for a microneedle array is approximately 2.43N . Therefore, our proposed microneedle may not only successfully penetrate human skin but may also can resist a large value of external forces which will be presented in future research.

Next, we examine the characteristics of blood flowing in our microneedle. Constants in (14-19) are chosen as follows: $\mu=0.0035\text{Ns/m}^2$, $\rho=1060\text{kg/m}^3$, the minor losses at the inlet and outlet are $K_1=0.5$ and $K_2=1$, $\eta=0.003\text{Ns/m}^2$, $\tau_{ve}=0.004\text{N/m}^2$ and $\mu_p=0.00125\text{Ns/m}^2$. We create two scenarios as below:

- **Scenario 1:** We increase the applied pressure drop from 1KPa to 30KPa with a $80\mu\text{m}$ -diameter single lumen. The obtained flow rates are shown in Fig. 7.
- **Scenario 2:** We change the diameter of single lumen from $50\mu\text{m}$ to $120\mu\text{m}$ with two values of pressure drop, i.e. 7KPa and 11KPa . The obtained flow rates are shown in Fig. 8.

According to Fig. 7a and Fig. 8a, there are two models that suitable to model blood flow in microneedle hollow, i.e. the model developed in [5] and the model we derived from Bernoulli's formula without gravity effect.

From Fig. 7b and Fig. 8b we can see that small testing range of flow rate provides guidelines for designing microneedle hollow. Specifically, hollow diameter can be selected based on the expected values of flow rate and extracted volume. In addition, according to the results in Fig. 7b when flow rate is $1\mu\text{l/s}$ the corresponding pressure drop of single lumen is approximately 5.58KPa . It means that pressure drop in microneedle hollow, which is also called as extraction ability as in [4], is the required negative pressure that need to be generated by actuator or pump.

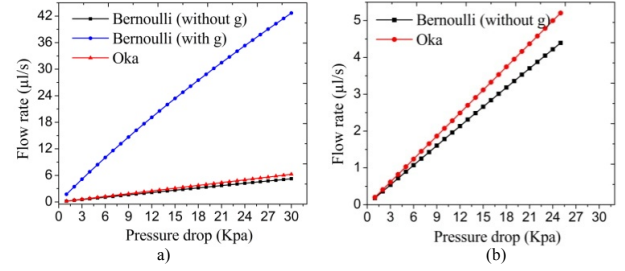


Figure 7. The relationship between flow rate and pressure drop. (a) big range of flow rate, (b) small range of flow rate

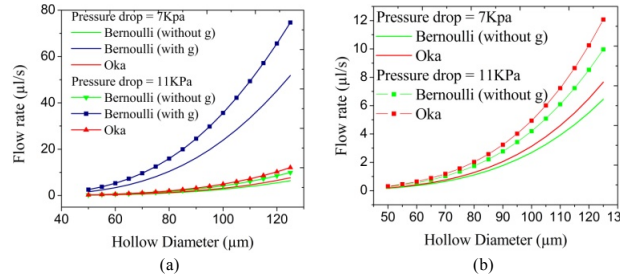


Figure 8. The relationship between flow rate and hollow diameter. (a) big range of flow rate, (b) small range of flow rate

V. CONCLUSION

In this paper, we propose a novel hollow microneedle which may have better mechanical properties, higher strength against skin resistance and external forces. The calculation results confirm that our proposed microneedle can bear higher critical buckling load and maximum bending force compared to previously proposed microneedles such as traditional shaped microneedle, double lumen micro needle, and tapered hollow microneedle. Moreover, with an analysis of blood flow and optimal values of diameter of hollow and fluidic parameters the ability to demonstrate continuous blood extraction without coagulation is at hand. Our proposed microneedle can be fabricated by using lithography with ultra-thick SU-8 2150, inclined exposure, and PDMS molding. Numerical simulations, fabrication, verification and validation will be presented in our next work.

REFERENCES

- [1] S.C Kuo and Y. Chou, "A Novel Polymer Microneedle Arrays and PDMS Micromolding," *Tamkang Journal of Science and Engineering*, vol. 7, pp. 95-98, 2004.
- [2] K. Kim, D. S. Park, H. M. Lu, W. Che, K. Kim, J.B. Lee, and C.H. Ahn, "A tapered hollow metallic microneedle array using backside exposure of SU-8," *Journal of Micromechanics and Microengineering*, vol. 14, no. 4, pp. 597-603, April 2004.
- [3] S. Tayyaba, M. W. Ashraf, and N. Afzulpurkar, "Design and simulation of double lumen polymeric microneedles for blood transport," in *Proc. of 2nd International Conference on Mechanical and Electrical Technology (ICMET)*, pp. 615-618, September 2010.
- [4] D. V. Nicolau, K. Tsuchiya, N. Nakanishi, and E. Nakamachi, "Development of blood extraction system designed by female mosquito's blood sampling mechanism for bio-MEMS," *SPIE Proceedings*, vol. 5651, pp. 379-388, March 2005.
- [5] Oka, S., "Rheology-Biorheology. Kyokabo", Tokyo, 1974
- [6] W. S. Janna, *Design of Fluid Thermal Systems*, CL Engineering Publisher, 3rd ed., May 2009.